2018

Kinetic, Metabolic and Macromolecular Response of Bacteria to Antimicrobial Agents

Fatemeh Faghihzadeh
University of Rhode Island, f.faghihzadeh@gmail.com

KINETIC, METABOLIC AND MACROMOLECULAR RESPONSE OF BACTERIA TO ANTIMICROBIAL AGENTS

BY

FATEMEH FAGHIHZADEH

A DISSERTATION SUBMITTED IN PARTIAL FULFILLMENT OF THE

REQUIREMENTS FOR THE DEGREE OF

DOCTOR OF PHILOSOPHY

IN

CIVIL AND ENVRIONMENTAL ENGINEERING

UNIVERSITY OF RHODE ISLAND

2018

DOCTOR OF PHILOSOPHY DISSERTATION

OF

FATEMEH FAGHIHZADEH

APPROVED:

Dissertation Committee:

Major Professor Vinka Oyanedel Craver

Ali Shafaqat Akanda

David C. Smith

Nasser H. Zawia
DEAN OF THE GRADUATE SCHOOL

UNIVERSITY OF RHODE ISLAND
2018

ABSTRACT

Bacteria have the extraordinary capability to modify their phenotype in response to stress agents. Response mechanisms to stressor (such as nanoparticles or light treatments) are the result of an evolutionary process in which bacteria can become resistant, or adapt to the stressor. Therefore, it is essential to elucidate the bacterial adaptation mechanisms to metal nanoparticles or pulse ultraviolet light since these processes not only can compromise the efficacy of these treatment methods but also has implications to public health issues.

Silver nanoparticles (AgNPs) are one of the most commonly used nanomaterials in consumer products and medical applications due to their antimicrobial properties. Also, pulsed lights (PL) applications for water treatment purposes are gaining increasing attention. PL has showed higher inactivation of microorganisms and degradation of PAHs, because of its rich and broad-spectrum UV content, high energy peaks and predictable treatment outcomes. However, the fate of microorganisms after exposure to AgNPs and pulsed lights as well as their negative impacts possible on the environment and public health are growing concerns.

There are knowledge gaps related to: the studying molecular level change of microorganism after exposure to AgNPs by Fourier-transform infrared spectroscopy (FTIR); Bacterial adaptation to chronic exposure to nanoparticles in continuous culture: kinetic and macromolecular response; and the effect of pulsed ultraviolet light system for removal of polycyclic aromatic hydrocarbon and disinfection of pathogens in drinking water.

In this study, *Escherichia coli* K-12 MG1655 (*E. coli*) responses to AgNPs was assessed under batch and continuous conditions. Further, we investigated the response of the same bacteria to PL. In detail, we evaluated antimicrobial agent's impacts on metabolic functions and cell structure such as, colony formation units, membrane permeation, respiration, growth, gene regulation and changes in cellular composition.

The results of batch culture for AgNPs toxicity test showed that bacteria developed resistance toward AgNPs and resulted in changes in the genotype and expression in the phenotype. Moreover, in continuous culture, results showed that culture growth conditions significantly affect bacterial response to nanoparticle exposure. Finally, from PL exposure to bacteria we obtained that the antimicrobial efficiency of PL depends on the PL lamp cut-off.

This study provides data that have a predominant role to determine the performance of toxicological tests. Hence, the knowledge of nanoparticles fate in different growth condition minimizes the upcoming environmental and public health issues due to releasing nanoparticles release on the ecosystems. Also, understanding the bacterial responses to antimicrobial agents help us to select the more sensible agents for antimicrobial purposes.

ACKNOWLEDGMENTS

I would like to thank my advisor, Dr. Vinka Oyanedel Craver for her guidance, patience and unwavering support through this project. I would also like to thank the example, motivation, inspiration and support I received from Dr. David Smith. I owe a special thanks to Dr. Thomas Boving, for his support, guidance, and transmitted knowledge for the completion of my work and studies as well as Dr. Ali Shafaqat Akanda for his assistance and encouragement. A big thanks to Dr. Nelson M. Anaya and Hichem Hadjeres for being an excellent research partner and providing huge support for this project. I warmly thank all of my undergraduate assistant, without whom this project would not have been possible: Magda, Kyle, Katrina. I am grateful for my excellent lab mates, Varun, Laura, Ivan, Ryan, Dounia, Hannes for making our workspace an enjoyable environment.

Special thanks go to Civil and Environmental Engineering family specially Kelly, Alfi, Supria and Pouria, as well as my friends at Chemical Engineering Department, especially Nasim, Joseph and Akram for their help, sharing, and advice during one of the most important period of my professional career. Also, I want to express gratitude to the Graduate School of Oceanography specially Ewelina and Amanda.

I want to thank my husband Arash Bigdeli, my mother Marzieh Moslemi and my sister Shabnam Faghihzadeh for their belief in me during the last years, as well as express my gratitude towards Iranian community in Rhode Island for their endless support specially Mohammad Reza Abtahi, Elmira S. Namin, Anita E. Tolouei,

Fatemeh Nemati, Soroush Kouhi, Arash N. Shirazi, Armin Sadighi, Shaghayegh Rezazadeh, and Amir N. Shirazi. And I am very appreciative of my entire Rhode Island community inside and outside of academia who have made my time in the ocean state such a pleasure

PREFACE

This dissertation is presented in manuscript format in accordance with University of Rhode Island Graduate School Guidelines. There are three sections contained within this dissertation. The first chapter is entitled “FOURIER TRANSFORM INFRARED SPETROSCOPY TO ASSESS MOLECULAR LEVEL CHANGES OF MICROORGANISMS EXPOSED TO NANOPARTICLES” and authored by Fatemeh Faghihzadeh, Nelson M. Anaya, Laura A. Schifman and Vinka Oyanedel-Craver and has been published at the Journal of Nanotechnology for Environmental Engineering. The second chapter is entitled “KINETIC, METABOLIC AND MACROMOLECULAR RESPONSE OF BACTERIA TO CHRONIC NANOPARTICLE EXPOSUR INONTINUOUS CULTURE” and authored by F. Faghihzadeh, N. M. Anaya, C. Astudillo-Castro, and V. Oyanedel-Craver and is in review at the Environmental Science-Nano Journal. The third chapter is entitled “COMPARISON OF TWO PULSED LIGHT LAMPS FOR DISINFECTION AND DEGRADATION ORGANIIC COMPOUNDS IN AQUEOUS SOLUTIONS” and authored by Faghihzadeh, F., Anaya, N.M., Hadjeres, H., Boving, T.B., Oyanedel-Craver and in preparation for submission to Water research Journal.

TABLE OF CONTENTS

LIST OF TABLES

LIST OF FIGURES

MANUSCRIPT – I: FOURIER TRANSFORM INFRARED SPETROSCOPY TO ASSESS MOLECULAR LEVEL CHANGES OF MICROORGANISMS EXPOSED TO NANOPARTICLES

Published in the Nanotechnology for Environmental Engineering Journal, April 2016

Fatemeh Faghihzadeh[a], Nelson M. Anaya[a], Laura A. Schifman[a] and Vinka Oyanedel-Craver[a*]

[a] Department of Civil and Environmental Engineering. University of Rhode Island, 1 Lippitt Rd., Bliss Hall 203 Kingston, Rhode Island 02881, United States

* Corresponding author: Vinka Oyanedel Craver

Email: craver@uri.edu,

Phone: (401) 874 2784,

Fax: (401) 874 2786

Abstract

Fourier transform infrared (FTIR) is a spectroscopy method that can identify variations in the total composition of microorganisms through the determination of changes of functional groups in biomolecules. FTIR measures the vibration and rotation of molecules influenced by infrared radiation at a specific wavelength. This technique allows the identification of structural changes of the molecular binding between microorganisms and metal atoms, which can provide information about the nature of their interactions. In this review article, we will describe the state of the art in current uses of FTIR for the elucidation of bacteria–nanoparticle interactions. We will describe advantages for the application of FTIR in the field of nanotoxicology, including higher signal-to-noise ratio, high energy throughput, as well as high accuracy and stability which are applicable to solid phase samples but not recommended for assays in the liquid phase. Limitations such as multiple background scans and post processing analysis are not deniable.

Comparison of FTIR with other commonly used tools such as raman spectroscopy, mass spectrometry, nuclear magnetic resonance spectroscopy, and X-ray photoelectron spectroscopy are also discussed. Finally, we present an application of FTIR for the assessment of bacterial changes in response to the exposure to silver nanoparticles (AgNPs). The results showed that the AgNPs-induced structural changes in the peptide and amino acids region may lead to alterations of conformation and/or composition of Amid B and Amid III. These results showed that bacteria developed resistance toward AgNPs and resulted in changes in the genotype and expression in

the phenotype. Here, ATR–FTIR provided the evidence of the AgNPs cytotoxicity induced intracellular level alterations in bacteria.

1- Introduction

Rapid and specific analytical tools to characterize the interactions between bacteria and nanoparticles are essential for the development of safe and effective nanomaterials. These tools can also help to prevent the unintentional negative effects that nanomaterials could have on ecosystems and public health. Broad spectrum molecular analytical tools based on infrared (IR) spectroscopy were introduced in the 1950s (Levine et al. 1953; Riddle et al. 1956; Kenner et al. 1958). After making several improvements to IR tools, researchers in the 1970s developed Fourier transform IR (FTIR) spectroscopy based on a new computational analysis, which led to Naumann and Helm (Helm et al. 1991; Naumann et al. 1991) introducing the FTIR technique for *in-situ* analysis of bacteria. FTIR can identify molecular signatures in bacteria composition due to the absorption of energy in the infrared region. Biochemical bonds are detected based on their molecular rotational degree and type of movement, such as stretching (Picquart et al. 2000; Nydegger et al. 2011), bending (Nydegger et al. 2011; Podstawka-Proniewicz et al. 2011), scissoring (Picquart et al. 2000; Podstawka-Proniewicz et al. 2011), or twisting (Picquart et al. 2000; Nydegger et al. 2011).

FTIR techniques were applied to identify bacteria (Levine et al. 1953; Riddle et al. 1956; Kenner et al. 1958; Whittaker et al. 2003) and classify (Helm et al. 1991; Mariey et al. 2001) bacterial strains through the use of spectral libraries for each type of bacteria (Mauer et al. 2008). These libraries are available as a package through

various scientific companies. Furthermore, several studies have shown the capability of FTIR to differentiate between intact and injured cells in stress conditions (Lin et al. 2004; Lorin–Latxague and Melin 2005; Al-Qadiri et al. 2008b; Al-Qadiri et al. 2008a; Alvarez-Ordóñez et al. 2010; Liu et al. 2011).

Recently, FTIR has been used to characterize bacteria exposed to nanoparticles (Nadtochenko et al. 2005; Kiwi and Nadtochenko 2005; Fang et al. 2007; Hu et al. 2007; Yuan et al. 2008; Jiang et al. 2010; Riding et al. 2012; Fang et al. 2012; Gurbanov et al. 2015). For instance, FTIR has been used to determine bacterial structural changes after exposure to different types of nanomaterials, such as oxides (Nadtochenko et al. 2005; Kiwi and Nadtochenko 2005; Hu et al. 2007; Jiang et al. 2010), quantum dots (Fang et al. 2012), and organic nanoparticles (Riding et al. 2012).

From a biochemical perspective, it is important to determine interactions at the molecular level as they could provide fundamental information on the effects observed at a systemic level. Due to the technological advances, simplicity of the sample preparation, and high speed of analysis, FTIR spectroscopy could fill the growing demand of fast and reliable toxicity screening in the field of nanotoxicology.

1.1- Overview of FTIR fundamentals

The emitted radiation from an IR source passes through an interferometer composed of a beam-splitter, a fixed mirror, and a moving mirror (Fig. 1). The interferometer measures the wavelength of emitted light *via* interference patterns that help to increase accuracy. IR spectra are obtained by applying IR radiation to a sample and measuring

the intensity of the passing radiation at a specific wavenumber (Fig. 1). The number of scans can be adjusted based on the quality requirement for the sample analysis; currently, the most common number of scans used is 2^8. IR radiation of certain molecular groups can be detected at a specifics wavenumbers. The x-axis of the spectrum represents the wavenumber while the y-axis represents absorbance or transmittance (Nadtochenko et al. 2005; Kiwi and Nadtochenko 2005; Corte et al. 2010).

The most common FTIR based methods for bacteria characterization are transmittance FTIR, attenuated total reflectance (ATR-FTIR), and micro-spectroscopy FTIR.

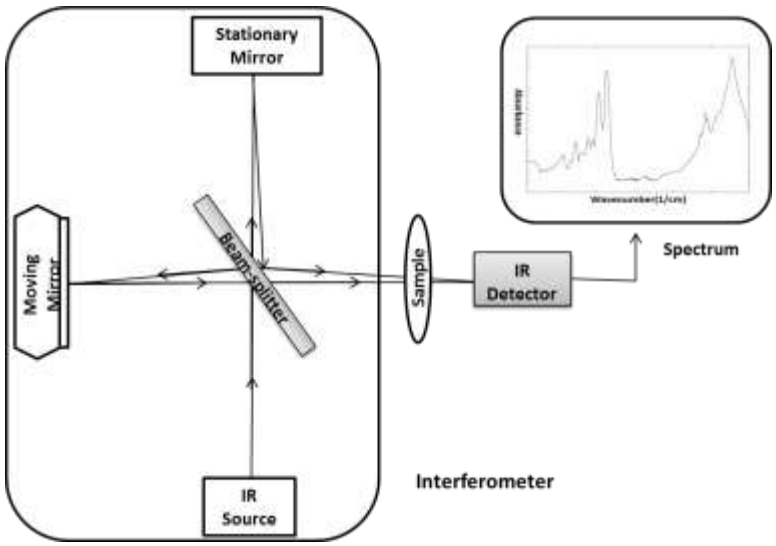

Fig. 1: Schematic components of FTIR spectroscopy, the IR source generates radiation which passes the sample through the interferometer and reaches the detector.

1.1.1- Transmittance FTIR

FTIR analysis can be carried out in solid, liquid or gas samples, however here only solid and liquid phase sample applications will be discussed. Solid samples should be ground with potassium bromide (about 5% of the weight of the sample) and pressed to

form a hard pellet. Then the sample is placed between two infrared-transparent plates. There are various types of transparent material used to analyze different types of samples. For liquid samples, selected compatible IR transparent windows could be zinc selenide or diamond glasses are more appropriated. In both cases, the IR beam passes through the sample, as previously described. The low noise-to-signal ratio in samples makes the transmittance method advantageous because the pressed sample has a low number of random fluctuations of the baseline, resulting in higher sensitivity (Coates 2006). The limitations of this method include that the absorption sensitivity varies within a sample containing different thicknesses as well as the required time for sample preparation.

Transmittance FTIR has been used to monitor bacterial properties and composition in growth and non-growth (Moen et al. 2005) conditions, such as osmotic stress (Beney et al. 2004; Moen et al. 2009), temperature shock (Mille et al. 2002; Moen et al. 2009; Alvarez et al. 2010), pH tolerance (Papadimitriou et al. 2008; Moen et al. 2009; Alvarez et al. 2010), chemical shock (Feo et al. 2004; Hu et al. 2007; Moen et al. 2009; Alvarez et al. 2010), UV light (Schleicher et al. 2005), and ultra-strong static magnetic fields (Hu et al. 2009). Likewise, the FTIR transmittance technique was used to study toxicity effects of selenium on *Escherichia coli* (*E. coli*) (Feo et al. 2004) and the exposure of *E.coli* and *Staphylococcus aureus* membrane a sequence of photocatalytic degradation followed by Ag/TiO_2 nanoparticle suspension (Hu et al. 2007).

1.1.2- Attenuated Total Reflectance (ATR)

For ATR-FTIR, a sample volume between 20 µL and 200 µL can be either directly transferred or dried and placed onto a crystal surface (Winder and Goodacre 2004; Burgula et al. 2006) that can be made from various materials with unique refractive index relative to the sample (Lasch and Naumann 2000). The effective factor regarding the ATR analysis is the refractive index of the sample, which should be lower than the crystal sample holder. Depending on the type of sample, various crystal surfaces exist (Lasch and Naumann 2000; Winder and Goodacre 2004; Burgula et al. 2006). The penetration ability of the IR beam through the sample is approximately 300 nm i beyond the surface of the sample. In some cases, to prevent interference from bulk water, a probe can be used to bring the IR beam directly onto the sample. A limitation of this methodology is that the resolution can decrease at higher wavelengths compared to the transmission mode due to higher background noise. However, because bacteria signatures are observed in the mid-IR, this limitation does not apply for bacteria analysis. To analyze bacterial samples by ATR-FTIR, bacteria are separated from the liquid sample by membrane filtration. Some of the types of membranes used for bacteria filtration include Metrical TM (Burgula et al. 2006), polyethylene (Mossoba et al. 2003), anodisc (Rodriguez-Saona et al. 2004), and aluminum oxide (Al-Holy et al. 2006).

ATR-FTIR has also been used to study the toxicity effect of various nanoparticles, such as ZnO, quantum dots (Fang et al. 2012), and carbon nanomaterial (Riding et al. 2012). For example, Wang et al. used ATR-FTIR to characterize the effect of nanowire photocatalysis on *E. coli*. Through ATR-FTIR, it was shown that structural

changes occurred in the membrane composition of treated cells, indicating increased cell permeability. In addition, Fang et al. investigated the toxicity effect of various quantum dot nanoparticle sizes on *E. coli*. Changes in membrane structure in treated *E. coli* indicated that the toxicity effect of quantum dots depends on size, where smaller nanoparticles produce a high inhibitory effect (Fang et al. 2012). Likewise, Riding et al. (Riding et al. 2012) studied the toxicity effect of long and short multiwall carbon nanotubes on gram-negative bacteria. The authors reported that the bactericidal effect of carbon nanotubes depends on their size, with shorter tubes resulting in greater toxicity than longer ones based in term of revealed signature of lipids, amide II, and DNA components in treated cells.

1.1.3- FTIR micro-spectroscopy

FTIR micro-spectroscopy is the most recent FTIR technique and combines a FTIR spectrometer and a microscope to obtain information through the spatial and chemical spectral information simultaneously (Lasch and Naumann 2000; Garidel and Boese 2007; Beekes et al. 2007). Sample preparation for micro-spectroscopy is performed by either drying a diluted sample directly on a IR transparent plate or pressing the IR transparent plates to a bacterial colony, which is called the “replica stamping technique” (Lasch and Naumann 2000). With this imprinting technique two to three bacterial layers can be placed on the plate. For both methods, the benefit is that it allows concentrating the IR radiation on the sample and collecting an accurate spectrum. It can also be applied to both, the transmission or attenuated total reflection mode (Garidel and Boese 2007). While micro-spectroscopy FTIR has limited spatial

resolution, identifying bacteria through this accessory is not limited by this fact as they have distinct levels of morphologic heterogeneity (Lasch and Naumann 2000).

Previous studies have reported several applications of FTIR micro-spectroscopy, including the heterogeneity during growth in *Legionella bozemanii, Bacillus megaterium,* and *Candida albicans* colonies (Thi and Naumann 2006) as well as *E. coli* activities in biofilms (Holman et al. 2009), endospores' bacteria changes after autoclaving (Perkins et al. 2004), differences between intact and dead *E. coli* (Davis et al. 2010), live and heat-treated *Salmonella Typhimurium* in chicken breast (Davis and Mauer 2010), the effect of membrane fluidity on resistance to high hydrostatic pressure in *Listeria monocytogenes* (Karatzas and Bennik 2002), and misfolding and aggregation changes of *E. coli* membranes in the presence of recombinant proteins (Ami et al. 2009). FTIR micro-spectroscopy was also used to investigate the effect of a fullerene-based nanomaterial on *Bacillus subtilis* and *Pseudomonas putida* membranes (Fang et al. 2007). The study found that the membrane fluidity and lipid composition depend on the nanomaterial concentration and the composition of the cell wall (Fang et al. 2007).

In general, the observed intensity of the absorption bands along the ATR-FTIR spectrum is less than the transmitted FTIR spectrum. The main difference between transmittance FTIR and ATR-FTIR is their depth of penetration. Transmittance FTIR measures a spectrum that is an average of the bulk properties of the sample; however, ATR-FTIR can only probe through samples up to 300 nm in thickness (Lasch and Naumann 2000; Winder and Goodacre 2004; Burgula et al. 2006). These two methods differ as well in sample preparation requirements. In the case of ATR-FTIR, the

sample is directly placed on to the crystal surface, but for transmittance FTIR, the sample must be placed between two transparent glass (Lasch and Naumann 2000; Winder and Goodacre 2004; Burgula et al. 2006).

1.2- Advantages, disadvantages, and limitations

All FTIR techniques present advantages and disadvantages for the analysis of bacteria exposed to stress conditions, such as exposure to nanoparticles. FTIR is a time-efficient technique because the sample preparation is simple (Carlos et al. 2011), the time needed to obtain the spectral analysis is short (Davis and Mauer 2010), and samples can be analyzed in different states (liquid or solids) (Mouwen et al. 2005; Burgula et al. 2007; Mauer et al. 2008;). In addition, only small amounts of the sample are required for analysis—usually in the order of µg (solids) or µL (liquid) (Meier 2005; Davis and Mauer 2010), and the method is usually not destructive (Lin et al. 2004). FTIR is also less expensive for bacterial identification compared to other commonly applied methods (Davis and Mauer 2010). Moreover, FTIR has three remarkable advantages: (1) higher signal-to-noise ratio, (2) high energy throughput, and (3) high accuracy and stability. A higher signal-to-noise ratio is possible because the wavelengths are measured simultaneously, which is called “Fellgett advantage”. Prevention of the light dispersion in FTIR causes high energy throughput which is called the “Jacquinot advantage”. Regarding accuracy and stability, a remarkable advantage of FTIR is the use of a HeNe (helium neon) laser which acts as an internal reference for each scan and provides accurate and stable wavenumber scales of an interferometer which is referred to as the “Connes advantage”. These three properties

of FTIR are effective for nanotoxicoly assays performed (Naumann 2006). All of these three properties of FTIR are effective in the solid phase rather the liquid phase of nanotoxicological studies.

However, there are also disadvantages. Multiple background scans and sample scans are necessary to avoid artifacts and variations in the spectra due the surrounding environmental conditions in sample heterogeneity. For instance, measuring the sample in culture media at different temperatures can influence the FTIR spectra of the sample (Cadet and de la Guardia 2000). Pretreatment of the samples may be required to purify the sample and to prevent peaks from overlapping on the spectra. For example, water from bacteria samples in liquids can overlap the band of amide compounds and produce a loss of information due to the large absorption of water molecules in the 1637 cm^{-1} wavenumber (Lasch and Naumann 2000). In some cases, this can be avoided by preparing a dried solid sample. To identify strains of bacteria, a library for characterization and identification is required, however this can be purchased from various scientific companies. Finally, the raw data can require extensive post-processing analysis.

1.3- Additional tools to complement FTIR analysis in observing changes in intracellular composition

FTIR limitations can be compensated for by combining the analysis with other techniques. The most commonly used techniques to determine the composition of bacteria include raman spectroscopy, mass spectrometry, nuclear magnetic resonance spectroscopy (NMR), and X-ray photoelectron spectroscopy.

1.3.1- Raman Spectroscopy

FTIR and Raman spectroscopy have similar fundamentals as they are both inelastic scattering tools that provide a molecular fingerprint of materials based on the vibration of their molecules (Kollias and Stamatas 2002). In Raman spectroscopy, a monochromatic light illuminates to the samples. The interactions of the impinging photons with the sample cause changes in the frequency of photons in monochromatic light. The inelastic transfer of energy then causes the frequency of the reemitted photons to shift in comparison with original monochromatic frequency. These shifts obtain information about molecular vibrational, rotational, and other low frequency transitions (Colthup 2012), which are called Raman effects. The elastic transfer of energy, or Rayleigh scattering, dominates the outputs of Raman spectroscopy. Therefore, in order to access Raman spectroscopy, the outputs of Raman spectroscopy require filtration by notch or band pass filters before further analysis (Colthup 2012).

The main benefit of Raman spectroscopy is that it requires less sample preparation compared to some FTIR modest (Colthup 2012). Although Raman spectroscopy is highly sensitive to some molecular vibrations (Larkin 2011), ambient noise, such as fluorescence, can interfere with the ability to obtain an accurate Raman spectra (Parker 1983).

Raman spectroscopy has been used to investigate the toxic effect of nanoparticle exposure to microorganisms and tracking the location of the nanoparticles with cells (Shah et al. 2011; Lamprecht et al. 2012). Examples on exposure of live virus to Ag and Fe_3O nanoparticles (Candeloro et al. 2011), quantifying the ratio of oxidized cysteine to total protein, and lipid unsaturation levels in viruses (Li et al. 2013; Li et

al. 2015), and determining the location of the nanomaterial inside the microorganism (Shah et al. 2011; Lamprecht et al. 2012).

Raman spectroscopy has it combined with FTIR can provide valuable data about the microorganism's interactions with nanoparticles as well as nanoparticle characterization. This is possible because Raman and FTIR spectroscopies are sensitive to homo-nuclear (C-C, C=C and C≡C bonds) and hetero-nuclear (OH stretching in water) functional groups, respectively (Larkin 2011).

A combination of FTIR and Raman spectroscopy has been used to characterize the nanohybrid composition of silver-coated carbon nanotubes to study their antimicrobial properties (Yuan et al. 2008). Here the combined methods were used to show the successful grafting of AgNPs with amine groups onto carbon nanotubes (Yuan et al. 2008).

1.3.2- Mass Spectrometry

Mass spectrometer characterizes the mass of a molecule by determining the mass-charge ratio (*m/z*) of its ion. Ions are produced by enforcing either the loss or gain of a charge from a sample, called the ionizing process. The ionizing process can be performed through electron bombardment, which produces the charged molecules (ions) of chemical compounds in a sample. Ions are electrostatically guided into a mass analyzer in which they are separated according to their mass-charge ratio and characterized. The results of molecular ionization, ion separation, and ion detection can be observed by a spectrum that provides molecular mass and structural information (Lay 2001).

A specific advantage of mass spectrometry over FTIR is the capacity to quantify the structural information, although the data collected by mass spectrometry is difficult to interpret (Gopal et al. 2013). On the other hand, the analysis of compounds with multiple functional groups is very difficult when using mass spectrometry (Fang et al. 2007; Gopal et al. 2013). Some examples of assessing toxicity effects of nanoparticles via mass spectrometry include a study focused on characterizing the interactions of bacteria with five types of nanoparticles (Gopal et al. 2013). This study determined the preferential binds between peptide fragments and surface coating of silver nanoparticles (Wigginton et al. 2010) and quantified the formation of ox datively induced DNA lesions in different types of cells exposed to gold nanoparticles (Nelson et al. 2013).

Mass spectrometry and FTIR are tools that are often used in conjunction; FTIR provides an outlook into the structural overview of bacterial toxicity whereas mass spectrometry offers a ratio of molecular bonds (Fang et al. 2007). For example, Fang et al. investigated the impact of buckminsterfullerene (C_{60}) on membrane properties on gram-positive and -negative bacteria (Fang et al. 2007). In this study, FTIR showed that the frequency of -CH_2 stretching increased due to the high concentration of nanomaterials, which means the fluidity of the membrane was increased in treated cells. Mass spectrometry also showed that the proportions of monounsaturated fatty acids in treated bacteria increased significantly compared to the controls (Fang et al. 2007).

1.3.3- Nuclear magnetic resonance spectroscopy (NMR)

NMR characterizes the physical and chemical properties of certain atomic nuclei. As all electrically charged nuclei have an associated spin, the applied external magnetic fields transfer energy at a specific wavelength from the base energy to a higher energy level. The wavelength corresponds to radio frequencies; hence, when the spin returns to its base level, energy is emitted at the same frequency, and the released signal results in a NMR spectrum for the nucleus (Shah et al. 2006).

NMR spectroscopy can determine the molecular structure, content, and purity of a sample. NMR can detect an unknown compound's molecular structure and match it against spectral libraries or directly infer them from basic structures of molecules (Serber and Dötsch 2001). In the case of known compounds, NMR can characterize the molecular structure as well as physical properties at the molecular level. These properties include structural changes, phase changes, solubility, and diffusibility (Serber and Dötsch 2001).

In order to analyze more complex materials such as bacteria (Serber and Dötsch 2001), NMR is more appropriate than the previously mentioned techniques. Some advantages of this tool are versatile identification in terms of material composition and high chemical sensitivity (Shah et al. 2006). NMR can measure the long-range hetero-nuclear distances, which can be used to measure a distance between an antibiotic and a specific site in the membrane (Cegelski 2015). In addition, NMR can determine protein structures, and the location of every atom in the space (Schanda et al. 2014). One of the disadvantages is that NMR has the potential to change the genetic code of

bacteria and consequently the behavior of the protein, due to the use of synthetized amino acids for labeling (Reckel et al. 2005).

Several studies have used NMR to measure the effectiveness of antimicrobial agents on intact *E. coli* without mutation or on mutated strains deficient in total fatty acid biosynthesis (Davis et al. 1979; Pius et al. 2012; Tardy-Laporte et al. 2013), as well as study the adaptation mechanisms of bacteria to peptides (Chia et al. 2000), or detect peptidoglycan composition and define the interactions with *Staphylococcus* aureus (Romaniuk and Cegelski 2015).

The combined NMR and FTIR approach was applied to investigate the interaction of different structures of peptides (α-helices and β-sheets) with the bacterial membrane and its diastereomer (Oren et al. 2002). NMR revealed the interactions between peptides within membranes, while FTIR characterized the composition of α-helical structures within the peptide. NMR also detected the ratio of α-helical and β-sheets within membranes. The combined approach showed which peptide organized more selectively with the membrane (Oren et al. 2002).

To our knowledge, no study has used NMR and FTIR combined for nanotoxicology. However, NMR as well as FTIR supports the identification of functional groups' alterations in bacteria (Davis et al. 1979; Pius et al. 2012; Tardy-Laporte et al. 2013). A spectrometric analysis of bacteria exposed to nanoparticles by NMR can provide comprehensive information about the molecular composition of cells and complement the FTIR results.

1.3.4- X-ray photoelectron spectroscopy (XPS)

In XPS, photoelectrons are emitted from the sample surface due to excitation with mono-energetic Al kα x-rays. The energy of emitted photoelectrons is measured by an electron energy analyzer. The photoelectron peak determines the binding energy and intensity of the elemental identity, chemical state, and quantity of an element. XPS has different detection limits and analysis depths to detect the chemical composition of different cells (Rouxhet et al. 1994; Dufrêne and Rouxhet 1996; Dufrêne et al. 1997; Yan et al. 1997; Beech et al. 1999; van der Mei et al. 2000; Bruinsma et al. 2001; Omoike and Chorover 2004; Pradier et al. 2005; Ojeda et al. 2008).

XPS determines the presence of elements and the composition of functional groups, such as proteins and polymeric substances on the cell surface (Rouxhet et al. 1994; Dufrêne and Rouxhet 1996; Dufrêne et al. 1997; Yan et al. 1997; Beech et al. 1999; van der Mei et al. 2000; Bruinsma et al. 2001; Omoike and Chorover 2004; Pradier et al. 2005; Ojeda et al. 2008). XPS can also estimate the concentrations of the bacterial surface compounds within 5 nm from the sample surface (Ahimou et al. 2007; Hamadi et al. 2008; Ojeda et al. 2008). These include functional group identification of polysaccharides, peptides, and hydrocarbon compounds with the use of a constituent model (Dufrêne et al. 1997; Ahimou et al. 2007; Ramstedt et al. 2011). XPS has been used to identify the accurate composition of polymer surfaces and their adhered biomolecules (Tyler 1997) as well as to study cell−substratum interfaces (Boonaert et al. 2001). Moreover, XPS identified the gram-negative *Aquabacterium* surface properties, including surface charge, acid−base behavior, chemical composition, and changes of the organic functional groups at different pH values (Ojeda et al. 2008).

The main limitation of XPS is the effective depth of the cell surface, which limits the application of this technique to extracellular analysis (Sprenger and Anderson 1991). This technique can provide the quantitative elemental analysis of all elements, except hydrogen and helium, both of them which are generally free of matrix effects and decrease quantitative accuracy (Dufrene et al. 1997; Ojeda et al. 2008; Rouxhet et al. 1994; Yan et al. 1997; Dufrene and Rouxhet 1996; Beech et al. 1999; Omoike and Chorover 2004; Pradier et al. 2005). Other disadvantages of this technique are that hydrogen cannot be detected by XPS and the requirement for a high vacuum, which results in a slow characterization process (8 hours). Finally, the deconvolution of XPS peaks should be carried out with extreme care because these peaks are notorious for leading to spurious results (Sprenger and Anderson 1991). Even though these limitations, this technique is useful analyzing bacterial surface interactions because of quantitative measurement and chemical bond identification based on elemental characterization (Leone et al. 2006; Hamadi et al. 2008).

In terms of studying toxicity effects, XPS has been applied to characterize the nanoparticle surface properties, such as characterizing the surface coating of Ag-TiO_2 nanoparticles and then complementing this analysis by studying the bactericidal effect of these nanoparticles via FTIR (M. Lopez Goerne, 2011).

2- Bacteria-nanoparticles interactions at the molecular level measured by FTIR

Several possible antimicrobial mechanisms have been detected using FTIR: 1) nanoparticles may change the fluidity of cell wall lipids by binding with -CH groups

of the membrane (Nadtochenko et al. 2005; Kiwi and Nadtochenko 2005; Fang et al. 2007; Hu et al. 2007) measured at 3100–2800 cm^{-1}; 2) the binding of nanoparticles, or ions released from nanoparticles, with amino acids in proteins and enzymes (Eckhardt et al. 2013), which changes the protein structures detectable at 1500–1800 cm^{-1} [16]; 3) nanoparticles bound to phosphate groups of nucleic acids in DNA or RNA altering their structures, which are detected in the 600–1200 cm^{-1} wavenumber range (Jiang et al. 2010; Eckhardt et al. 2013); and 4) nanoparticle catalyzed oxidation mechanisms and generation of reactive oxygen species (ROS) (Eckhardt et al. 2013), which can cause alterations in polysaccharide structures measured in the 900–1200 cm^{-1} wavenumber (Jiang et al. 2010) range. The chemical properties of bacteria exposed to nanoparticles can be determined from previous studies that introduced the specificity of the altered chemical groups (Nadtochenko et al. 2005; Kiwi and Nadtochenko 2005; Hu et al. 2007; Fang et al. 2007; Jiang et al. 2010; Fang et al. 2012; Riding et al. 2012). As previously mentioned, FTIR is able to reveal different biochemical properties of bacteria based on their chemical bonds[1–12] and structural changes (Zeroual et al. 1994). The biochemical structural alterations of bacteria exposed to nanoparticles can be characterized in four regions by tracking FTIR fingerprints (Nadtochenko et al. 2005; Kiwi and Nadtochenko 2005; Hu et al. 2007; Fang et al. 2007; Jiang et al. 2010; Fang et al. 2012; Riding et al. 2012). These regions are mainly placed between 3100 and 2800 cm^{-1} for fatty acids, 1800 and 1500 cm^{-1} for proteins and peptides, 1200 and 900 cm^{-1} for carbohydrates, and 900 and 600 cm^{-1} for the fingerprint region (Lasch and Naumann 2000). The impacts of nanoparticles in each of these regions are described below.

2.1- Fatty acid region

The chains of several bacterial membrane amphiphiles (e.g., phospholipids) and side-chain vibrations can be characterized by the peaks in the region around 3100-2800 cm^{-1}, which are observed due to the -CH stretching vibrations of CH_3, CH_2, and CH functional groups (Naumann et al. 1991; Lasch and Naumann 2000). The bands in 2955 cm^{-1}, 2930 cm^{-1}, 2898 cm^{-1}, 2870 cm^{-1}, and 2850 cm^{-1} wavenumbers are responsible for -CH asymmetric stretching of -CH_3 in fatty acids, -CH asymmetric stretching of >CH_3 in fatty acids, -CH stretching of ≥-CH of amino acids in fatty acids, -CH symmetric stretching of -CH in fatty acids, and -CH symmetric stretching of CH_2 in fatty acids, respectively (Lasch and Naumann 2000). Sometimes a peak at 3015 cm^{-1} was reported as a responsible band for stretching CH double bonds in unsaturated fatty acid chains (Lasch and Naumann 2000).

Fatty acids' spectral bands between 3100 and 2800 cm^{-1} (Sivakesava et al. 2004; Mura et al. 2012) can determine the severity of the nanoparticles' impact on the bacterial wall. The resolved peaks in the majority of published articles characterized the differences between bacterial fatty acids' profiles in the presence of nanoparticles and untreated bacteria (Nadtochenko et al. 2005; Kiwi and Nadtochenko 2005; Hu et al. 2007; Fang et al. 2007; Fang et al. 2012). Membrane peroxidation in *E. coli*-exposed TiO_2 photocatalysis was detected through modifications of bands at 2958 cm^{-1}, 2924 cm^{-1}, 2876 cm^{-1}, and 2854 cm^{-1}, which were caused by -CH asymmetric stretching of -CH_3 in fatty acids, -CH asymmetric stretching of >CH_3 in fatty acids, and -CH symmetric stretching of CH_2 in fatty bands (Nadtochenko et al. 2005; Kiwi and

Nadtochenko 2005). Similarly, Hu et al. reported that the main alteration in the fatty acid region included reduced peak intensity of the -CH bands at 2872 cm^{-1} and 2852 cm^{-1} as well as undetectable bands at 2963 cm^{-1} and 2927 cm^{-1} in bacteria exposed to AgI/TiO_2 nanoparticles for 6 hours (Hu et al. 2007). Also, Fang et al. observed changes after exposing *E. coli* to different sizes of the CdTe quantum dot nanoparticles (Fang et al. 2012). They characterized the intensity of bands at 2958 cm^{-1}, 2925 cm^{-1}, and 2854 cm^{-1} and found that peaks were smaller in treated bacteria compared to the control. The authors reported that the alterations in -CH of the fatty-tail structure is the cause of smaller peak intensity at these wavenumbers. Furthermore, they found that the -CH band at 2873 cm^{-1} disappeared after treating bacteria with the small size of CdTe quantum dots. Also, they detected that the effects of the ZnO nanowire photocatalysis were characterized in the fatty acid regions by the decreased bands at 2852 cm^{-1}, 2924 cm^{-1}, and 2959 cm^{-1}, indicating the changes in -CH of the fatty-tail structure. Moreover, other studies focusing on bacteria treated with different concentrations of fullerene-based nanomaterials reported that a decreasing intensity ratio of CH_2 vibration indicates the alteration of membrane fluidity (Fang et al. 2007). A modification of the -CH vibration on the exposed bacterial profile are interpreted as bacterial lysis (Nadtochenko et al. 2005; Kiwi and Nadtochenko 2005; Hu et al. 2007; Fang et al. 2007; Fang et al. 2012), thereby indicating an increase in the lipid-layer fluidity of the bacterial cell walls. The enhanced fluidity of the lipopolysaccharides cause a leakage in the cell membrane (Losasso et al. 2014) that has been reported due to the peroxidation in the case of polar-saccharide moieties (Naumann et al. 1989).

Additional information for the fatty acid region can be derived from the responsible bands for -CH deformation in the 1500–1200 cm^{-1} area (Bellamy 1975; Lasch and Naumann 2000; Davis and Mauer 2010). The bands around 1367 cm^{-1}, 1354 cm^{-1}, and 1341 cm^{-1} are responsible for the vibrations of methylene fragments in the kink (gauche-trans-gauche), double-gauche, and end-gauche conformations, respectively (Lewis et al. 1994; Cieslik-Boczula et al. 2008). After bacterial exposure to oxide nanoparticles, the band at 1341 cm^{-1} disappeared and intensive bands at 1362 cm^{-1} were observed (Jiang et al. 2010), indicating a low concentration of the vibrations of methylene in end-gauche conformers as well as a combination of vibrations of methylene in gauche-trans-gauche and double-gauche conformers, respectively (Lewis et al. 1994; Cieslik-Boczula et al. 2008). Hu et al. reported that the increase in the concentration of carboxylic groups was due to the appearance of bands at 1408 cm^{-1} and 1337 cm^{-1}. They concluded that the photocatalytic degradation of the cell membrane causes the formation of carboxylic acid (Hu et al. 2007). In addition, some spectral changes were reported near 1414 cm^{-1} and 1390 cm^{-1}, indicating the unsaturated aldehydes due to the deformation of the hydroperoxides or lipid endoperoxides and the appearance of C=O stretching bonds (Gericke and Huehnerfuss 1995).

In the case of characterizing alterations in the phospholipids of nanoparticle-exposed bacteria, bands for the PO^{-2} asymmetric stretching of phosphodiesters in phospholipids should be detected near 1280–1200 cm^{-1}. Based on various studies, phosphate groups on the FTIR spectra demonstrated the decrease in peak intensity around 1232 cm^{-1} (Fang et al. 2012) or 1234 cm^{-1} bands due to the sensitivity of the hydration–

dehydration of the phosphoric groups in lipids structures (R. KINDER and WESSELS 1997; Davis and Mauer 2010). This mechanism is responsible for the change in permeation in terms of the depletion in ATP levels (Eckhardt et al. 2013) that has been reported as a nanoparticles' impact on bacteria (Nadtochenko et al. 2005; Kiwi and Nadtochenko 2005; Hu et al. 2007; Fang et al. 2007; Fang et al. 2012). Moreover, Riding et al. claimed that the decreased peak at 1238 cm^{-1} in the carbon nanotube-treated bacteria indicated the inhibition of releasing free ROS (Riding et al. 2012).

Moreover, other wavenumber regions were reported for phospholipid and phosphodiester compounds. For instance, a decreased intensity of peaks was reported for phospholipid and phosphodiester compounds around 1080 cm^{-1}, suggesting the peroxidation of the hydrophobic end. They also reported the appearance of two bands at 1111 cm^{-1} and 976 cm^{-1} after ZnO nanoparticle exposure, which introduced a signature of the symmetry and asymmetric vibration of deprotonated PO_3^{2-}, suggesting that part of the PO^{2-} groups in phosphodiester was converted into terminal phosphoryl PO_3^{2-} groups. In addition, a new band formed at 937 cm^{-1} after exposure to ZnO nanoparticles might relate to the symmetry vibration of PO_4^{3-} (Persson et al. 1996; Jiang et al. 2004). This band may appear from the deviation of terminal phosphoryl groups caused by the CH_2 wagging spectra.

The destruction of polar-saccharides as a result of ROS generation by nanoparticles caused clear changes in the wavenumbers in the fatty acid region of treated bacteria compared to untreated cell spectra (Nadtochenko et al. 2005; Kiwi and Nadtochenko 2005; Hu et al. 2007; Fang et al. 2007; Fang et al. 2012; Lorin–Latxague and Melin 2005).

2.2- Protein Region

The peaks at 3200 cm^{-1} and 3060 cm^{-1} indicate N-H stretching of amide A and amide B, respectively, in proteins (Naumann et al. 1991; Feo et al. 2004; Beney et al. 2004; Schleicher et al. 2005). Furthermore, the majority of responsible peaks for the protein region mainly include the peaks at 1800 cm^{-1} and 1500 cm^{-1}, which are dominated by the amide I and amide II of proteins and peptides, except the amide III band, which is located around 1280 cm^{-1}. The amide I band components of proteins rise near the 1695–1675 cm^{-1} area. Certain peaks at 1655 cm^{-1} and 1637 cm^{-1} are responsible for the rise in amide I principally due to the stretching vibrations of the C=O groups at α-helical and β-pleated sheet structures of proteins, respectively. Amide II bands of proteins show up in the 1550–1520 cm^{-1} region due to N–H bending with contributions from the C–N stretching vibrations of the peptide group. As previous reports have mentioned, amide I and amide II bands present the predominance of α or β structures (Lasch and Naumann 2000; Beekes et al. 2007). Amino acids can also be detected by FTIR; for instance, tyrosine can be detected by the peak in 1515 cm^{-1} (Naumann et al. 1991; Lasch and Naumann 2000; Maquelin et al. 2002; Yu and Irudayaraj 2005; Beekes et al. 2007). Other amino acids such as aspartate and glutamate demonstrated weak peaks between 1585 cm^{-1} and 1570 cm^{-1} due to the stretching vibration of carboxylate groups (Lasch and Naumann 2000).

Interactions between metal nanoparticles and thiol groups of respiratory chain enzymes and other amino acid groups of bacterial membranes (Liau et al. 1997; Feng et al. 2000) yield to the thought of FTIR's affordability for detecting the alterations of

protein conformation in nanoparticle treated bacteria. The altered peaks caused by protein structural changes were reported in several articles and characterized the differences between the bacterial protein profiles in the presence of nanoparticles and untreated bacteria (Nadtochenko et al. 2005; Kiwi and Nadtochenko 2005; Hu et al. 2007; Fang et al. 2007; Fang et al. 2012; Riding et al. 2012). The spectral profile resulting from bacteria exposed to different sizes of nanotubes based on FTIR analysis indicated the alteration of bands at 1497 cm^{-1} and 1485 cm^{-1}, which were introduced as dominant protein conformational alterations (Riding et al. 2012). Similarly, the decrease in peak intensity was reported at 1639 cm^{-1} and at 1539 cm^{-1}. The authors further claimed a decreased intensity of the amide A band at 3290 cm^{-1} due to the conformational changes of amide groups at the hydrophobic end of the phosphor-lipids. In addition, Hu et al. found a decrease in peak intensity of bands near 1653 cm^{-1} and 1545 cm^{-1} after exposing pathogenic bacteria to AgI/TiO_2 nanoparticles under visible light irradiation (Hu et al. 2007), which indicates that increasing exposure time causes the decrease in the concentrations of amide I and amide II groups (Hu et al. 2007).

Fang et al. reported protein conformational changes in treated gram-negative bacteria exposed to quantum dot nanoparticles[21]. Here, clear decreases of peak intensity were observed after exposure in the spectral peaks at 1645 cm^{-1}, 1540 cm^{-1}, and 3288 cm^{-1}. In another study, where gram-positive bacteria were exposed to oxide nanoparticles, the bands at 1600 cm^{-1} and 1408 cm^{-1} showed increases in peak intensity compared to the control[15]. A possible explanation for the mechanism in the gram positive bacteria exposed to oxide nanoparticles is that the carboxyl group concentrations increased due

to the contribution of the carboxylic groups forming an inner sphere complex with the oxide metal center. Another explanation is that the ester bond of D-alanine branch is connected to the exposed gram-positive bacteria, then detached to form D-alanine acid (Omoike and Chorover 2004). Upon the gram-positive bacteria exposure to oxide nanoparticles, the intensity ratio of β-sheets to α-helices also decreased (Al-Qadiri et al. 2008b). This can be explained by either lower sensitivity of the FITR to detect hydrogen-bonding carbonyl groups which changed the β-sheet structure; alternatively, the β-sheet intensity of the protein may have been diminished due to unfolding (Jr 1995) after interaction with nanoparticles.

Changes in the protein region, such as peaks at 1414 cm^{-1}, as reported by Nadtochenko et al., include the C-O-H in-plane bending of carbohydrates, DNA/RNA backbone, and proteins (Nadtochenko et al. 2005; Kiwi and Nadtochenko 2005). Also, bands at 1390 cm^{-1} may be influenced by the effect of nanoparticles on bacteria due to the C=O symmetric stretching of COO- group in amino acids and fatty acids. Some spectral changes have been reported, corresponding to the formation of the α and β structures of unsaturated aldehydes because of the breakdown process of hydroperoxides or lipid endoperoxides (Gericke and Huehnerfuss 1995). Finally, in another study, changes in the peaks at 1390 cm^{-1} derived a possible explanation based on the presence of nitro-compounds from proteins or enzymes during the bacterial protection mechanisms. These compounds corresponded to the nanoparticle-exposed bacterial resistance mechanisms to decrease the effect of nitrosative stress at the transcriptional level (Park et al. 2009).

The results of the discussed report clarified that the peptide and amino acids, regardless of their position (intracellular or extracellular), were modified in the nanoparticle-treated bacterial FTIR signature.

2.3- Carbohydrates Region

The spectral changes after bacteria exposure to nanoparticles may take place in the 900–1200 cm^{-1} area, which is dominated by C-O-C and C-O ring vibrations in various polysaccharides. In detail, the region of 1120–1140 cm^{-1} relates to the ν(C–O–C) glycosidic linkage (Gue et al. 2001) and peaks around 1153 cm^{-1}, 1117 cm^{-1}, 1102 cm^{-1}, 1058 cm^{-1}, 993 cm^{-1}, and 966 cm^{-1}, corresponding to the ν(C–O) ring, ν(C–O), ν(C–C), and δ(COH) vibrations of carbohydrates (Kačuráková and Mathlouthi 1996).

The profiles of polysaccharide bands after treatment with nanoparticles have been reported with obvious changes (Nadtochenko et al. 2005; Jiang et al. 2010). The bands at 1117 cm^{-1} and 1102 cm^{-1} disappeared in the asymmetric vibration of the C–O–C glycosidic linkage regions, respectively and a new band showed up at 1120 cm^{-1}. Also a decrease in intensity of the broad 1140–1000 cm^{-1} band was detected. These spectral changes to lipopolysaccharides peroxidation can be explained by the composition of the asymmetric outer membrane, amphipathic molecules, or lipo-polysaccharides (Naumann et al. 1989; Kacurakova and Mathlouthi 1996). Another study reported a decrease in peak intensity at 1188 cm^{-1} that corresponds to carbohydrate changes, indicating the occurrence of ROS-induced damage (Riding et al. 2012). Jiang et al. reported in a different study that after exposing bacteria to ZnO nanoparticles, the sugar bands at 1074 cm^{-1} shifted to a lower wavenumber, suggesting the weakening of

the C-O bond due to an increase in the degree of strength of hydrogen bonding with oxides (Jiang et al. 2010).

The negative surface charge of bacteria due to polysaccharides of lipopolysaccharides provides interaction with the positively charged nanoparticles and forms pit structures in the membrane (Rizzello and Pompa 2014). These pit structures could be detected by FTIR in the polysaccharides region because they are formed by disrupting the ß-1→4 glycosidic bonds of the membrane (Eckhardt et al. 2013).

2.4- Fingerprint region

The fingerprint falls between wavenumbers 900 cm^{-1} to 600 cm^{-1} and indicates unique weak bands that correspond to nucleic acids, i.e. phenylalanine, tyrosine, tryptophan, and various nucleotides (Lasch and Naumann 2000). The discrimination of bacteria at the strain level can be performed in the fingerprint region (Davis and Mauer 2010). Bands corresponding to bacterial nucleic acids are not limited to the fingerprint region; two peaks can be observed around 1715 cm^{-1} and 1415 cm^{-1} which are responsible for >C=O stretching of esters in nucleic acids and carbonic acids and C-O-H in-plane bending in the DNA/RNA backbone (Lasch and Naumann 2000).

In bacteria treated with nanoparticles an increased band near 1738 cm^{-1} was observed due to vibration of the C=O carbonyl group. The possible explanation is the peroxidation of nucleic acid chains[128] because of oxidative stress by the generation of ROS (Hu et al. 2007; Jiang et al. 2010; Eckhardt et al. 2013). Hu et al. provided an explanation for the increased peaks at 1690 cm^{-1} and 1734 cm^{-1} in exposed bacteria, which indicate an increase in concentration of C=O bonds in aldehydes and ketones

(Hu et al. 2007). Additionally, due to a pH change in bacteria exposed to nanoparticles, the functional groups of the nucleic acid also undergo changes, which can be revealed in the fingerprint region of the FTIR spectra (Buszewski 2015).

3. Example of ATR-FTIR use for the study of *E. coli* exposure to AgNPs using batch reactors

E. coli K-12 (ATCC 23716), a non-pathogenic strain, was selected for this study. *E. coli* is a gram-negative bacterium that has been found to be metabolically active and has been extensively studied in nanotoxicological research (Zhang and Oyanedel-Craver 2013; Anaya et al. 2015; Schifman et al. 2015). Reagent used to prepare the Lysogeny Broth Miller (LB) growth media consisted of 10 g/L NaCl, 5 g/L yeast extract, and 10 g/L tryptone (Reddy et al. 2007) which it was based on ATCC recommendations. The bacteria were stored in phosphate buffer solution (PBS)—monobasic potassium phosphate, dibasic potassium phosphate, and Ethylenediaminetetraacetic acid (EDTA)—which were all purchased from Sigma Aldrich. Standard casein-coated silver nanoparticles (AgNPs) were obtained from the Argenol Company, Spain.

Microplates with six wells were used to grow bacteria until log phase, measuring the optical density at 600 nm (OD600) every 15 minutes. After 7.5 hours of bacterial growth, suspensions of AgNPs in deionized water were injected to achieve a concentration of 15 mg/L inside of the exposed condition (media plus bacteria+ AgNPs). Controls wells were included to detect contamination (media with no bacteria), and comparison between the non-exposed condition (media plus bacteria)

and exposed condition. After that, plates were run for 7.5 additional hours to assess AgNPs toxicity at 2.5 hours, 5 hours, and 7.5 hours.

Liquid samples were prepared for ATR-FTIR (Nicolet iS50 FTIR, Thermo Scientific) analysis by fixing the optical density (OD600) to 0.8 using a UV−vis spectrophotometer (Genesis, 10UV, Thermo Scientific). Following this, bacteria were centrifuged at 13,000 rpm for 10 minutes, and the supernatant was removed. The pellets were suspended in 10 μL of PBS 10% (Zhang 2013), and the suspension of bacteria with AgNPs was directly placed onto the crystal surface (Gurbanov et al. 2015).

Spectra were the result of 256 scans with a resolution of 4 cm^{-1} in the 4000–350 cm^{-1} spectral range. The data was provided by Omnic software (Thermo Scientific) and processed using Matlab (Mathworks Software).

A unique FTIR spectrum is detected for the AgNP treated bacteria after each contact time (Fig. 2). Increased contact time resulted in decreased peaks in the spectra, where the untreated bacteria had the most intense peaks throughout the spectrum compared to the bacteria exposed for 7.5 hours, which had the weakest intensity peaks. To detect the specific responses within the treated bacteria, the data were analyzed region by region on the spectra.

Fig. 3 shows the spectra for the fatty acid region, including the *E. coli* profile and *E. coli* exposed to AgNPs. The obvious changes were related to shifting due to the deformation of $>CH_2$ and ν_s(C=O) in lipids after 7.5 hours of treatment (Table 1). The change in the asymmetry vibration of phosphate groups also disappeared after 7.5

hours of exposure. The observed changes in the fatty acid region can be due to the alterations in the fluidity of the cytoplasm membrane or cell wall.

Fig. 4 shows the ATR-FTIR spectra in the 1800–1200 cm^{-1} range of the *E. coli* as a control and *E. coli* exposed to AgNPs. The ATR-FTIR protein region peaks of *E. coli* before and after treatment are shown in (Table 2).

The band at 1284.8 cm^{-1} showed increased peak intensity in order to express the presence of amide III components of proteins in untreated *E. coli*. This band was shifted to 1287.3 cm^{-1} after 2.5 hours and 5 hours of exposure, but disappeared after 7.5 hours of exposure. Furthermore, amide A and amide B bands were observed at 3098.6 cm^{-1} and 3277.9 cm^{-1} in the untreated bacterial profile, respectively. However, the greatest shifting happened for the amide B band after 2.5 hours of treatment and remained consistent until 7.5 hours of treatment (Fig. 3 and Table 2).

Bands between 1200 cm^{-1} and 900 cm^{-1} showed the presence of C-O-C and C-O vibrations in the sugar rings in various components of polysaccharides (Fig. 5a). The peaks at 1167.7 cm^{-1}, 1145 cm^{-1}, 968.1 cm^{-1}, and 932.4 cm^{-1} were observed in the untreated *E. coli* spectra. However, after 2.5 hours of exposure to nanoparticles, the peaks appeared in different wavenumbers, such as 1163 cm^{-1}, 1058.4 cm^{-1}, and 932.4 cm^{-1}. The band responsible for ν(C-C) was observed at 1058 cm^{-1} in the spectra after 2.5 hours of exposure. This band was shifted to 1057.3 after 5 hours of treatment time and did not exist in untreated *E. coli*. A major shift was seen because of the ν(C-O) ring for *E. coli* from 1167.7 cm^{-1} to 1163 cm^{-1} after 2.5 hours of exposure and again to 1169.3 cm^{-1} after 5 hours. Despite the fact that the band at 932.4 cm^{-1} was shifted to

916.5 cm^{-1} after 5 hours of exposure, this band did not change after only 2.5 hours of exposure. In addition, a band at 968.6 cm^{-1} appeared in the spectra of untreated *E. coli* and exposed *E. coli* after 5 hours, while the exposed *E. coli* after 2.5 hours did not exhibit this band. All peaks of this region disappeared after 7.5 hours of nanoparticle exposure. The deformation of bacterial cell walls can be the reason of the shifting in the carbohydrate region (Fig. 5a), which shows P=O symmetric stretching in DNA, RNA, and phospholipids bands that shifted from 1064 cm^{-1} in untreated *E. coli* to 1078 cm^{-1} after 2.5 hours and 5 hours of exposure.

In the region between 900 cm^{-1} and 600 cm^{-1}, weak bands appeared (Fig. 5b). The finger print bands of *E. coli* are 824.9 cm^{-1}, 782 cm^{-1}, 665.8 cm^{-1}, and 620 cm^{-1}, which shifted to 827.8 cm^{-1}, 781.5 cm^{-1}, 661.9 cm^{-1}, and 624.3 cm^{-1}, respectively, after 2.5 hours of treatment. Changes were observed in exposed *E. coli* spectra after 5 hours and appeared in the spectrum of treated bacteria at 693.3 cm^{-1}, 643.6 cm^{-1}, and 623.4 cm^{-1}. All peaks in the fingerprint region disappeared after 7.5 hours of treatment.

Some specific peaks showed unique behavior in the fingerprint region. The peak at 644.1 cm^{-1} only appeared in untreated samples and was not seen in any of the treated samples. On the contrary, a band at 881.8 cm^{-1} appeared at 2.5 hours, which was not present in the untreated bacteria, nor did it appear in the 5 hour sample. In contrast, the band at 695.2 cm^{-1} was not changed at all after exposure. The reason for the changes in this region may be due to the alteration of the secondary and tertiary helix structure of DNA, the generation of new gene fragments, or an increase in the transcriptional in the DNA molecule (Hu et al. 2009).

Table 1: Comparison of fatty acids region of untreated *E. coli* and treated *E. coli* with AgNPs at 0 hrs, 2.5 hrs, 5 hrs and 7.5 hrs of treatment using ATR-FTIR

Vibration Mode	E. coli Wavenumber (cm^{-1})	*E. coli*+AgNPs (2.5 hrs) Wavenumber (cm^{-1})	*E. coli*+AgNPs (5 hrs) Wavenumber (cm^{-1})	*E. coli*+AgNPs (7.5 hrs) Wavenumber (cm^{-1})
$\nu_a(CH_3)$	2958.3	2958.3	2957.8	2957.3*
$\nu_a(CH_2)$	2924.5	2924.5	2924.5	2924.5
$\nu_s(CH_3)$	2873.9	2873.9	2873.9	2873.9
$\nu_s(CH_2)$	2853.6	2853.6	2853.6	2853.2
$>CH_2$ deformation	1453.6	1453.6	1453.6	1454.1*
$\nu_s(C=O)$	1393.8	1393.8	1393.8	1394.3
$\nu_a(P=O)$	1235.2	1235.2	1235.2	**

*Peak was shifted to a different wavenumber, **Peak was not observed.

Table 2: Comparison of proteins region of untreated *E. coli* and treated *E. coli* with AgNPs at 0 hrs, 2.5 hrs, 5 hrs and 7.5 hrs of treatment using ATR-FTIR

Vibration Mode	E. coli Wavenumber (cm^{-1})	E. coli+AgNPs (2.5 hrs) Wavenumber (cm^{-1})	E. coli+AgNPs (5 hrs) Wavenumber (cm^{-1})	E. coli+AgNPs (7.5 hrs) Wavenumber (cm^{-1})
Amid A	3277.9	3277.9	3277.9	3277.9
Amid B	3098.6	3088.9*	3089.4*	3089.4*
Amid I	1626.7	1627.6	1627.6	1628.1*
Amid II	1532.6	1533.1	1533.1	1532.6*
Amide III	1284.8	1287.3	1287.3	**

*Peak was shifted to a different wavenumber, **Peak was not observed.

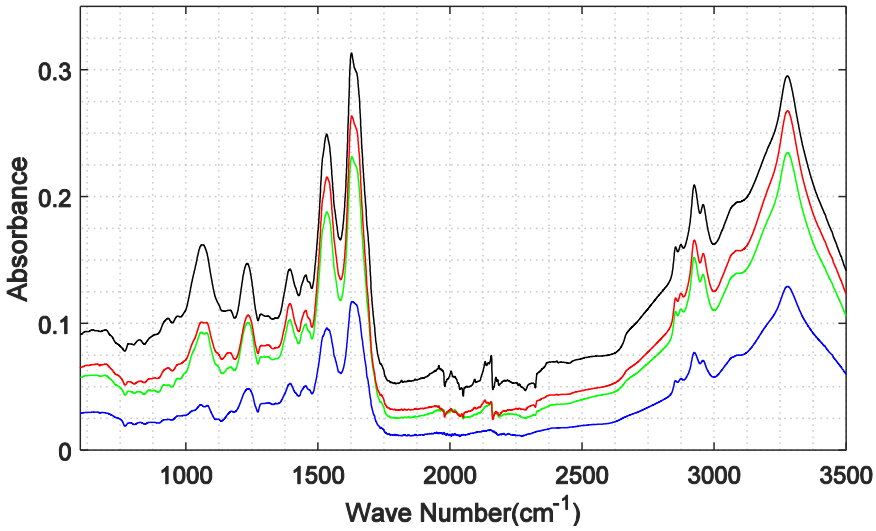

Fig. 2: ATR-FTIR spectra region in untreated *E. coli* (black line), *E. coli*+AgNPs after 2.5 hrs (red line), *E. coli*+AgNPs after 5 hrs (green line), and *E. coli*+AgNPs after 7.5 hrs (blue line)

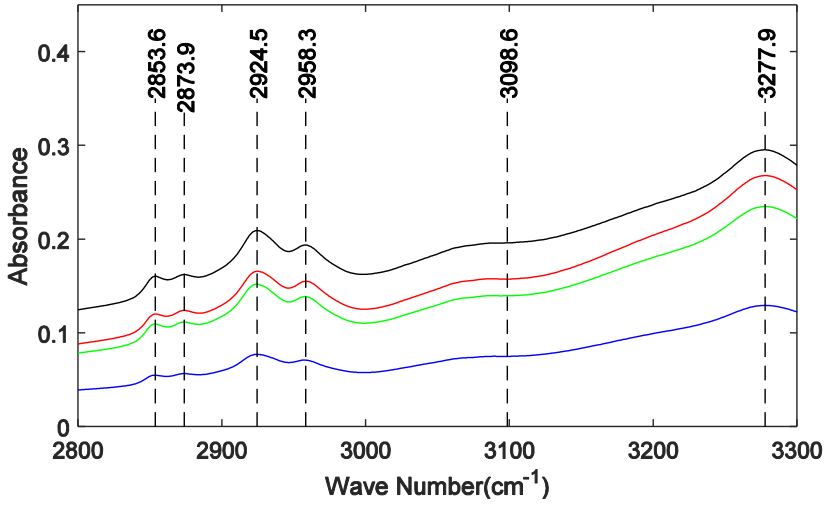

Fig. 3: ATR-FTIR spectra of Fatty acid region in untreated *E. coli* (black line), *E. coli*+AgNPs after 2.5 hrs (red line), *E. coli*+AgNPs after 5 hrs (green line), and *E. coli*+AgNPs after 7.5 hrs (blue line)

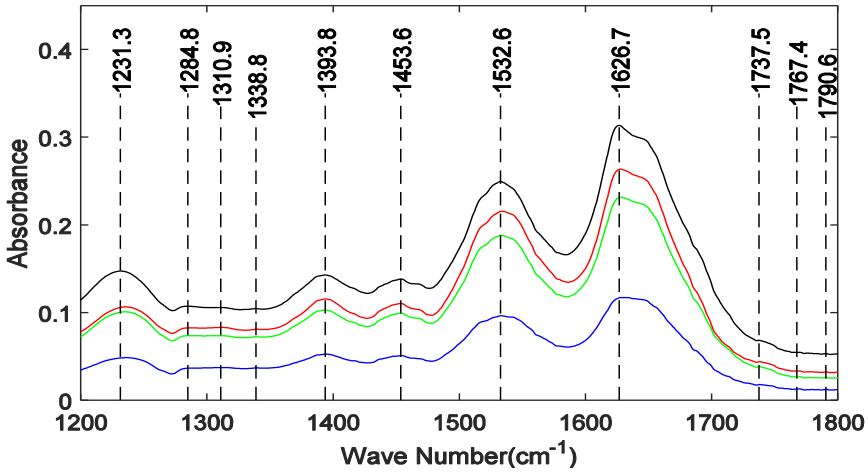

Fig. 4: ATR-FTIR spectra of 1200-1800 cm^{-1} region of untreated *E. coli* (black line), *E. coli*+AgNPs after 2.5 hrs (red line), *E. coli*+AgNPs after 5 hrs (green line), and *E. coli*+AgNPs after 7.5 hrs (blue line)

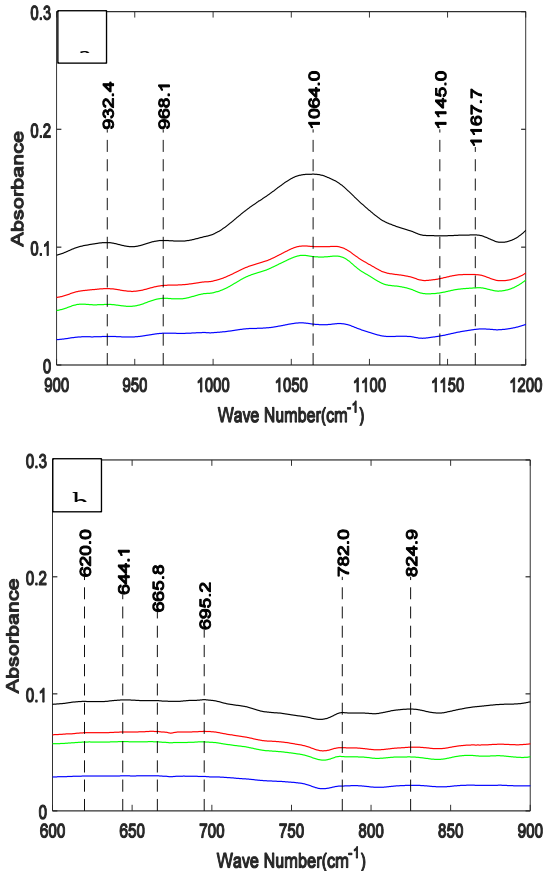

Fig. 5: ATR-FTIR spectra of 900-1200 cm^{-1} and Fig. 5b ATR-FTIR spectra of 900-600 cm^{-1} region of untreated *E. coli* (black line), *E. coli*+AgNPs after 2.5 hrs (red line), *E. coli*+AgNPs after 5 hrs (green line), and *E.coli*+AgNPs after 7.5 hrs (blue line)

The results showed that the spectral regions changed based on the time of exposure after treatment of bacteria with nanoparticles. The results indicated that 7.5 hours showed the most spectral modifications. The most remarkable differences were found in the peptide and amino acids region. This could suggest that part of the ATR-FTIR spectral changes were due to the damage of conformational/compositional alterations in some of the components of the protein structures that could be intracellular proteins or cell wall peptides (Kiwi and Nadtochenko 2005; Jiang et al. 2010). While the

majority of previous studies have focused on membrane alterations (Nadtochenko et al. 2005; Kiwi and Nadtochenko 2005; Fang et al. 2007; Hu et al. 2007), Jiang et al. also reported modifications in the different bacterial strains of protein structures after being exposed to oxide nanoparticles (Jiang et al. 2010). Even though the reference study used oxide nanoparticles (Jiang et al. 2010), the mechanism for modifications in bacterial protein structures may be similar to the toxicity effect observed here. The cytotoxicity effect of oxide nanoparticles onto bacteria was also shown in the proteins region of the bacterial profile. The changes in the intensity ratio of β-sheets/α-helices were reported as a protein structure alteration (Jiang et al. 2010).

The interactions of AgNPs that caused the changes in the fatty acids, specifically -CH deformation, can be the reason for alteration in membrane permeability, which suggests the formation of pits in the bacterial cell wall. Another reason for differences in membrane permeability is the modification at the cellular ATP level, which was observed in exposed bacterial spectra due to the dehydration of phospholipids. In another study where bacteria were exposed to ZnO nanoparticles, the phosphodiester bond was modified in treated cells and formed phosphate monoesters (Jiang et al. 2010). This resulted in highly disordered alkyl chains yielding membrane ruptures and cell leaking (Jiang et al. 2010). The deformation of the fatty acid can be derived from the presence of unsaturated aldehydes during the deformation of hydroperoxides or lipid endoperoxides and the appearance of P=O stretching bands. Other studies also reported the shifting of fatty acids bands due to the toxicity effect of oxide nanoparticles (Nadtochenko et al. 2005; Kiwi and Nadtochenko 2005). These impacts on phosphate groups' stretching may be caused by the ROS, which identify

malfunctions in the respiratory chain enzymes and other membrane proteins and lipophospho-polysaccharids (Jiang et al. 2010).

This study shows that AgNPs can impact the structure and function of proteins (Wigginton et al. 2010; Rizzello and Pompa 2014; Losasso et al. 2014) and can damage nucleic acid molecules (Choi et al. 2008; Graves et al. 2015). The effect of membrane alterations in the treated bacteria was less compared to the observed changes in proteins. Furthermore, slight changes in membrane permeation were detected using epifluorescence stains and extracted lipid monolayers of *E coli* exposed to AgNPs after 5 hours (Anaya et al.). However, even these small changes were enough to damage the outer cell membrane by AgNPs, which causes more entry of AgNPs into the cells could be one of the reasons that AgNPs have cytotoxic effect on *E. coli*(Arora et al. 2008; Wigginton et al. 2010; Zhang and Oyanedel-Craver 2013) while another reason could be that a decrease in ATP levels inside the bacteria occurs due to the lack of nutrients and oxygen after 7.5 hours in a batch growth system.

4. Conclusion

FTIR is an extremely rapid technique compared to conventional techniques. FTIR has uniform applicability to various bacteria and a high specificity for differentiating toxic effects at intracellular levels. Thus, it can provide clear discrimination between chemically exposed bacteria in comparison to controls. The spectral range in this method could assist in rapidly evaluating the toxicity level of different stressors, such as nanoparticles. Consequently, FTIR spectroscopy could be successfully applied to characterize time-dependent toxicity impacts of nanoparticles in bacteria and to assess the intensity of cell sensitivity toward physical or chemical treatments. FTIR

techniques in this context provide diagnostic methods for different forms of samples. Complementary techniques, such as NMR, Raman, XPS, and mass spectroscopy, can increase the information density in order to determine the intracellular composition and structures of treated and untreated cells.

Acknowledgments

This research work was supported by the National Science Foundation under the grant numbers CBET-1350789.

References

Ahimou F, Boonaert CJP, Adriaensen Y, et al (2007) XPS analysis of chemical functions at the surface of Bacillus subtilis. J Colloid Interface Sci 309:49–55. doi: 10.1016/j.jcis.2007.01.055

Al-Holy MA, Lin M, Cavinato AG, Rasco BA (2006) The use of Fourier transform infrared spectroscopy to differentiate Escherichia coli O157:H7 from other bacteria inoculated into apple juice. Food Microbiol 23:162–168. doi: 10.1016/j.fm.2005.01.017

Al-Qadiri HM, Al-Alami NI, Al-Holy MA, Rasco BA (2008a) Using Fourier Transform Infrared (FT-IR) Absorbance Spectroscopy and Multivariate Analysis To Study the Effect of Chlorine-Induced Bacterial Injury in Water. J Agric Food Chem 56:8992–8997. doi: 10.1021/jf801604p

Al-Qadiri H m., Lin M, Al-Holy M a., et al (2008b) Detection of Sublethal Thermal Injury in Salmonella enterica Serotype Typhimurium and Listeria monocytogenes

Using Fourier Transform Infrared (FT-IR) Spectroscopy (4000 to 600 cm−1). J Food Sci 73:M54–M61. doi: 10.1111/j.1750-3841.2007.00640.x

Alvarez A, Halisch J, Prieto M (2010) Changes in Fourier transform infrared spectra of Salmonella enterica serovars Typhimurium and Enteritidis after adaptation to stressful growth conditions. Int J Food Microbiol 142:97–105. doi: 10.1016/j.ijfoodmicro.2010.06.008

Ami D, Natalello A, Schultz T, et al (2009) Effects of recombinant protein misfolding and aggregation on bacterial membranes. Biochim Biophys Acta BBA - Proteins Proteomics 1794:263–269. doi: 10.1016/j.bbapap.2008.10.015

Anaya NM, Faghihzadeh F, Ganji N, et al Comparative study between chemostat and batch reactors to quantify membrane permeability changes on bacteria exposed to silver nanoparticles. Sci Total Environ. doi: 10.1016/j.scitotenv.2016.03.039

Anaya NM, Solomon F, Oyanedel-Craver V (2015) Effects of dysprosium oxide nanoparticles on Escherichia coli. Environ Sci Nano. doi: 10.1039/C5EN00074B

Arora S, Jain J, Rajwade JM, Paknikar KM (2008) Cellular responses induced by silver nanoparticles: In vitro studies. Toxicol Lett 179:93–100. doi: 10.1016/j.toxlet.2008.04.009

Beech IB, Zinkevich V, Tapper R, et al (1999) Study of the interaction of sulphate-reducing bacteria exopolymers with iron using X-ray photoelectron spectroscopy and time-of-flight secondary ionisation mass spectrometry. J Microbiol Methods 36:3–10. doi: 10.1016/S0167-7012(99)00005-6

Beekes M, Lasch P, Naumann D (2007) Analytical applications of Fourier transform-infrared (FT-IR) spectroscopy in microbiology and prion research. Vet Microbiol 123:305–319. doi: 10.1016/j.vetmic.2007.04.010

Bellamy LJ (1975) The infra-red spectra of complex molecules. Chapman and Hall London

Beney L, Mille Y, Gervais P (2004) Death of Escherichia coli during rapid and severe dehydration is related to lipid phase transition. Appl Microbiol Biotechnol 65:457–464. doi: 10.1007/s00253-004-1574-x

Boonaert CJP, Dufrene YF, Derclaye SR, Rouxhet PG (2001) Adhesion of Lactococcus lactis to model substrata: direct study of the interface. Colloids Surf B Biointerfaces 22:171–182. doi: 10.1016/S0927-7765(01)00196-5

Bruinsma GM, van der Mei HC, Busscher HJ (2001) Bacterial adhesion to surface hydrophilic and hydrophobic contact lenses. Biomaterials 22:3217–3224. doi: 10.1016/S0142-9612(01)00159-4

Burgula Y, Khali D, Kim S, et al (2006) Detection of Escherichia coli O157:H7 and Salmonella typhimurium using filtration followed by Fourier-transform infrared spectroscopy. J Food Prot 69:1777–1784.

Burgula Y, Khali D, Kim S, et al (2007) Review of Mid-Infrared Fourier Transform-Infrared Spectroscopy Applications for Bacterial Detection. J Rapid Methods Autom Microbiol 15:146–175. doi: 10.1111/j.1745-4581.2007.00078.x

Buszewski B (2015) Assignment of functional groups in Gram-positive bacteria. J Anal Bioanal Tech. doi: 10.4172/2155-9872.1000232

Cadet F, de la Guardia M (2000) Quantitative Analysis, Infrared. In: Meyers RA (ed) Encyclopedia of Analytical Chemistry. John Wiley & Sons, Ltd, Chichester, UK,

Candeloro P, Tirinato L, Malara N, et al (2011) Nanoparticle microinjection and Raman spectroscopy as tools for nanotoxicology studies. Analyst 136:4402–4408. doi: 10.1039/C1AN15313G

Carlos C, Maretto DA, Poppi RJ, et al (2011) Fourier transform infrared microspectroscopy as a bacterial source tracking tool to discriminate fecal E. coli strains. Microchem J 99:15–19. doi: 10.1016/j.microc.2011.03.002

Cegelski L (2015) Bottom-up and top-down solid-state NMR approaches for bacterial biofilm matrix composition. J Magn Reson 253:91–97. doi: 10.1016/j.jmr.2015.01.014

Chia BCS, Lam Y-H, Dyall-Smith M, et al (2000) A31P NMR study of the interaction of amphibian antimicrobial peptides with the membranes of live bacteria. Lett Pept Sci 7:151–156. doi: 10.1007/BF02443582

Choi O, Deng KK, Kim N-J, et al (2008) The inhibitory effects of silver nanoparticles, silver ions, and silver chloride colloids on microbial growth. Water Res 42:3066–3074. doi: 10.1016/j.watres.2008.02.021

Cieślik-Boczula K, Czarnik-Matusewicz B, Perevozkina M, et al (2008) ATR-IR spectroscopic study of the structural changes in the hydrophobic region of ICPAN/DPPC bilayers. J Mol Struct 878:162–168. doi: 10.1016/j.molstruc.2007.08.003

Coates J (2006) Interpretation of Infrared Spectra, A Practical Approach. In: Encyclopedia of Analytical Chemistry. John Wiley & Sons, Ltd,

Colthup N (2012) Introduction to Infrared and Raman Spectroscopy. Elsevier

Corte L, Rellini P, Roscini L, et al (2010) Development of a novel, FTIR (Fourier transform infrared spectroscopy) based, yeast bioassay for toxicity testing and stress response study. Anal Chim Acta 659:258–265. doi: 10.1016/j.aca.2009.11.035

Davis JH, Nichol CP, Weeks G, Bloom M (1979) Study of the cytoplasmic and outer membranes of Escherichia coli by deuterium magnetic resonance. Biochemistry (Mosc) 18:2103–2112. doi: 10.1021/bi00577a041

Davis R, Irudayaraj J, Reuhs BL, Mauer LJ (2010) Detection of E. coli O157:H7 from ground beef using Fourier transform infrared (FT-IR) spectroscopy and chemometrics. J Food Sci 75:M340–346. doi: 10.1111/j.1750-3841.2010.01686.x

Davis R, Mauer LJ (2010) Fourier transform infrared (FT-IR) spectroscopy: a rapid tool for detection and analysis of foodborne pathogenic bacteria. Curr Res Technol Educ Top Appl Microbiol Microb Biotechnol 2:1582–1594.

Dufrêne YF, Rouxhet PG (1996) X-ray photoelectron spectroscopy analysis of the surface composition of Azospirillum brasilense in relation to growth conditions. Colloids Surf B Biointerfaces 7:271–279. doi: 10.1016/0927-7765(96)01295-7

Dufrêne YF, van der Wal A, Norde W, Rouxhet PG (1997) X-ray photoelectron spectroscopy analysis of whole cells and isolated cell walls of gram-positive bacteria: comparison with biochemical analysis. J Bacteriol 179:1023–1028.

Eckhardt S, Brunetto PS, Gagnon J, et al (2013) Nanobio Silver: Its Interactions with Peptides and Bacteria, and Its Uses in Medicine. Chem Rev 113:4708–4754. doi: 10.1021/cr300288v

Fang J, Lyon DY, Wiesner MR, et al (2007) Effect of a Fullerene Water Suspension on Bacterial Phospholipids and Membrane Phase Behavior. Environ Sci Technol 41:2636–2642. doi: 10.1021/es062181w

Fang T-T, Li X, Wang Q-S, et al (2012) Toxicity evaluation of CdTe quantum dots with different size on Escherichia coli. Toxicol In Vitro 26:1233–1239. doi: 10.1016/j.tiv.2012.06.001

Feng QL, Wu J, Chen GQ, et al (2000) A mechanistic study of the antibacterial effect of silver ions on Escherichia coli and Staphylococcus aureus. J Biomed Mater Res 52:662–668.

Feo JC, Castro MA, Robles LC, Aller AJ (2004) Fourier-transform infrared spectroscopic study of the interactions of selenium species with living bacterial cells. Anal Bioanal Chem 378:1601–1607. doi: 10.1007/s00216-004-2494-4

Garidel P, Boese M (2007) Non-Invasive Fourier Transform infrared Microspectroscopy and Imaging Techniques: Basic Principles and Application. Mod Res Educ Top Microsc 132–143.

Gericke A, Huehnerfuss H (1995) Investigation of Z- and E-Unsaturated Fatty Acids, Fatty Acid Esters, and Fatty Alcohols at the Air/Water Interface by Infrared Spectroscopy. Langmuir 11:225–230. doi: 10.1021/la00001a039

Gopal J, Manikandan M, Hasan N, et al (2013) A comparative study on the mode of interaction of different nanoparticles during MALDI-MS of bacterial cells. J Mass Spectrom 48:119–127. doi: 10.1002/jms.3135

Graves JL, Tajkarimi M, Cunningham Q, et al (2015) Rapid evolution of silver nanoparticle resistance in Escherichia coli. Front Genet. doi: 10.3389/fgene.2015.00042

Gué Michaël, Dupont V, Dufour A, Sire O (2001) Bacterial Swarming: A Biochemical Time-Resolved FTIR−ATR Study of Proteus mirabilis Swarm-Cell Differentiation. Biochemistry (Mosc) 40:11938–11945. doi: 10.1021/bi010434m

Gurbanov R, Simsek Ozek N, Gozen AG, Severcan F (2015) Quick Discrimination of Heavy Metal Resistant Bacterial Populations Using Infrared Spectroscopy Coupled with Chemometrics. Anal Chem 87:9653–9661. doi: 10.1021/acs.analchem.5b01659

Hamadi F, Latrache H, Zahir H, et al (2008) The relation between Escherichia coli surface functional groups' composition and their physicochemical properties. Braz J Microbiol Publ Braz Soc Microbiol 39:10–15. doi: 10.1590/S1517-83822008000100003

Helm D, Labischinski H, Schallehn G, Naumann D (1991) Classification and identification of bacteria by Fourier-transform infrared spectroscopy. J Gen Microbiol 137:69–79. doi: 10.1099/00221287-137-1-69

Holman H-YN, Miles R, Hao Z, et al (2009) Real-Time Chemical Imaging of Bacterial Activity in Biofilms Using Open-Channel Microfluidics and Synchrotron FTIR Spectromicroscopy. Anal Chem 81:8564–8570. doi: 10.1021/ac9015424

Hu C, Guo J, Qu J, Hu X (2007) Photocatalytic Degradation of Pathogenic Bacteria with AgI/TiO2 under Visible Light Irradiation. Langmuir 23:4982–4987. doi: 10.1021/la063626x

Hu X, Qiu Z, Wang Y, et al (2009) Effect of ultra-strong static magnetic field on bacteria: Application of Fourier-transform infrared spectroscopy combined with cluster analysis and deconvolution. Bioelectromagnetics 30:500–507. doi: 10.1002/bem.20506

Jiang W, Saxena A, Song B, et al (2004) Elucidation of functional groups on gram-positive and gram-negative bacterial surfaces using infrared spectroscopy. Langmuir ACS J Surf Colloids 20:11433–11442. doi: 10.1021/la049043+

Jiang W, Yang K, Vachet RW, Xing B (2010) Interaction between Oxide Nanoparticles and Biomolecules of the Bacterial Cell Envelope As Examined by Infrared Spectroscopy. Langmuir 26:18071–18077. doi: 10.1021/la103738e

Jr TP (1995) All About Albumin: Biochemistry, Genetics, and Medical Applications. Academic Press

Kacurakova M, Mathlouthi M (1996) FTIR and laser-Raman spectra of oligosaccharides in water: characterization of the glycosidic bond. Carbohydr Res 284:145–157. doi: 10.1016/0008-6215(95)00412-2

Karatzas KAG, Bennik MHJ (2002) Characterization of a Listeria monocytogenes Scott A Isolate with High Tolerance towards High Hydrostatic Pressure. Appl Environ Microbiol 68:3183–3189. doi: 10.1128/AEM.68.7.3183-3189.2002

Kenner BA, Riddle JW, Rockwood SW, Bordner RH (1958) BACTERIAL IDENTIFICATION BY INFRARED SPECTROPHOTOMETRY II. J Bacteriol 75:16–20.

Kiwi J, Nadtochenko V (2005) Evidence for the Mechanism of Photocatalytic Degradation of the Bacterial Wall Membrane at the TiO_2 Interface by ATR-FTIR and Laser Kinetic Spectroscopy. Langmuir 21:4631–4641. doi: 10.1021/la046983l

Kollias N, Stamatas G (2002) Optical Non-Invasive Approaches to Diagnosis of Skin Diseases. J Investig Dermatol Symp Proc 7:64–75. doi: 10.1046/j.1523-1747.2002.19635.x

Lamprecht C, Gierlinger N, Heister E, et al (2012) Mapping the intracellular distribution of carbon nanotubes after targeted delivery to carcinoma cells using confocal Raman imaging as a label-free technique. J Phys Condens Matter 24:164206. doi: 10.1088/0953-8984/24/16/164206

Larkin P (2011) Infrared and Raman Spectroscopy; Principles and Spectral Interpretation. Elsevier

Lasch P, Naumann D (2000) Infrared spectroscopy in microbiology.

Lay JO (2001) MALDI-TOF mass spectrometry of bacteria*. Mass Spectrom Rev 20:172–194. doi: 10.1002/mas.10003

Leone L, Loring J, Sjöberg S, et al (2006) Surface characterization of the Gram-positive bacteria Bacillus subtilis-an XPS study. Surf Interface Anal 38:202–205. doi: 10.1002/sia.2184

Levine S, Stevenson HJR, Chambers LA, Kenner BA (1953) INFRARED SPECTROPHOTOMETRY OF ENTERIC BACTERIA. J Bacteriol 65:10–15.

Lewis RN, McElhaney RN, Monck MA, Cullis PR (1994) Studies of highly asymmetric mixed-chain diacyl phosphatidylcholines that form mixed-interdigitated gel phases: Fourier transform infrared and 2H NMR spectroscopic studies of hydrocarbon chain conformation and orientational order in the liquid-crystalline state. Biophys J 67:197–207. doi: 10.1016/S0006-3495(94)80470-9

Liau SY, Read DC, Pugh WJ, et al (1997) Interaction of silver nitrate with readily identifiable groups: relationship to the antibacterial action of silver ions. Lett Appl Microbiol 25:279–283.

Li J, Strong R, Trevisan J, et al (2013) Dose-Related Alterations of Carbon Nanoparticles in Mammalian Cells Detected Using Biospectroscopy: Potential for Real-World Effects. Environ Sci Technol 47:10005–10011. doi: 10.1021/es4017848

Li J, Ying G-G, Jones KC, Martin FL (2015) Real-world carbon nanoparticle exposures induce brain and gonadal alterations in zebrafish (Danio rerio) as determined by biospectroscopy techniques. The Analyst 140:2687–2695. doi: 10.1039/C4AN02227K

Lin M, Al-Holy M, Al-Qadiri H, et al (2004) Discrimination of Intact and Injured Listeria monocytogenes by Fourier Transform Infrared Spectroscopy and Principal Component Analysis. J Agric Food Chem 52:5769–5772. doi: 10.1021/jf049354q

Liu Z, Yang S, Bai Y, et al (2011) The alteration of cell membrane of sulfate reducing bacteria in the presence of Mn(II) and Cd(II). Miner Eng 24:839–844. doi: 10.1016/j.mineng.2011.03.005

Lorin–Latxague C, Melin A-M (2005) Radical induced damage of Micrococcus luteus bacteria monitored using FT–IR spectroscopy. J Spectrosc 19:17–26. doi: 10.1155/2005/386404

Losasso C, Belluco S, Cibin V, et al (2014) Antibacterial activity of silver nanoparticles: sensitivity of different Salmonella serovars. Front Microbiol. doi: 10.3389/fmicb.2014.00227

Maquelin K, Kirschner C, Choo-Smith L-P, et al (2002) Identification of medically relevant microorganisms by vibrational spectroscopy. J Microbiol Methods 51:255–271. doi: 10.1016/S0167-7012(02)00127-6

Mariey L, Signolle JP, Amiel C, Travert J (2001) Discrimination, classification, identification of microorganisms using FTIR spectroscopy and chemometrics. Vib Spectrosc 26:151–159. doi: 10.1016/S0924-2031(01)00113-8

Mauer LJ, Reuhs BL, Voeller JG (2008) Mid-Infrared Sensors for The Rapid Analysis of Select Microbial Food Borne Pathogens. In: Wiley Handbook of Science and Technology for Homeland Security. John Wiley & Sons, Inc.,

Meier RJ (2005) Vibrational spectroscopy: a “vanishing” discipline? Chem Soc Rev 34:743. doi: 10.1039/b503880d

Mille Y, Beney L, Gervais P (2002) Viability of Escherichia coli after combined osmotic and thermal treatment: a plasma membrane implication. Biochim Biophys Acta BBA - Biomembr 1567:41–48. doi: 10.1016/S0005-2736(02)00565-5

M. Lopez Goerne, T (2011) Study of Bacterial Sensitivity to Ag-TiO2 Nanoparticles. J Nanomedicine Nanotechnol. doi: 10.4172/2157-7439.S5-003

Moen B, Janbu AO, Langsrud S, et al (2009) Global responses of Escherichia coli to adverse conditions determined by microarrays and FT-IR spectroscopy. Can J Microbiol 55:714–728. doi: 10.1139/w09-016

Moen B, Oust A, Langsrud Ø, et al (2005) Explorative multifactor approach for investigating global survival mechanisms of Campylobacter jejuni under environmental conditions. Appl Environ Microbiol 71:2086–2094. doi: 10.1128/AEM.71.4.2086-2094.2005

Mossoba MM, Al-Khaldi SF, Jacobson A, et al (2003) Application of a disposable transparent filtration membrane to the infrared spectroscopic discrimination among bacterial species. J Microbiol Methods 55:311–314. doi: 10.1016/S0167-7012(03)00114-3

Mouwen DJM, Weijtens MJBM, Capita R, et al (2005) Discrimination of Enterobacterial Repetitive Intergenic Consensus PCR Types of Campylobacter coli and Campylobacter jejuni by Fourier Transform Infrared Spectroscopy. Appl Environ Microbiol 71:4318–4324. doi: 10.1128/AEM.71.8.4318-4324.2005

Mura S, Greppi G, Marongiu ML, et al (2012) FTIR nanobiosensors for *Escherichia coli* detection. Beilstein J Nanotechnol 3:485–492. doi: 10.3762/bjnano.3.55

Nadtochenko VA, Rincon AG, Stanca SE, Kiwi J (2005) Dynamics of E. coli membrane cell peroxidation during TiO2 photocatalysis studied by ATR-FTIR spectroscopy and AFM microscopy. J Photochem Photobiol Chem 169:131–137. doi: 10.1016/j.jphotochem.2004.06.011

Naumann D (2006) Infrared Spectroscopy in Microbiology. In: Encyclopedia of Analytical Chemistry. John Wiley & Sons, Ltd,

Naumann D, Helm D, Labischinski H (1991) Microbiological characterizations by FT-IR spectroscopy. Nature 351:81–82. doi: 10.1038/351081a0

Naumann D, Schultz C, Sabisch A, et al (1989) New insights into the phase behaviour of a complex anionic amphiphile: architecture and dynamics of bacterial deep rough lipopolysaccharide membranes as seen by FTIR, X-ray, and molecular modelling techniques. J Mol Struct 214:213–246. doi: 10.1016/0022-2860(89)80015-8

Nelson BC, Petersen EJ, Marquis BJ, et al (2013) NIST gold nanoparticle reference materials do not induce oxidative DNA damage. Nanotoxicology 7:21–29. doi: 10.3109/17435390.2011.626537

Nydegger MW, Rock W, Cheatum CM (2011) 2D IR spectroscopy of the C-D stretching vibration of the deuterated formic acid dimer. Phys Chem Chem Phys PCCP 13:6098–6104. doi: 10.1039/c0cp01087a

Ojeda JJ, Romero-Gonzalez ME, Bachmann RT, et al (2008) Characterization of the cell surface and cell wall chemistry of drinking water bacteria by combining XPS, FTIR spectroscopy, modeling, and potentiometric titrations. Langmuir ACS J Surf Colloids 24:4032–4040. doi: 10.1021/la702284b

Omoike A, Chorover J (2004) Spectroscopic study of extracellular polymeric substances from Bacillus subtilis: aqueous chemistry and adsorption effects. Biomacromolecules 5:1219–1230. doi: 10.1021/bm034461z

Oren Z, Ramesh J, Avrahami D, et al (2002) Structures and mode of membrane interaction of a short αhelical lytic peptide and its diastereomer determined by NMR, FTIR, and fluorescence spectroscopy. Eur J Biochem 269:3869–3880. doi: 10.1046/j.1432-1033.2002.03080.x

Papadimitriou K, Boutou E, Zoumpopoulou G, et al (2008) RNA arbitrarily primed PCR and fourier transform infrared spectroscopy reveal plasticity in the acid tolerance response of Streptococcus macedonicus. Appl Environ Microbiol 74:6068–6076. doi: 10.1128/AEM.00315-08

Parker FS (1983) Applications of Infrared, Raman, and Resonance Raman Spectroscopy in Biochemistry. Springer Science & Business Media

Park H-J, Kim JY, Kim J, et al (2009) Silver-ion-mediated reactive oxygen species generation affecting bactericidal activity. Water Res 43:1027–1032. doi: 10.1016/j.watres.2008.12.002

Perkins DL, Lovell CR, Bronk BV, et al (2004) Effects of Autoclaving on Bacterial Endospores Studied by Fourier Transform Infrared Microspectroscopy. Appl Spectrosc 58:749–753.

Persson P, Nilsson N, Sjöberg S (1996) Structure and Bonding of Orthophosphate Ions at the Iron Oxide–Aqueous Interface. J Colloid Interface Sci 177:263–275. doi: 10.1006/jcis.1996.0030

Picquart M, Haro-Poniatowski E, Morhange JF, et al (2000) Low frequency vibrations and structural characterization of a murine IgG2a monoclonal antibody studied by

Raman and IR spectroscopies. Biopolymers 53:342–349. doi: 10.1002/(SICI)1097-0282(20000405)53:4<342::AID-BIP6>3.0.CO;2-M

Pius J, Morrow MR, Booth V (2012) 2H Solid-State Nuclear Magnetic Resonance Investigation of Whole Escherichia coli Interacting with Antimicrobial Peptide MSI-78. Biochemistry (Mosc) 51:118–125. doi: 10.1021/bi201569t

Podstawka-Proniewicz E, Piergies N, Skołuba D, et al (2011) Vibrational characterization of L-leucine phosphonate analogues: FT-IR, FT-Raman, and SERS spectroscopy studies and DFT calculations. J Phys Chem A 115:11067–11078. doi: 10.1021/jp207101m

Pradier CM, Rubio C, Poleunis C, et al (2005) Surface Characterization of Three Marine Bacterial Strains by Fourier Transform IR, X-ray Photoelectron Spectroscopy, and Time-of-Flight Secondary-Ion Mass Spectrometry, Correlation with Adhesion on Stainless Steel Surfaces. J Phys Chem B 109:9540–9549. doi: 10.1021/jp044705p

Ramstedt M, Nakao R, Wai SN, et al (2011) Monitoring Surface Chemical Changes in the Bacterial Cell Wall. J Biol Chem 286:12389–12396. doi: 10.1074/jbc.M110.209536

Reckel S, Löhr F, Dötsch V (2005) In-Cell NMR Spectroscopy. ChemBioChem 6:1601–1606. doi: 10.1002/cbic.200500076

Reddy KM, Feris K, Bell J, et al (2007) Selective toxicity of zinc oxide nanoparticles to prokaryotic and eukaryotic systems. Appl Phys Lett 90:213902–1–213902–3. doi: 10.1063/1.2742324

Riddle JW, Kabler PW, Kenner BA, et al (1956) Bacterial identification by infrared spectrophotometry. J Bacteriol 72:593–603.

Riding MJ, Martin FL, Trevisan J, et al (2012) Concentration-dependent effects of carbon nanoparticles in gram-negative bacteria determined by infrared spectroscopy with multivariate analysis. Environ Pollut 163:226–234. doi: 10.1016/j.envpol.2011.12.027

Rizzello L, Pompa PP (2014) Nanosilver-based antibacterial drugs and devices: Mechanisms, methodological drawbacks, and guidelines. Chem Soc Rev 43:1501–1518. doi: 10.1039/C3CS60218D

R. KINDER C. ZIEGLER, WESSELS JM (1997) gamma-Irradiation and UV-C light-induced lipid peroxidation: a Fourier transform-infrared absorption spectroscopic study. Int J Radiat Biol 71:561–571. doi: 10.1080/095530097143897

Rodriguez-Saona LE, Khambaty FM, Fry FS, et al (2004) Detection and Identification of Bacteria in a Juice Matrix with Fourier Transform–Near Infrared Spectroscopy and Multivariate Analysis. J Food Prot 67:2555–2559.

Romaniuk JAH, Cegelski L (2015) Bacterial cell wall composition and the influence of antibiotics by cell-wall and whole-cell NMR. Phil Trans R Soc B 370:20150024. doi: 10.1098/rstb.2015.0024

Rouxhet PG, Mozes N, Dengis PB, et al (1994) Application of X-ray photoelectron spectroscopy to microorganisms. Colloids Surf B Biointerfaces 2:347–369. doi: 10.1016/0927-7765(94)80049-9

Schanda P, Triboulet S, Laguri C, et al (2014) Atomic Model of a Cell-Wall Cross-Linking Enzyme in Complex with an Intact Bacterial Peptidoglycan. J Am Chem Soc 136:17852–17860. doi: 10.1021/ja5105987

Schifman LA, Kasaraneni VK, Sullivan RK, et al (2015) New Antimicrobially Amended Media for Improved Nonpoint Source Bacterial Pollution Treatment. Environ Sci Technol 49:14383–14391. doi: 10.1021/acs.est.5b03782

Schleicher E, Heßling B, Illarionova V, et al (2005) Light-induced reactions of Escherichia coli DNA photolyase monitored by Fourier transform infrared spectroscopy. FEBS J 272:1855–1866. doi: 10.1111/j.1742-4658.2005.04617.x

Serber Z, Dötsch V (2001) In-Cell NMR Spectroscopy. Biochemistry (Mosc) 40:14317–14323. doi: 10.1021/bi011751w

Shah NB, Dong J, Bischof JC (2011) Cellular Uptake and Nanoscale Localization of Gold Nanoparticles in Cancer Using Label-Free Confocal Raman Microscopy. Mol Pharm 8:176–184. doi: 10.1021/mp1002587

Shah N, Sattar A, Benanti M, et al (2006) Magnetic resonance spectroscopy as an imaging tool for cancer: a review of the literature. J Am Osteopath Assoc 106:23–27.

Sivakesava S, Irudayaraj J, Debroy C (2004) Differentiation of microorganisms by FTIR-AIR and NIR spectroscopy. Trans ASAE 47:951–957.

Sprenger D, Anderson O (1991) Deconvolution of XPS spectra. Fresenius J Anal Chem 341:116–120. doi: 10.1007/BF00322120

Tardy-Laporte C, Arnold AA, Genard B, et al (2013) A 2H solid-state NMR study of the effect of antimicrobial agents on intact Escherichia coli without mutating. Biochim Biophys Acta BBA - Biomembr 1828:614–622. doi: 10.1016/j.bbamem.2012.09.011

Thi NAN, Naumann D (2006) Investigating the heterogeneity of cell growth in microbial colonies by FTIR microspectroscopy. Anal Bioanal Chem 387:1769–1777. doi: 10.1007/s00216-006-0829-z

Tyler BJ (1997) XPS and SIMS studies of surfaces important in biofilm formation. Three case studies. Ann N Y Acad Sci 831:114–126.

van der Mei HC, de Vries J, Busscher HJ (2000) X-ray photoelectron spectroscopy for the study of microbial cell surfaces. Surf Sci Rep 39:1–24. doi: 10.1016/S0167-5729(00)00003-0

Whittaker P, Mossoba MM, Al-Khaldi S, et al (2003) Identification of foodborne bacteria by infrared spectroscopy using cellular fatty acid methyl esters. J Microbiol Methods 55:709–716. doi: 10.1016/j.mimet.2003.07.005

Wigginton NS, Titta A de, Piccapietra F, et al (2010) Binding of Silver Nanoparticles to Bacterial Proteins Depends on Surface Modifications and Inhibits Enzymatic Activity. Environ Sci Technol 44:2163–2168. doi: 10.1021/es903187s

Winder CL, Goodacre R (2004) Comparison of diffuse-reflectance absorbance and attenuated total reflectance FT-IR for the discrimination of bacteria. The Analyst 129:1118–1122. doi: 10.1039/b408169b

Yan L, Marzolin C, Terfort A, Whitesides GM (1997) Formation and Reaction of Interchain Carboxylic Anhydride Groups on Self-Assembled Monolayers on Gold. Langmuir 13:6704–6712. doi: 10.1021/la970762g

Yuan W, Jiang G, Che J, et al (2008) Deposition of Silver Nanoparticles on Multiwalled Carbon Nanotubes Grafted with Hyperbranched Poly(amidoamine) and Their Antimicrobial Effects. J Phys Chem C 112:18754–18759. doi: 10.1021/jp807133j

Yu C, Irudayaraj J (2005) Spectroscopic characterization of microorganisms by Fourier transform infrared microspectroscopy. Biopolymers 77:368–377. doi: 10.1002/bip.20247

Zeroual W, Choisy C, Doglia SM, et al (1994) Monitoring of bacterial growth and structural analysis as probed by FT-IR spectroscopy. Biochim Biophys Acta BBA - Mol Cell Res 1222:171–178. doi: 10.1016/0167-4889(94)90166-X

Zhang H (2013) Application of silver nanoparticles in drinking water purification. University of Rhode Island

Zhang H, Oyanedel-Craver V (2013) Comparison of the bacterial removal performance of silver nanoparticles and a polymer based quaternary amine functiaonalized silsesquioxane coated point-of-use ceramic water filters. J Hazard Mater 260:272–277. doi: 10.1016/j.jhazmat.2013.05.025

XW, Wang W, PL, et al (2011) Photocatalytic degradation of E.coli membrane cell in the presence of ZnO nanowires. J Wuhan Univ Technol-Mater Sci Ed 26:222–225. doi: 10.1007/s11595-011-0201-9

FT-IR Library: an essential reference for research. In: Sigma-Aldrich. http://www.sigmaaldrich.com/labware/learning-center/spectral-viewer/ft-ir-library.html. Accessed 24 Dec 2015a

Infrared Spectral Interpretation: A Systematic Approach. In: CRC Press. https://www.crcpress.com/Infrared-Spectral-Interpretation-A-Systematic-Approach/Smith/9780849324635. Accessed 13 Dec 2015b

MANUSCRIPT–II: KINETIC, METABOLIC AND MACROMOLECULAR RESPONSE OF BACTERIA TO CHRONIC NANOPARTICLE EXPOSURE IN CONTINUOUS CULTURE

In review at the Environmental Science-Nano Journal

F. Faghihzadeh [a], N. M. Anaya [a], C. Astudillo-Castro [b], and V. Oyanedel-Craver [a]*

[a] Department of Civil and Environmental Engineering, Bliss hall 203, University of Rhode Island, Kingston, RI, 02881, USA. E-mail: Faghihzadeh@uri.edu; nelson_anaya@my.uri.edu; craver@uri.edu. Phone: (401)-874-2784. Fax: (401)-874-2786.

[b] School of Food Engineering, Pontificia Universidad Católica de Valparaíso, 716 Waddington, Playa Ancha, Valparaiso 2360100, Chile. E-mail: carolina.astudillo@pucv.cl

* Corresponding author: Vinka Oyanedel Craver

E-Mail: craver@uri.edu

Phone: (401) 874 2784,

Fax: (401) 874 2786

Abstract

Nanoparticles with antimicrobial properties are used in thousands of nano-enabled consumer products. Therefore, it is important to understand the response mechanisms of bacteria that are exposed to these nanoparticles at different conditions. Moreover, it is necessary to evaluate possible microbial adaptation mechanisms. In our study, *Escherichia coli* K-12 MG1655 (*E. coli*) were grown continuously in bioreactors at two specific growth rates (0.1 h^{-1} and 0.2 h^{-1}) and then exposed to chronic concentrations of casein-coated silver nanoparticles (AgNPs) [1 mg/L] for about 180 generations. After initiating the injection of AgNPs, the results showed a change in growth kinetic parameters between non-exposed and exposed systems. Maximum yield (Y_{max}) decreased by 33%, while the maintenance coefficient (m_s) increased by 52%. This was evidence indicating the versatility of the culture to growth in the exposed conditions and even the ability to achieve a new stationary state. However, the adaptation was achieved at a metabolic cost. Comparing the concentration and composition of extra-cellular substances (ES) that were produced showed differences between the non-exposed and exposed conditions, and also between the exposed systems in the two growth conditions. In the AgNPs-exposed bioreactor (EB) growing at 0.1 h^{-1}, AgNPs-ES complexes showed that the ratio of the area representing β-sheets to the area representing α-helix proteins was higher than 2.4, which implies the formation of a protein corona, while at an exposed growth rate of 0.2 h^{-1} this ratio was < 1, indicating no protein corona. Transcriptomic results showed gene regulation in response to AgNPs exposure as a function of the specific growth rate. Batch exposure tests using the resultant cultures for each condition showed a lower inhibitory effect

for the AgNPs on EB at 0.1 h^{-1} than on control bacteria (CB) at 0.1 h^{-1} in terms of membrane permeation and reactive oxygen species generation. Overall, our study showed that culture growth conditions significantly affects bacterial response to nanoparticle exposure. Therefore, these growth parameters should be determined and reported when performing toxicological tests.

1. Introduction

Antimicrobial nanoparticles are used to inhibit and deactivate unwanted microorganisms,[1–3] however, bacteria stress response mechanisms can hinder the efficacy of these nanoparticles.

The impact of nanoparticles on bacteria activity and growth depends on several parameters, including the physicochemical properties of the bacteria core and shell, bulk composition, as well as the physicochemical and physiological properties of the microorganisms.[4] During bacterial growth, bulk composition changes due to the consumption and production of compounds by the bacteria. Therefore, the physiochemical characteristics of the surfaces of the nanoparticles can change through ligand capping of the organic molecules, such as thru extra-cellular substances (ES).[5] ES consist mainly of polysaccharides, proteins, nucleic acids, and lipids.[6,7] Previous studies have shown that the concentration and composition of ES changes with variation in the growth rates of microbial cultures.[7,8] Therefore, the interactions with nanoparticles may also change nanoparticle surface properties. To the best of our knowledge, this has not been previously assessed.

Studies of the interaction of AgNPs with bacteria are usually conducted in batch and/or continuous bioreactors.[1,2,4] In batch reactors, the growth rate of the bacteria culture changes over time due to the uptake of the substrate and the release of metabolic products. Additionally, there are four distinct growth phases that can be distinguished in batch cultures: lag, exponential or log, stationary, and death. Each of these phases is associated with both bulk and physiological bacterial changes.

Therefore, it can be inferred that the physicochemical properties of the nanoparticles will also likely change throughout the experimental period.[9]

Continuous reactors can be used to overcome these limitations. These reactors can achieve steady-state conditions where the concentration of the growth-controlling substrate and density of the culture do not change significantly with time.[10] Continuous cultures have been used extensively to study bacteria stress response and to investigate the development of antibiotic resistance.[11–13] In a previous study, we compared bacteria exposed to pulses of AgNPs using continuous and batch reactors, and our results showed that in terms of membrane permeability, there were marked differences between both conditions.[1] Numerous studies have reported the effects of AgNPs in terms of multiple parameters related to cell viability.[14,15] However, to the best of our knowledge, changes in the physicochemical properties of the nanoparticles at different continuous culture conditions have not been reported.

Additionally, most studies have focused on the antimicrobial effects of nanoparticles, but have not considered that in nature, microorganisms grow in

the presence of inhibitors. Therefore, in addition to nutrient uptake, growth may be controlled by the presence of anthropogenic inhibitors, such as nanoparticles. Therefore assessing the impact of nanoparticles on kinetic parameters that commonly occur in the ecological context is extremely important.[16–18]

The main objective of this study was to elucidate the impact of bacterial growth conditions and their response to chronic exposure to silver nanoparticles. We used continuous bioreactors to determine the inhibitory effect of nanoparticles in terms of kinetic parameters, nanoparticle-ES interactions, and transcriptomic analysis. Additionally, culture samples from the effluent of the exposed bioreactor (EB) and control (CB) bioreactors were re-cultured in batch mode, and then acutely exposed to AgNPs in order to compare membrane permeation, respiration activity, and reactive oxygen species (ROS) generation responses.

2. Material and Methods

2.1. Materials

A non-pathogenic strain of *Escherichia coli K-12 strain MG1655* (ATCC 700926) (*E. coli)* was selected for this study. *E. coli* is a Gram-negative bacterium that has been extensively used in nano-toxicological studies.[2,19] The reagents used to prepare the M9 minimal growth media for the bacteria [20] included: M9 minimal salts, glucose solution (BioUltra, ~20% in DI water), calcium chloride, thiamine hydrochloride and magnesium sulfate heptahydrate; and a phosphate buffer solution (PBS) containing monobasic potassium phosphate, dibasic potassium phosphate and ethylenediaminetetraacetic acid. A glucose (HK) assay kit (GAHK201KT) was purchased from Sigma Aldrich and used as received. SYTO 9 and propidium iodide

for cell membrane permeation were purchased from Invitrogen. Standard casein-coated AgNPs were obtained from Argenol Laboratories (Spain).

ROS was measured with a Dichlorofluorescin diacetate (DCFDA) Cellular ROS Detection Assay Kit from Abcam (ab113851). A Synergy TM MX microplate reader (BIOTEK, VT) was used for the batch exposure experiment.

2.2. Methods

2.2.1. Bacteria culture. In this study, we used a slightly modified version of the multiplex bioreactor system from our previous study[1] (Figure S1 in the ESI). The vessels were fed with sterile M9 minimal medium adjusted to pH 7.2 and air (airflow of 1.5 L/min). A peristaltic pump provided a flow rate of 0.1 mL/min to achieve a growth rate of 0.1 h^{-1} in one run, while 0.14 mL/min was used to achieve the 0.2 h^{-1} condition in the second run. Each run consisted of four bioreactors inoculated with 300 µl of *E. coli* inoculum (optical density at 600 nm = 1.8) and two bioreactors as blanks with only M9 minimal media. After reaching steady state in terms of bacteria optical density (OD), the four bioreactors were inoculated with *E. coli*, and two bioreactors were injected continuously with AgNPs using syringe pumps (model 100 from Kd-Scientific) (exposed bioreactors, EB), while the other two bioreactors were fed with only M9 medium as controls (CB). Subsequently, all of the bioreactors were operated for at least 32 hours. Samples were taken from each reactor every 4 hours, centrifuged and the supernatant was stored at -20 °C to extract ES and to determine glucose concentration.[21] OD600 of the resuspended pellet in 10%

PBS was measured to determine bacteria concentration using a UV Vis-spectrophotometer. The resuspended pellets from all bioreactors were stored in sterile glycerol at -20°C and used for the regrowth and toxicity analysis described in Section 2.5.

2.2.2. Kinetic parameter calculations. The μ_{max} of *E. coli* and washout dilution rate value were determined using a methodology found in the literature[22,23] (Details in ESI). μ_{max} was 0.21 h^{-1}, while the wash out dilution rate was 0.3 h^{-1} (Figure S2 in the ESI). The operational conditions in terms of specific growth rate selected for this study were to 0.1 h^{-1} and 0.2 h^{-1}.

Biomass concentration was followed by measuring OD600 according to previously published protocols.[47] Additionally, dry biomass weight was obtained for all bioreactors and normalized based on the internal volume of the continuous bioreactor vessels.

Glucose concentration (*S*) in the bioreactors was determined thru a glucose (HK) assay reagent[25] following manufacturer instructions.

The Monod equation was used to determine the saturation constant (K_s), yield coefficient ($Y_{x/s}$), maximum yield (Y_{max}), and maintenance coefficient (m_s) in the bioreactors at steady state conditions.[26] The K_s for glucose was determined using Equation 1 from continuous bioreactor theory.[23, 26]

$$K_s = S\left(\frac{\mu_{max}}{\mu} - 1\right) \qquad \text{Equation 1}$$

K_s is the substrate saturation constant (mmol/L), S is the outlet substrate concentration (mM), μ is specific growth rate (h^{-1}), and μ_{max} is maximum specific growth rate (h^{-1}).

$Y_{x/s}$ was determined by dividing biomass concentration (normalized mg dry weight cell) per mmol consumed substrate.[24,27] Furthermore, Y_{max} and m_s were obtained from the regression parameters of Equation 2.[27]

$$\frac{1}{Y_{x/s}} = \frac{1}{Y_{max}} + \frac{m_s}{\mu} \qquad \text{Equation 2}$$

2.3. Nanoparticles-EPS interaction analysis

2.3.1. Nanoparticle Characterization. AgNPs were continuously injected into each bioreactor to achieve a concentration of 1 mg/L inside the exposed bioreactors. (Figure S4 and details provided in ESI).

The nanoparticle hydrodynamic diameter size distribution and zeta potential (ζ) of the nano-suspensions were determined by using dynamic light scattering (DLS) using a Zetasizer Nano (Malvern, ZEN 3600). Inductively-coupled plasma spectroscopy (ICP-OES optima 3100, Perkin Elmer) and inductively coupled plasma mass spectrometry (iCAP Q ICP-MS) were used to measure the concentrations of AgNPs and silver ions (Ag^+). The ionic release from AgNPs at each condition was quantified as Anaya *et al.*,[1] Ag ions released was quantified for the conditions: AgNPs with ES (from continuous bioreactors), AgNPs with M9 minimal medium, and AgNPs with distilled water (control). Digestion in 2% nitric acid was required for all samples before analysis.

2.3.2. Cryogenic transmission electron microscopy. Nanoparticle suspensions were characterized by transmission electron microscopy (cryo-TEM). Also, the interaction between AgNPs-ES and formation of the protein corona on the nanoparticles surface were monitored by cryo-TEM during different times of exposure (0 h, 8 h, and 32 h). Sample for cryo-TEM were verified using a Vitrobot (FEI Company).[28] Quantifoil grids with 2 mm holey-carbon on 200 square mesh copper (Electron Microscopy Sciences, Hat-field, PA) were used for specimens preparation. Imaging was carried out by using a JEOL JEM-2100F TEM (Peabody, MA) in a cooled stage (model 915, Gatan Inc., Pleasanton, CA). ImageJ software was used for image analysis.

2.3.3. EPS quantification and characterization. Initially, ES was separated from the bacterial culture suspension of continuous bioreactor using a previously described methodology by Seo and Bailey.[46]

Dried ES were characterized using ATR-FTIR (Nicolet iS50 FTIR, Thermo Scientific). Spectra of the samples were the result of 256 scans with a resolution of 4 cm^{-1} in the 1800-900 cm^{-1} spectral range (Omnic software, Thermo Scientific) and processed using MATLAB (MathWorks Software). Hierarchical cluster analysis (HCA) was applied to discriminate the compositional differences between the ATR-FTIR spectra of ES from exposed and control bioreactors at the different conditions tested.[29] For HCA, a data set was collected from the pair-wise similarity coefficients of all spectra as a matrix of correlation coefficients, which contains total number of spectra (N entries).[30] Between two spectra, each correlation coefficient can range from 0.0 for completely different spectra to 1.0 for identical spectra. The similar spectra

were obtained by the recalculation of correlation matrix. Then, the identical spectra were merged into a new object and the merging process repeated until all spectra are combined into a small number of clusters.

Thermogravimetric analysis (TGA) of dried ES was performed in a thermogravimetric apparatus with N_2 atmosphere by using a TA instrument Q500 TGA following previously reported methodology.[31] Data were also obtained from the first derivative of the TGA line. Raw data of TGA were smoothed by a moving average and the Gaussian fit to first derivative of smooth data was found by MATLAB software.

Formation of protein corona on the AgNPs surface was determined as well by using the ATR-FTIR.[32] It was assumed that the observed peak is the summation of two Gaussian functions representing β sheet and α helix structure,[3,32] coefficients for these functions have been determined by a parametric fitting of the data by MATLAB on the observed peak in range of 1800-1550 cm^{-1}. After subtraction of the protein from the casein layer of AgNPs, the ratio between areas under β sheet to α helix structure of proteins was altered after corona formation.[35] The ES without AgNPs was exposed to different concentration of AgNPs to validate the protein corona formation onto AgNPs surface.

2.4. Reverse-Transcription Quantitative Polymerase Chain Reaction (RT-qPCR)

Reverse transcript (RT)-qPCR is a valuable tool widely used for analysis of gene expression.[33–37] Previously, dominant genes have been identified to response AgNPs inhibitory effects including outer membrane porin (*ompF*), copper efflux

oxidase (*cueO*), copper/silver efflux system (*cusA*), and copper transporter (*copA*) genes.[4,19] These genes are responsible for the following metabolic pathways; outer membrane porin F, oxidizes model substrate dimethoxyphenol, silver and copper efflux of membrane transporter, and silver-translocating P-type ATPase efflux pump.[19] Also, a previous report showed that at the transcriptional level, fatty acid synthesis inhibited by the AgNPs inhibitory effects[35], hence, the expression of beta hydroxydecanoyl thioester dehydrase (*FabR)* gene that regulated *E. coli* fatty acid synthesis was also considered.[38] In addition, the expression of glucose 6-phosphate dehydrogenase (*zwf*) and capsular polysaccharide (*cpsB*) regulons impact on the respiration metabolic pathway [33] as well as colanic acid and capsular polysaccharide biosynthesis[39], respectively, were determined.

For real-time quantitative polymerase chain reaction (RT-qPCR) determination, samples from the effluent of the bioreactor were collected in tubes containing RNAlater solution (Ambion Inc. Austin, TX). Total RNA extraction was performed using PureLink™ RNA Mini Kit (Ambion Inc. Austin, TX). Total RNA concentration was quantified by NanoDrop. In order to obtain pure RNA and reduce the genomic DNA contamination, we treated the extracted RNA with DNase free from Maxima First Strand cDNA Synthesis kit (Thermo Fisher Scientific, Waltham, MA). Then first strand cDNA was synthesized by using DNase free RNA and random primers according to the protocol of Maxima First Strand cDNA Synthesis kit (Thermo Fisher Scientific, Waltham, MA). Running the reactions without cDNA were produced negative controls. The National Center for Biotechnology Information (NCBI) was used to determine the gene sequences and designing gene-specific real-

time primers was performed by OligoAnalizer 3.1 tool available from the Integrated DNA Technologies website (https://www.idtdna.com/calc/analyzer) (details in the ESI). Also, primer sequences are listed in Table S4 of the ESI. The specificity of designed primers was checked in NCBI to be sure that their binding sites are unique in the genome.

Quantification of cDNA was performed by using SYBR Green PCR Master Mix (Applied Biosystems). Two replicates per treatment were considered for RT-qPCRs using the cDNA. Comparative Cycle threshold (C_T) method ($\Delta\Delta C_T$) was used to perform the calculations. The C_T of the target genes was normalized with the C_T of the *rrsB* to obtain its ΔC_T. The values of ΔC_T of the target genes were further normalized with the ΔC_T of the control cells (*i.e.*, non-exposed cells), the result of which generated the final data set ($\Delta\Delta C_T$) (details provided in ESI).[40, 19]

2.5. Comparison of cultures to acute exposure to AgNPs

Samples were collected from the effluent of the bioreactors EB and CB at 92 hours and 60 hours for runs with specific growth rates of 0.1 h^{-1} and 0.2 h^{-1}, respectively. Bacteria from the samples were harvested and exposed to two concentrations of AgNPs (1mg/L and 10mg/L) to compare the response of the resultant EB and CB cultures for each condition in terms of respirometric activity, membrane permeation and ROS production.

2.5.1. Respirometric analysis. Cell respiration was quantified in non-growing conditions (media consisting on PBS solution and glucose, but not other nutrients), to compare electron transports activity due to the aerobic metabolization of the carbon

source. Respiration activity was determined through the reduction of tetrazolium dye[41] measuring absorbance at 590 nm every 0.25 hour for 5 hours.

2.5.2. Membrane permeation analysis. The membrane permeation of *E. coli* was determined using the Baclight kit (propidium iodide and SYTO 9) with a microplate reader. Propidium iodide becomes intercalates to the DNA only when the membrane is disrupted, while SYTO 9 indicates intact membranes.[41] The green/red fluorescence ratio between the EB and CB at the given AgNPs concentration (1 mg/L and 10 mg/L) was calculated as previously reported.[60] The membrane permeation of *E. coli* was determined using the Baclight kit (propidium iodide and SYTO 9) with a microplate reader. Propidium iodide becomes intercalates to the DNA only when the membrane is disrupted, while SYTO 9 indicates intact membranes.[41] The green/red fluorescence ratio between the EB and CB at the given AgNPs concentration (1 mg/L and 10 mg/L) was calculated as previously reported.[60]

2.5.3. ROS generation measurement using 2',7' –dichlorofluorescin diacetate (DCFH-DA). The reaction between DCFDA and ROS produced fluorescent product 2',7' –dichlorofluorescein (DCF). An oxidation-sensitive fluorescent probe 2',7' –dichlorofluorescein diacetate (DCFH-DA) was measured ROS. Non-fluorescent 2',7' –dichlorofluorescin diacetate (DCFDA) was formed by deacetylation of cellular esterases.[33] Abcam protocol[42] was employed after slight modifications (details in the ESI). Intensity was measured at an excitation wavelength of 488 nm and at an emission wavelength of 535 nm for 12 hours using a fluorescence microplate reader.

2.6. Statistical analysis

The data were analyzed by student's t-test using MATLAB. Differences between means were considered statistically significant at $p < 0.05$. Data are presented as mean ± standard error of the mean (SEM) of at least three independent experiments, unless otherwise stated. T-test analysis was performed to detect the differences between kinetic parameters of control bacteria and AgNPs-exposed bacteria as well as the differences between toxicity effects of nanoparticles on the resultant culture of bioreactors (control bacteria and AgNPs-exposed bacteria). Also, the changes in negative charge of nanoparticles surface in different solutions were assessed by t-test analysis.

3. Results and discussion

3.1. Bacterial growth

Fig. 6 shows the evolution of the OD600 parameter used to follow the growth of the bacteria inside the bioreactors.

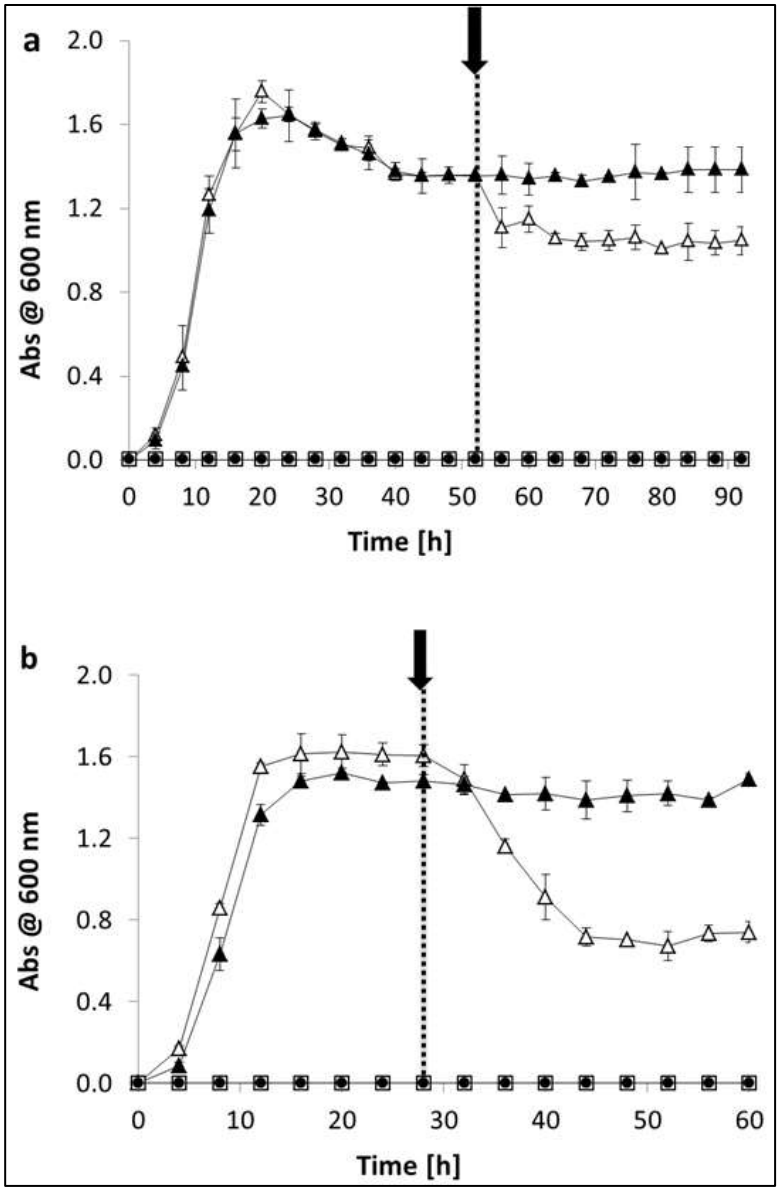

Fig. 6 Effect of continuous injection of AgNPs [1 mg/L] on *E. coli* growth at two specific growth rates in continuous culture. (a) 0.1 h^{-1} and (b) 0.2 h^{-1}. ▲ bacteria without AgNPs, Δ bacteria exposed to AgNPs. ● M9 media in absence of bacteria or AgNPs. □ M9 media and AgNPs. The arrow and dashed line show time when AgNPs injected. Bars represent the error between duplicates reactors.

Fig. 6 shows that at both conditions blank vessels maintain a value of zero, indicating a lack of contamination. As expected, at both growth conditions, all inoculated bioreactors reached steady state at similar times. After steady state was achieved, for each run, two bioreactors were used for the exposure condition (EB) while the other two were left undisturbed for control purposes. After AgNPs injection, there was a period in which biomass decreased for both exposed bioreactors at runs of 0.1 h^{-1} and 0.2 h^{-1}, however in both cases these bioreactors achieved a new steady state condition after 8 h and 16 h, for the 0.1 h^{-1} and 0.2 h^{-1} conditions, respectively. At the end of the experiments, the exposed bioreactor operating at 0.1 h^{-1} (EB-0.1) showed a 15.4% lower concentration of bacteria compared to the control bioreactors operating at 0.1 h^{-1} (CB-0.1). The reduction of bacteria concentration was 56.3% in the EB-0.2 reactors compared to CB-0.2. These results showed that at the conditions tested, microorganisms growing at a lower specific growth rate are less inhibited in term of biomass, compared to those growing at a higher growth rate. The total silver concentration in the blank bioreactors (M9, no bacteria) was very close to 1 mg/L (Figure S5 in the ESI). However, in all exposed bioreactors the concentration of AgNPs was lower than the desired value due to possible trapping in the pellets of bacteria during the centrifugation step of the sampling process.

3.2. Kinetic parameters comparison at different specific growth rates

Table 3 shows the concentration of bacteria inside the biore`actors (X), concentration of glucose inside the bioreactors (S), saturation constant (K_s), yield coefficient ($Y_{x/s}$), maximum yield coefficient (Y_{max}), and maintenance coefficient (m_s).

Table 3. Kinetic parameter of *E. coli* at 0.1 h^{-1} and 0.2 h^{-1} for exposed and control bioreactors

Kinetic Parameter	Control μ =0.1 h^{-1}	Control μ =0.2 h^{-1}	Exposed μ =0.1 h^{-1}	Exposed μ = 0.2 h^{-1}
X (mg cell/L)	1.06±0.05	0.62±0.02	0.7±0.01	0.29±0.01
S_{out} (mmol/L)	0.78±0.036	21.04±0.8	1.38±0.03	28.24±0.26
$S_{consumed}$ (mmol/L)	43.22± 0.04	22.96± 0.8	42.62± 0.03	15.76± 0.26
K_s (mmol/L)	0.84±0.03	0.84±0.03	1.53±0.03	1.53±0.01
μ (h^{-1})	0.1	0.2	0.1	0.2
$Y_{x/s}$ (mg cell/mmol S consumed)	0.025± 0.0012	0.027± 0.002	0.016± 0.0003	0.018± 0.0015
Y_{max} (mg cell/mmol S consumed)	0.03		0.02	
m_s (mg cell/mmol S consumed.h^{-1})	0.754		1.146	

After the injection of AgNPs, K_s for the exposed bioreactors (EB-0.1 and EB-0.2) increased 82% compared to their respective controls (CB-0.1 and CB-0.2).

K_s for EB-01 and EB-0.2 were the same because the concentration of AgNPs in both cases was the same, which agree with kinetic inhibitory models. These results agreed with Bhattacharya and Mukherjee,[43] who reported that the inhibition of sugar metabolism was due to the inactivation of the phosphomannose isomerase enzyme in the bacteria because of their interaction with the AgNPs.

Both EB-0.1 and EB-0.2 had a significant reduction in the yield coefficient ($Y_{x/s}$) compared to their respective controls (p = 0.01 and p = 0.001, respectively).

An increase in the maintenance coefficient for EB cultures was detected. In addition, the maximum biomass yield for EB cultures decreased ~33% compared to the controls. The decrease in Y_{max} in the EB was attributed to the increase in m_s. The maintenance coefficient (m_s) depends partially on the cellular requirements for osmoregulation,[44] and these results showed that chronic exposure to the AgNPs can affect cell requirements. The changes of Y_{max} with specific growth rate in continuous systems were similar to those obtained at different times in batch cultures.[45] These results demonstrated the different effects on the cells' physiology and regulatory pathways when the tests were performed in both batch and continuous systems.[45] This highlighted the difficulties involved in interpreting the data and drawing general conclusions when using different bioreactor configurations.

3.3. Nanoparticles-EPS interactions

3.3.1. Effect of growth conditions on particle size and zeta potential. The hydrodynamic diameters of the AgNPs in pristine M9 minimal medium and in the ES of the exposed bacteria were measured at 32 hours for both growth rates conditions (Table S5 in the ESI). Also, the stability of the AgNPs in distilled water (DI) was determined as a control (Figure S7 in the ESI). These results showed that ES reduced the stability of the nanoparticles in terms of size and zeta potential for both tested growth rate conditions. Major changes were observed at the EB-0.1 bioreactor where the lower zeta potential values of the AgNPs were detected (p = 0.0001) in comparison to EB-0.2. This can be explained by the attachment of the protein corona to the surfaces of the nanoparticles as reported by Shannahan *et al*.[46]

Since the biomass evolution profiles of the EB-0.1 cultures were less inhibited by the AgNPs, Cryo-TEM images were only collected for this condition (Fig. 7).

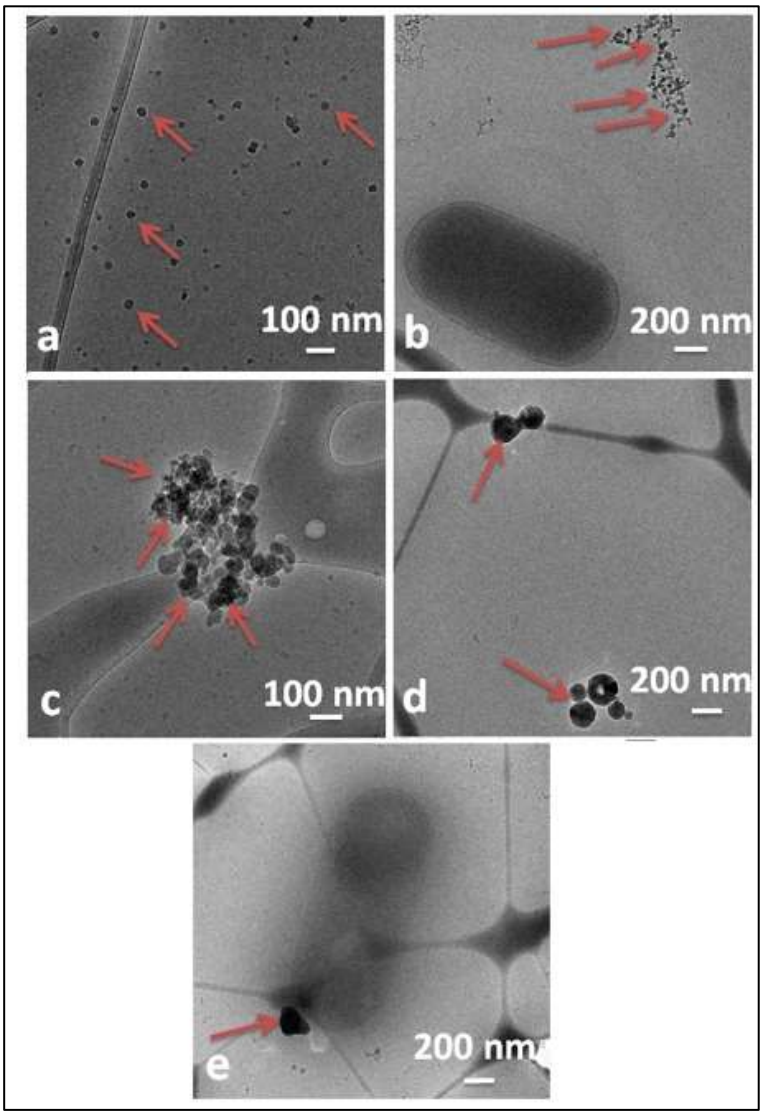

Fig. 7 Cryo-TEM images of bacteria- nanoparticles interaction, ES- nanoparticles interaction, and protein corona formation on nanoparticles surface from exposed bioreactor operating at $0.1h^{-1}$ (EB-0.1) after 8 hours and 32 hours after dosing of nanoparticles started. (a) AgNPs in DI water. (b) Released ES with trapped nanoparticles inside after 8 hours from dose. (c) Magnified ES-nanoparticles interactions from (a). (d) AgNPs-ES complex after 32 hours from starting dose showing large size distribution. (e) AgNPs-ES complex outside cell prevented from penetration. Red arrows represent nanoparticles.

For reference, images of AgNPs in DI water were also collected (Fig. 7a). ES from EB-0.1 images showed that the nanoparticles were trapped in the ES after 8 hours in the bioreactor (Fig. 7b). The images also showed that agglomeration increased after 32 hours at EB-0.1 (Fig. 7c). These results suggested that nanoparticle-ES interactions can lead to biological corona formation on the surfaces of the nanoparticles due to the high affinity of the nanoparticle surface with sulfur- or nitrogen-containing compounds, especially amino acids.[19] Since protein corona is an unstable form of assembly on the surfaces of the nanoparticles,[47,48] different AgNPs sizes can be observed in Fig. 7d. Therefore, the surface of the AgNPs had been modified and these nanoparticles could not pass through cell membranes (Fig. 7e).

3.3.2. Formation of protein corona on the surfaces of the nanoparticles. Protein conformation of α-helices and β-sheets were examined in samples collected from EB-0.1, CB-0.1 and EB-0.2, CB-0.2 at 8 hours and 32 hours. Fig. 8 shows that the ratio of the area representing β-sheets to the area of α-helix was < 1 for all conditions except AgNPs in ES from EB-0.1. At the EB-0.1 condition**,** the ratio values of β-sheets integral to α-helix integral were 3.1 and 2.4, at 8 hours and 32 hours, respectively. This suggests that the nanoparticles induced a reduction of protein content in the α- helix or enhanced the conformational entropy of the protein.[3,32]

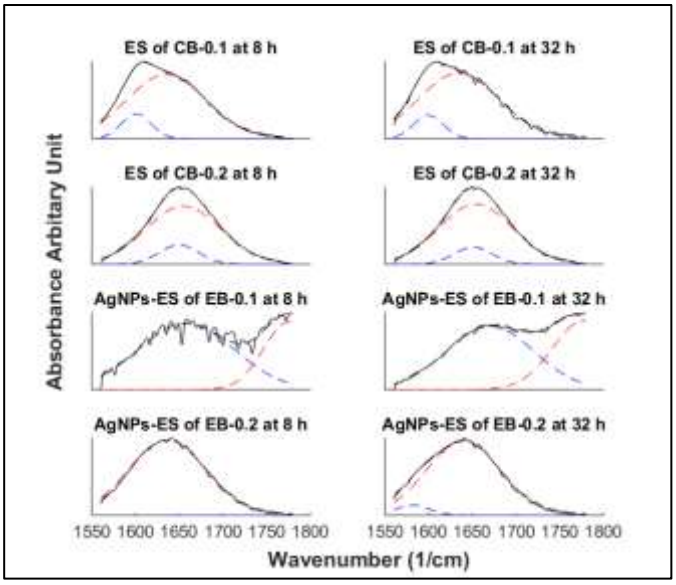

Fig. 8 FTIR spectra of 1800-1550 cm^{-1} region for ES released by control bacteria as well as obtained ES from AgNPs exposed bacteria for both specific growth rates. Black lines present the raw spectra of protein regions of ES. Blue and red lines show the area under β-sheet structures and α-helix structures of proteins in ES, respectively.

HCA of FTIR data from ES composition showed that ES extracted from EB-0.1 segregated distinctly from the ES from control groups of 0.2 h^{-1} (Figure S10 in the SI). Therefore, the formation of protein corona on the surface of AgNPs depended on the composition of ES released by bacteria at different specific growth rates.

TGA was conducted (weight loss *vs.* temperature) to determine thermal stability of the ES that were interacting with the AgNPs. The analysis was performed using derivative thermogravimetric analysis (DTG) from the TGA results. The thermal stability of the ES at CB-0.1 showed a double peak at DTG, which exhibited 30% weight loss at 100 °C followed by a minor peak at 300 °C with less than 5% weight loss (Fig. 9a) and (Figure S11a in the ESI). In addition, DTG of AgNPs-ES at EB-0.1 (Fig. 9a) showed a

major peak at 100 °C to 200 °C associated with 20% weight loss, and this was followed by a minor peak at 400 °C with less than 10% weight loss. On the other hand, ES at CB-0.2 had a double peak with 20% weight loss at 100 °C and 220 °C (Fig. 9b). However, AgNPs-ES at EB-0.2 (Fig. 9b) had two more minor peaks with 2% weight loss that were observed at 450 °C to 550 °C in addition to the peaks at 100 °C to 180 °C and 220 °C with 12% weight loss. Thermograms at 700 °C indicated that the AgNPs had the lowest weight loss at EB-0.1, while the ES had their maximum weight loss due to the degradation of protein at the higher temperatures.

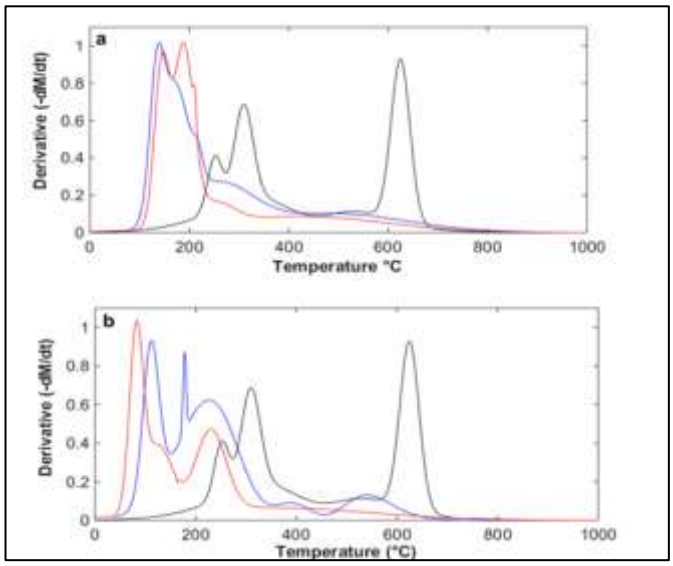

Fig. 9 Derivative thermogravimetric (DTG) curves of AgNPs, ES-AgNPs, and ES. (a) First derivative of thermal stability of AgNPs-ES from EB-0.1 and ES of CB-0.1, and (b) First derivative of thermal stability of AgNPs-ES from EB-0.2 and ES of CB-0.2. Thermal stability of AgNPs-casein was obtained as a reference to compare with interacted AgNPs-ES. Black, blue, and red lines represent AgNPs, AgNPs-ES, and ES, respectively. Data were also obtained by taking the first derivative of the TGA lines. Raw data of TGA were smoothed by a moving average and the Gaussian fit to first derivative of smooth data has been found by MATLAB software.

These results supported the results obtained by ATR-FTIR, which indicated that the AgNPs-ES of EB-0.1 contained proteins[49] from the ES. At EB-0.2, the nanoparticles in the ES were impacted to a lesser extent compared to those in EB-0.1. This could have been due to the concentration and compositional differences of the ES produced at two growth conditions. ES from EB-0.1 formed protein corona, and surface properties changed after 32 hours, which resulted in a negative surface charge (Table S5 in the ESI) and a change in the size of the AgNPs (Figure S8 in the ESI). However,

it was evident that no protein corona was formed at EB-0.2 (Fig. 8). The protein corona formed at EB-0.1 increased the size of the nanoparticles and decreased the penetration of nanoparticles into the cells. These results show the importance of electrostatic and hydrophobic interactions in the formation of the protein corona, and their biological and toxicological implications.

3.4. Gene expression level at two specific growth rates

The results of the analyses indicated that there were several mechanisms by which bacteria responded to AgNPs exposure in both specific growth rates. The results, including various quantities of ES and their compositional characteristics as well as the AgNPs-ES interaction at different specific growth rates, indicated the necessity of investigating both specific growth rates on the gene expression level of eight target genes (*ompF, cueO, cusA, soxS, cpsB, zwf, copA*, and *fabR*) normalized using an internal reference gene, *rrsB* (Fig. 10).

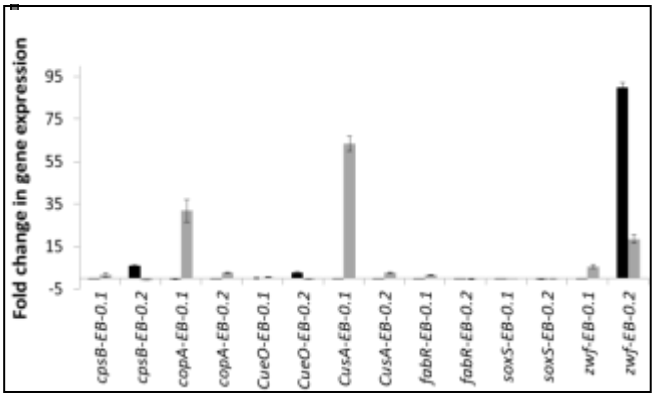

Fig. 10 Quantitative amplification data of the target genes from continuous bioreactor products in response to AgNPs. Black and grey marks represent samples at 8 hours and 32 hours, respectively after continuous injection of AgNPs. Fold change in gene expression is relative to non-exposed control. Gene expressions were normalized against internal reference gene, *rrsB*. The error bars are the standard error of the mean of three technical replicate from two bioreactors at the same condition.

In this study, the membrane in EB was protected by the response of up-regulated genes, such as *copA* and *cusA* to AgNPs at both specific growth rates. These genes are responsible for silver and copper efflux of membrane transporter, lipid biosynthesis, and silver-translocating P-type ATPase efflux pump. Nanoparticles mediate the generation of ROS and also modulate the antioxidant activities of ROS-metabolizing enzymes, such as slow electron transport, the NADPH-dependent flavor enzyme, catalase, glutathione peroxidase, and superoxide dismutase.[33] In general, the *soxS* and *cueO*[19,33] genes, which are responsible for ROS expression, were not affected by the AgNPs at EB-0.1, however, only *cueO* genes were up-regulated at EB-0.2. Also, *zwf* gene showed higher expression at EB-0.2 in compare with EB-0.1 which may be associated with changes in the metabolic pathway of glucose-6-phosphate

dehydrogenase in the respiration process[33] and/or the relatively impenetrable membrane of EB-0.1.[50] At EB-0.1, the nanoparticles could not cause the generation of ROS, so the cells were not involved in compensating for the disruptive impacts of the nanoparticles due to the formation of ROS. However, the activation of the *copA*, *cpsB*, *fabR*, and *cusA* regulons prevented irreversible damage to EB-0.1.

3.5. Comparison of cultures to acute exposure to AgNPs

Since the continuous culture results showed different responses at the two specific growth rates, we compared the response of the resultant culture at these two conditions to acute exposure to nanoparticles in terms of: respiration activity, membrane permeation, and intracellular ROS production. These tests were performed in batch conditions using the resultant cultures from the control bioreactors (CB) and exposed bioreactors (EB). In addition, no nanoparticles for the negative control and 10 mg/L for the positive control were applied for the inhibitory effect of AgNPs.

3.5.1. Inhibitory effect on respiration. Fig. 11 shows no differences between the percent of remaining respiration (PRR) of EB and CB groups at both specific growth rates ($p > 0.05$) when they were exposed to different nanoparticle concentrations. Silver ions released from the nanoparticles are the main mechanism for metabolic disruption of bacteria. These results showed that at batch growing conditions, the resultant cultures respond similarly to nanoparticle exposure.

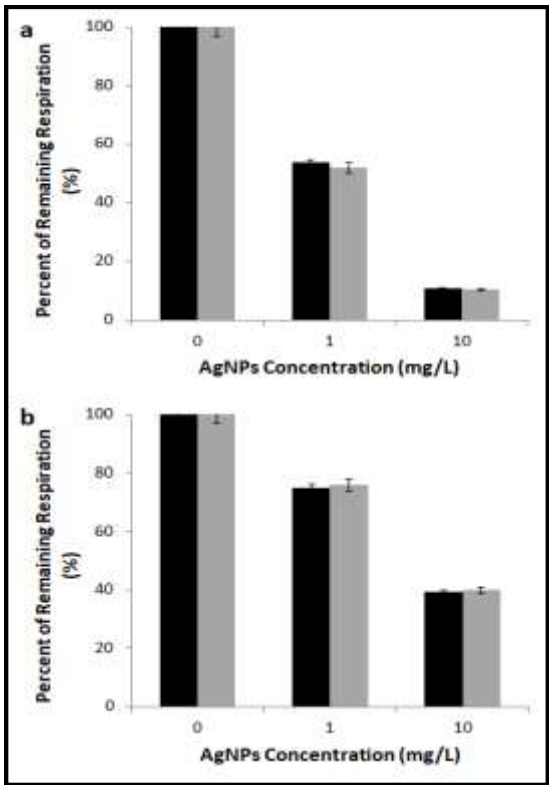

Fig. 11 Represents percent of remaining respiration (PRR) of continuous bioreactor products including AgNPs-exposed bioreactor (EB) and control bioreactor (CB) under AgNPs (1 mg/L, and 10 mg/L). a) PRR values of CB and EB of 0.1 h^{-1}, and b) PRR values of CB and EB of 0.2 h^{-1}. Black marks show CB and gray marks represent EB. Each value represents an average of 6 wells from two duplicate 96 well microplates.

3.5.2. Inhibitory effect on membrane permeation. The undisturbed cell membrane (UCM) results shown in Fig. 12 indicate that the inhibitory effect of the AgNPs (1 mg/L) on EB after exposure to AgNPs at both 0.1 h^{-1} and 0.2 h^{-1} was lower than that of CB exposed to AgNPs. The statistical analysis confirmed that low concentrations (1 mg/L) of the AgNPs had a higher inhibitory effect on the CB at 0.1 h^{-1} and 0.2 h^{-1} than they had on EB-0.1 and EB-0.2 (p = 0.09 and p = 0.02, respectively). Shokri *et al.*[50] reported that the cyclic fatty acids of *E. coli* were

increased at lower growth rates. Hence, the mechanical strength of the cell membranes showed high resistance to sonication and osmotic shock/enzymatic treatment.[50] In comparison to a previous study,[1] a slight high inhibitory effect was observed at a low AgNPs (1 mg/L) concentration and there was no physical damage to the bacteria at high concentrations of AgNPs (15 mg/L and 50 mg/L). This was due to the aggregation of the AgNPs at high concentrations and the decreased steric forces due to the release of ES during bacteria metabolism.[1]

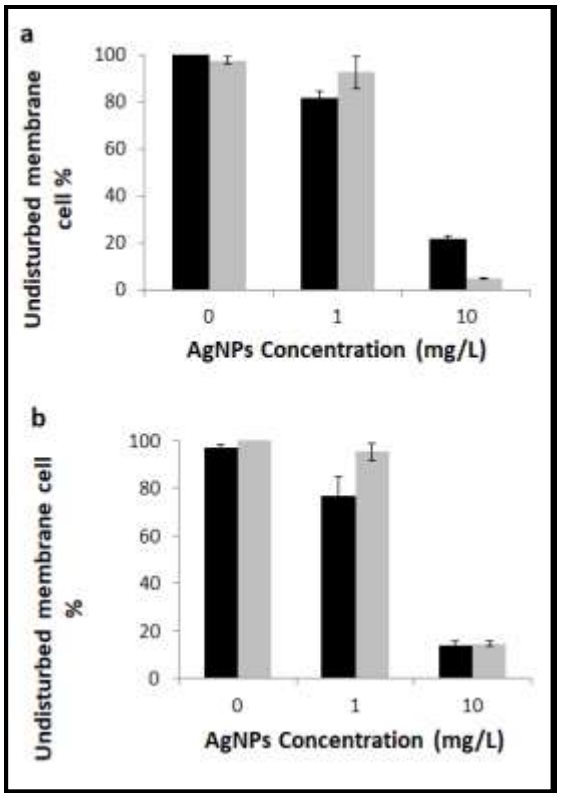

Fig. 12 Represents undisrupted cell membrane (UCM) of continuous bioreactor products including AgNPs-exposed bioreactor (EB) and control bioreactor (CB) under AgNPs (1 mg/L, and 10 mg/L). UCM values were measured at 5 hours a) CB and EB of 0.1 h^{-1}, and b) CB and EB of 0.2 h^{-1}. Black marks show CB and gray marks represent EB. Each value represents an average of 6 wells from two duplicates microplates.

3.5.3. Evaluation of the generation of ROS. When CB-0.1 was exposed to 1 mg/L of AgNPs, the fluorescence increased, although the exposure of EB-0.1 to AgNPs (1 mg/L) did not show any significant generation of ROS (p = 0.89) (Fig. 13a). Fig. 13b shows that high levels of ROS were generated in EB-0.2 at 12 hours. Hence, the level of fluorescence was not statistically different between the CB-0.2 and EB-0.2 after exposure to 1 mg/L of AgNPs (p = 0.93). The resultant cultures from EB and CB bioreactors have different responses to acute exposure to nanoparticles in terms of

membrane permeation and ROS formation for both specific growth rates. Significant ROS generation and UMC were observed between CB and EB, which contrast with PRR between CB and EB in the same condition. This suggested that ROS generated during electron transport is slowed by high mitochondrial membrane potential.[51] Hence, oxygen radicals react with oxygen dissolved in the membrane and cause the membrane disruption.

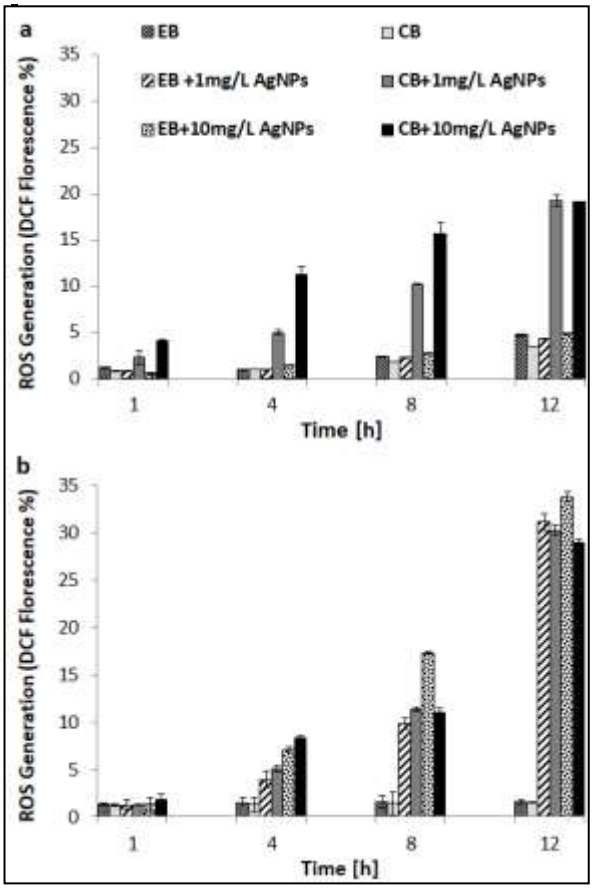

Fig. 13 Represents reactive oxygen species level (ROS) of bioreactor culture products for exposed bioreactor (EB) and control bioreactor (CB) contacted with AgNPs (1 mg/L, and 10 mg/L). ROS generation value in a) CB and EB of 0.1 h^{-1}, and b) CB and EB of 0.2 h^{-1}. Each value represents an average of 6 wells from two duplicates 96 well microplates.

4. Discussion

In terms of AgNPs impacts on kinetic parameters, our results showed that the microbial population continues to grow in the presence of the AgNPs, however, metabolic activity is impaired. This is demonstrated by changes in the kinetic parameters (decrease of $Y_{x/s}$ and Y_{max} as well as increase of K_s, and m_s). The metabolic changes led to a new steady state for a continuous culture in which

the resultant concentration of biomass is lower than that obtained at the steady state in non-exposed conditions. Thus, the resultant biomass concentration was inversely dependent on the specific growth rate (high specific growth rate, low end biomass concentration).

Kinetic parameter analysis helps us to understand the fate of the microbial population as a whole, but it does not provide insight into the mechanism(s) governing the observed effect. As such, bio-macromolecule analysis was utilized to elucidate the phenomena. The results from the AgNPs-ES interaction showed that different compositions of ES were produced at the two tested conditions (0.1 h^{-1} and 0.2 h^{-1} specific growth rate). The concentration of extracted ES from the continuous culture was quantified and normalized to the OD600 bacteria concentration (Figure S9 in the ESI). In general, the concentration of ES at 0.1 h^{-1} was higher than 0.2 h^{-1}. After nanoparticle injection, the concentration of ES at EB-0.1 slowly increased until 32 hours. At EB-0.2, a temporary spike in ES concentration was observed at between 8 and 16 hours after AgNPs injection, however, this concentration sharply decreased by the end of the experiment. These findings agreed with Williams and Wimpenny[8] who reported that ES production decreases with an increase in the specific growth rate. An increase in ES due to nanoparticles was also observed by Zhang *et al*. using mixed cultures.[52]

Notably, the ES composition of the AgNPs-exposed bioreactors were different than the controls at the same condition as evidenced by the hierarchical cluster analysis of FTIR data (HCA, Figure S10 in the ESI). This study supports

the idea that changes on the surface properties of AgNPs, at the two culture conditions, were due the production and excretion of ES with different compositions at the two specific growth rates tested. These varieties of ES composition were demonstrated by the TGA analysis. The TGA results for the AgNPs-ES complexes obtained from EB-0.1 supported the evidence regarding protein corona formation on the surface of the AgNPs. Li *et al*.[7] reported that total cellular polysaccharide (combination of ES and intracellular polysaccharide) decreased as the specific growth rate increased, while protein concentration increases. This was in agreement with the TGA result regarding the increase in protein of AGNPs-ES at EB-0.1. Moreover, FTIR showed that the ratio of the area representing β-sheets to the α-helix of AgNPs-ES at EB-0.1 was higher than EB-0.2, which was induced due to the increase in β sheet content or due to the fortification of the conformational entropy of the protein at EB-0.1.[3, 32] These results showed that *E. coli* produces more effective ES in terms of nanoparticles destabilization at lower specific growth rates.

In the context of transcriptomic analysis, the main genes that respond to chronic levels of continuous stress due to the nanoparticles are *zwf, CusA,* and *copA*. Specifically, the up-regulation of the *zwf* and *copA* genes was in agreement with the changes in growth parameters such as K_s, Y_{max} and m_s in the exposed bioreactors. The *zwf* gene could lead to a K_s increase, while decreasing $Y_{max,}$ in two ways, inactivation of phosphomannose by the AgNPs, and a drop in the efficiency of sugar metabolism.[43] The *copA* gene in the exposed cultures translocated silver thru the ATPase efflux pump by increasing m_s. Furthermore,

the upregulation of the *cpsB* gene, production of capsular polysaccharide and canonical regulatory transcription,[39] was faster at EB-0.1 than EB-02, which showed a faster metabolic pathway response to the stressors for cultures growing at lower specific growth rates.[53] These results are evidence that cell requirements increase due to chronic exposure to AgNPs.

Finally, the acute test results showed that even if bacteria are able to adapt to nanoparticles, they cannot transfer this adaptability to the following generations over 114 generations at 0.2 h^{-1} (number of *E. coli* generation during 32 hours of nanoparticles exposure). However, at 0.1 h^{-1}, the number of generations was 206, which increases the probability of bacterial adaptation to nanoparticles, which was in agreement with the acute tests. In this content, UCM and ROS generation between CB and EB showed that at a EB condition, nanoparticles did not significantly disrupt the cell membrane, and did not produce oxidative damage by ROS. Hence, EB are not compensating for a lower disruptive effect from nanoparticles than CB when they are exposed to nanoparticles of 1 mg/L. However, the low PRR for the 0.1 h^{-1} resultant culture when exposed to AgNPs indicates the impact of culturing conditions on the bacterial response to AgNPs. Bacteria in a continuous culture caused the reduction in the inhibitory effect of AgNPs by producing ES, especially at 0.1 h^{-1}. Therefore, the higher expression of the *zwf* gene at EB-0.2 in comparison with EB-0.1 was associated with the relatively modified surface chemistry of nanoparticles in EB-0.1 in a continuous culture. Hence, the PRR between CB and EB showed that the changes observed were a phenotypic response to the stress conditions and not permanent changes

in the bacterial respiration mechanism. Wang *et al.* reported on the highly conserved nature of bacteria, which protect them from change through only a few genetic mutations.[54] This study is in agreement with the results obtained from the higher growth rate condition. However, another study claimed that genomic analysis of AgNPs exposed *E.coli* showed resistance by generation 200, where three mutations smoothly occurred in AgNPs resistance bacteria[2].

These studies indicate that despite previous claims to the contrary, bacteria can easily evolve resistance to AgNPs, and this occurs by relatively simple genomic changes in a few generations. In conventional batch tests, since the contact time was 5 hours, the number of generations that were exposed to nanoparticles was 17, which means that at a batch culture condition the probability of adaptation is even lower than that for a continuous culture, unless the specific growth rates of a culture are high enough to decrease the number of generations. Hence, at lower specific growth conditions, the probability of producing nanoparticle- resistant bacteria will increase. Therefore, the bacterial culture condition influences the inhibitory effect of nanoparticles by changing their physiochemical properties, and also caused permanent bacterial resistance.

5. Conclusions

The fate of nanoparticles and their inhibitory effects in a continuous culture depends on the bacterial specific growth rate associated with different concentrations and the composition of ES produced at each growth condition. ES at a lower growth rate are more effective in reducing the inhibitory effect of the nanoparticles. This occurs thru consumption of ROS, immobilization of the

nanoparticles, and the formation of protein corona on the surfaces of the nanoparticles. Cultures exposed to nanoparticles are able to growth and achieve new stable conditions (steady state) at higher energy consumption than unexposed cultures. This is due to the activation of several regulons, such as *zwf, CusA,* and *copA,* which occurs to prevent irreversible damage from the stress condition.

Conflicts of interest

The authors declare no conflicts of interest.

Acknowledgements

This work was supported by the National Science Foundation under the grant numbers CBET-1350789 and CBET-1055652. The authors would like to appreciate Drs. D. Smith, E. Rubin from Graduate School of Oceanography and the URI Sequencing and Genomic Center.

References

1 N. M. Anaya, F. Faghihzadeh, N. Ganji, G. Bothun and V. Oyanedel-Craver, *Sci. Total Environ.*, 2016, **565**, 841–848.

2 J. L. Graves, M. Tajkarimi, Q. Cunningham, A. Campbell, H. Nonga, S. H. Harrison and J. E. Barrick, *Front. Genet.*, , DOI:10.3389/fgene.2015.00042.

3 F. Faghihzadeh, N. M. Anaya, L. A. Schifman and V. Oyanedel-Craver, *Nanotechnol. Environ. Eng.*, 2016, **1**, 1.

4 A. Ivask, I. Kurvet, K. Kasemets, I. Blinova, V. Aruoja, S. Suppi, H. Vija, A. Käkinen, T. Titma, M. Heinlaan, M. Visnapuu, D. Koller, V. Kisand and A. Kahru, *PLoS ONE*, , DOI:10.1371/journal.pone.0102108.

5 K. Ikuma, A. W. Decho and B. L. T. Lau, *Front. Microbiol.*, , DOI:10.3389/fmicb.2015.00591.

6 E. Gulot, P. Georges, A. Brun, M. P. Fontaine-Aupart, M. N. Bellon-Fontaine and R. Briandet, *Photochem. Photobiol.*, 2002, **75**, 570–578.

7 M. Li, P. Nkrumah and M. Xiao, *Inland Waters*, 2014, **4**, 357–362.

8 A. G. Williams and J. W. T. Wimpenny, *J. Gen. Microbiol.*, 1978, **104**, 47–57.

9 Z. Fencl, J. Řičica and J. Kodešová, *J. Appl. Chem. Biotechnol.*, 1972, **22**, 405–416.

10 K. Kovárová-Kovar and T. Egli, *Microbiol. Mol. Biol. Rev. MMBR*, 1998, **62**, 646–666.

11 P. De Leenheer and N. G. Cogan, *J. Math. Biol.*, 2009, **59**, 563–579.

12 M. Lin, H. F. Huo and Y. N. Li, , DOI:10.1016/j.nonrwa.2012.02.016.

13 T. King, S. Seeto and T. Ferenci, *Genetics*, 2006, **172**, 2071–2079.

14 D. Fraser and M. Kaern, *Mol. Microbiol.*, 2009, **71**, 1333–1340.

15 D. Mu, X. Yu, Z. Xu, Z. Du and G. Chen, *Sci. Rep.*, 2016, **6**, 29953.

16 W. Harder and L. Dijkhuizen, *Philos. Trans. R. Soc. Lond. B. Biol. Sci.*, 1982, **297**, 459–480.

17 H. Veldkamp and H. W. Jannasch, *J. Appl. Chem. Biotechnol.*, 1972, **22**, 105–123.

18 K. M. Peil and A. F. Gaudy, *Appl. Microbiol.*, 1971, **21**, 253–256.

19 J. S. McQuillan and A. M. Shaw, *Nanotoxicology*, 2014, **8**, 177–184.

20 Escherichia coli (Migula) Castellani and Chalmers ATCC ® 700926&tr, https://www.atcc.org/Products/All/700926.aspx#culturemethod, (accessed February 6, 2017).

21 Y. Jiao, G. D. Cody, A. K. Harding, P. Wilmes, M. Schrenk, K. E. Wheeler, J. F. Banfield and M. P. Thelen, *Appl. Environ. Microbiol.*, 2010, **76**, 2916–2922.

22 G. Molin, *Eur. J. Appl. Microbiol. Biotechnol.*, 1983, **18**, 303–307.

23 R. M. Maier, I. Pepper and C. Gerba, *Environ. Microbiol.*, 2000, 43–59.

24 J. Glazyrina, E.-M. Materne, T. Dreher, D. Storm, S. Junne, T. Adams, G. Greller and P. Neubauer, *Microb. Cell Factories*, 2010, **9**, 42.

25 S. Ganal, C. Gaudin, K. Roensch and M. Tran, *J Exp Microbiol Immunol*, 2007, **11**, 54–59.

26 J. Monod, *Annu. Rev. Microbiol.*, 1949, **3**, 371–394.

27 S. J. Pirt, *Proc. R. Soc. Lond. B Biol. Sci.*, 1965, **163**, 224–231.

28 A. Xi and G. D. Bothun, *The Analyst*, 2014, **139**, 973–981.

29 S. R. Chowdhury, S. Manna, P. Saha, R. K. Basak, R. Sen, D. Roy and B. Adhikari, *J. Appl. Microbiol.*, 2011, **111**, 1381–1393.

30 J. H. Ward, *J. Am. Stat. Assoc.*, 1963, **58**, 236.

31 Q. Lin, C. Mao, A. Kong, X. Bu, X. Zhao and P. Feng, *J. Mater. Chem. A*, 2017, **5**, 21189–21195.

32 N. Durán, C. P. Silveira, M. Durán and D. S. T. Martinez, *J. Nanobiotechnology*, 2015, **13**, 55.

33 A. Baez and J. Shiloach, *Microb. Cell Factories*, 2013, **12**, 1.

34 J. S. McQuillan, H. G. Infante, E. Stokes and A. M. Shaw, *Nanotoxicology*, 2012, **6**, 857–866.

35 J. McQuillan, .

36 K. Arunasri, M. Adil, K. Venu Charan, C. Suvro, S. Himabindu Reddy and S. Shivaji, *PLoS ONE*, 2013, **8**, e57860.

37 K. W. Kinzler, *Gene Expr.*, 1999, **270**, 484–487.

38 Z. Rahman, N. Rashid, J. Nawab, M. Ilyas, B. H. Sung and S. C. Kim, *Environ. Sci. Pollut. Res.*, 2016, **23**, 12007–12018.

39 G. Huang, D. Xia, T. An, T. W. Ng, H. Y. Yip, G. Li, H. Zhao and P. K. Wong, *Appl. Environ. Microbiol.*, 2015, **81**, 5174–5183.

40 M. W. Pfaffl, *Real-Time PCR*, 2006, **63**, 63–82.

41 N. M. Anaya, F. Solomon and V. Oyanedel-Craver, *Environ. Sci. Nano*, , DOI:10.1039/C5EN00074B.

42 DCFDA - Cellular Reactive Oxygen Species Detection Assay Kit (ab113851) | Abcam, http://www.abcam.com/dcfda-cellular-reactive-oxygen-species-detection-assay-kit-ab113851.html, (accessed February 6, 2017).

43 R. Bhattacharya and P. Mukherjee, *Adv. Drug Deliv. Rev.*, 2008, **60**, 1289–1306.

44 X. Wu, R. Altman, M. A. Eiteman and E. Altman, *Appl. Environ. Microbiol.*, 2014, **80**, 2880–2888.

45 J. H. Seo and J. E. Bailey, *Biotechnol. Bioeng.*, 1986, **28**, 1590–1594.

46 J. H. Shannahan, X. Lai, P. C. Ke, R. Podila, J. M. Brown and F. A. Witzmann, *PLoS ONE*, , DOI:10.1371/journal.pone.0074001.

47 M. Mahmoudi, I. Lynch, M. R. Ejtehadi, M. P. Monopoli, F. B. Bombelli and S. Laurent, *Chem. Rev.*, 2011, **111**, 5610–5637.

48 S. Lara, F. Alnasser, E. Polo, D. Garry, M. C. Lo Giudice, D. R. Hristov, L. Rocks, A. Salvati, Y. Yan and K. A. Dawson, *ACS Nano*, , DOI:10.1021/acsnano.6b07933.

49 M. M. Yallapu, N. Chauhan, S. F. Othman, V. Khalilzad-Sharghi, M. C. Ebeling, S. Khan, M. Jaggi and S. C. Chauhan, *Biomaterials*, 2015, **46**, 1–12.

50 A. Shokri, A. M. Sandén and G. Larsson, *Appl. Microbiol. Biotechnol.*, 2002, **58**, 386–392.

51 M. P. Murphy, *Biochem. J.*, 2009, **417**, 1–13.

52 C. Zhang, Z. Liang and Z. Hu, *Water Res.*, 2014, **50**, 350–358.

53 J. Zeng, J.-M. Gao, Y.-P. Chen, P. Yan, Y. Dong, Y. Shen, J.-S. Guo, N. Zeng and P. Zhang, *Sci. Rep.*, 2016, **6**, 26721.

54 L. Wang, C. Hu and L. Shao, *Int. J. Nanomedicine*, 2017, **12**, 1227–1249.

55 C. M. Hessler, M.-Y. Wu, Z. Xue, H. Choi and Y. Seo, *Water Res.*

SUPLEMENTARY INFORMATION

Additional details for method

1.1. Experimental conditions and toxicity tests

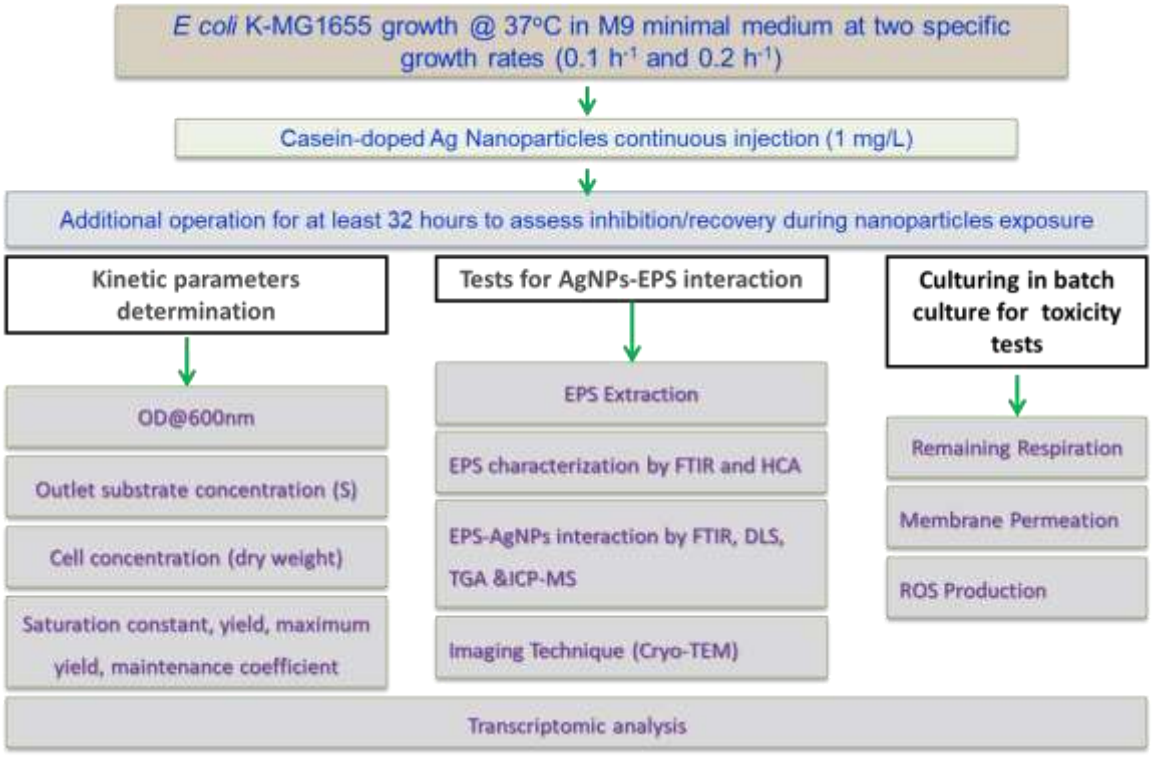

Figure S1. Condition and tests performed in this study

1.2. Kinetic parameters determination in details

1.2.1. Maximum specific growth rate

First we performed the batch culture to find the optimum temperature and optimum substrate concentration for *E.coli* Mg1655 growth. The μ_{max} depends on the culture temperature,[1] hence, temperatures in the range of 37 °C – 40 °C were examined in a batch bioreactor to find the optimum temperature for *E. coli* growth. Also, at high substrate concentration, growth will occur at μ_{max}. Therefore, to determine the

optimum substrate concentration, two concentrations of glucose (8 g/L and 20 g/L) as the only carbon source.[1,2] Then, the μ_{max} of *E. coli* was determined by batch culture in optimum growth condition (temperature = 37 and glucose concentration = 8 g/L). For this purpose, direct measurements of μ_{max} carried out in a batch bioreactor (**Error! eference source not found.**b).

Also, in order to obtain the wash out dilution factor the experiment was performed with six bioreactors: four bioreactors inoculated with 300 µl of *E. coli* (OD at 600nm was 1.8) and 2 bioreactors as controls contained only M9 minimal media. A concentration of 8 g/L of glucose as the only carbon source was added into minimal M9 media container. Initial µ was 0.1 h^{-1} which increased to 0.2 h^{-1} after 20 hours and finally increased to 0.3 h^{-1} after 32 hours. As shown in **Error! Reference source not ound.**a, after increasing specific growth rate to 0.3 h^{-1}, the cells start to wash out.

As the optimum specific growth rates for the investigating the response of cells at different specific growth rates to AgNPs, 0.1 h^{-1} and 0.2 h^{-1} were selected.

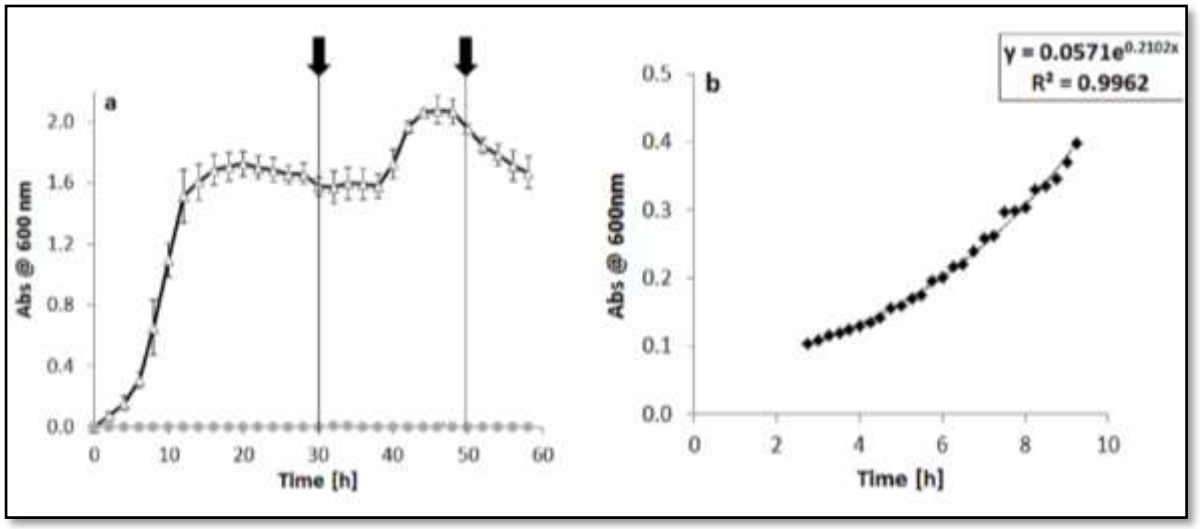

Figure S2. μ_{max} of *E. coli* determined by two methods including batch and continuous cultures. (a) μ_{max} of *E. coli* in continuous culture obtained by increasing specific growth rate (μ). Growth started with μ at 0.1 h^{-1}, increased to 0.1 h^{-1} at 30 hours, and finally increased to 0.3 h^{-1}. Bold black arrows represent the time of increasing μ. Δ represents bacteria control exposed to AgNPs. ● represents a M9 minimal media control to detect contamination. Samples were collected every 2 hours. Bars represent two replicates. (b) μ_{max} of *E. coli* in M9 minimal media in 96 well microplates with glucose concentration of 8 g/L and temperature at 37 °C. Samples were run in triplicate.

1.2.2. Cell dry weight

Then, we found the cell dry weight for each condition by multiplying cell dry weight with the absorbance at OD600. In detail, 1 ml of cell suspension was centrifuged in pre-dried and pre-weighed 1 ml test tubes at 13000 × g for 5 min. After removal of the supernatant, the samples were measured for cell wet weight and then dried at vacuum for at least 24 hours.[47] The dry biomass weight obtained for all four bioreactors. Then, they normalized based on the inside volume of continuous bioreactor's vessels.

1.2.3. Substrate concentration

We determined the outlet substrate concentration (S_{out}) by using Glucose (HK) Assay kit. The glucose consumption rate as an only carbon source were determined by the glucose (HK) assay reagent (Product Code G 3293) which purchased from Sigma Aldrich. The protocols for glucose concentration determined as given in the manufacturers' instructions. The concentration of glucose in the samples was

calculated using the millimolar extinction coefficient or NADH at 340 nm using the equation shown below as given in the manufacturers' instructions.

mg glucose/ml = (ΔA)(TV)(Glucose MW)(F)/ (ε)(d)(SV)(Conversion Factor for µg to mg)

A is the concentration in term of absorbance at 340 nm.

Where; A Total Blank = A Sample Blank + A Reagent Blank , $\Delta A = A_{Test} - A_{Total\ Blank}$, TV = Total Assay Volume (0.02 ml), SV = Sample Volume (1.02 ml), Glucose MW = 180.15g/mole, F = DF = 4 from sample preparation, ε = Millimolar extinction coefficient for NADH at 340nm =6.22, d = Light path (cm), 1000 = Conversion Factor for µg to mg.

1.2.4. Saturation constant

We normalized the outlet substrate concentration (S_{out}) by bacterial absorbance (OD 600). Then we converted the outlet substrate concentration (S_{out}) unit from mg/mL to mmol/L. We prepared a chart calculating K_s , with 1/µ as y axis and 1/ S_{out} as x axis. K_s was determined by multiplying slope with 1/intersect. Also, we checked K_s values with $K_s=S*((\mu_{max}/\mu)-1)$ equation (Table S 1 and Table S 2).

Table S 1. K_s determination for control bioreactors at two specific growth rates.

µ (1/h)	0.10	0.20
S_{out} (mmol/L)	0.78	21.04
1/µ	10.00	5.00

1/ S_{out}	1.28	0.05
Slope	4.05	
Intersect	4.81	
μ_{max}	0.21	
K_s (mmol/L)	0.84	
	Point 1	Point 2
check for $\mu_{max}=((S+Ks)/S)\mu$	0.21	0.21
check for $Ks=S*((\mu_{max}/\mu)-1)$	0.84	0.84

Table S 2. K_s determination for AgNPs-exposed bioreactors at two specific growth rates.

μ (1/h)	0.10	0.20
S_{out} (mmol/L)	1.38	28.24
$1/\mu$	10.00	5.00

1/ S_{out}	0.73	0.04
slope	7.24	
intersect	4.74	
μ_{max}	0.21	
K_s (mmol/L)	1.53	
	Point 1	Point 2
check for $\mu_{max}=((S+Ks)/S)\mu$	0.21	0.21
check for $Ks=S*((\mu_{max}/\mu)-1)$	1.53	1.53

1.2.5. Substrate mass balance

Also, mass balance for substrate in bioreactors at steady state checked by the following equation:

$$\frac{ds}{dt} = S_{in} - S_{out} - S_{consumed}$$

By applying steady state assumption and rewriting the consumed substrate as the yield coefficient divided by biomass we arrive at following equation:

$$Y_{\frac{x}{s}} = \frac{X}{S_{in} - S_{out}}$$

For each case, the left and right hand side of above equation are as follows:

For control bioreactor at 0.1 h^{-1} => 0.025 = 1.06/(44-0.78) mmol/L

For control bioreactor at 0.2 h^{-1} => 0.027 = 0.62/(44-21.04) mmol/L

For AgNPs-exposed bioreactor at 0.1 h^{-1} => 0.016= 0.7/(44-1.38) mmol/L

For AgNPs-exposed bioreactor at 0.1 h^{-1} => 0.018= 0.29/(44-28.24) mmol/L

1.2.6. Maximum Yield and maintenance coefficient

The maximum yield and maintenance coefficient calculated by the linear regression of 1/μ as x axis and 1/yield as y axis. Slope is the maintenance coefficient and 1/intersect is the maximum yield.

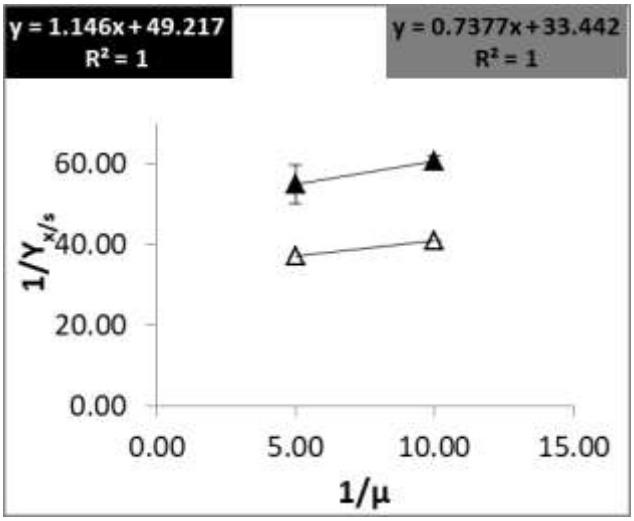

Figure S3. Relation of yield coefficient ($Y_{x/s}$) of *E. coli* to specific growth rate (μ) using double reciprocal linear transformation. Δ, Grey line and grey box represents control bacteria (CB). ▲, Black line and black box represent AgNPs-exposed bacteria (EB).

1.3. *E.coli* number of generation

For continuous culture at steady state phase during the nanoparticles exposure time, cell doubling times (T_d) were calculated as the batch culture. The population of bacteria reduced after the treatment with toxicant which caused the reduction in the rate of cell multiplication[4]. Hence, the doubling time calculation of the conventional bioreactor ($T_d = 0.693/D$) was not applicable. We used the following formula to obtain the doubling time and number of generations:

$$N_t = N_0 * (1 + r)^{Td}$$

Where:

N_t: The amount at time t

N_0: The amount at time 0

r: Growth rate

T_d: doubling time

We obtained the doubling time of 0.28 h at 0.2 h^{-1}, and 0.15 h at 0.1 h^{-1} the number of generation for 32 hours of contact time was 114 at 0.2 h^{-1} and 206 at 0.1 h^{-1}. In batch test, since the contact time was 5 hours, the number of generation was 17.

1.4. Continuous injection of nanoparticles to bioreactors

AgNPs are continuously injected in to the system to achieve 1 mg/L concentration in bioreactors. Precisely, three single syringe infusion pumps were utilized for continuous injection of AgNPs into bioreactors (Figure S4 in the ESI). Based on conservation of mass for AgNPs in distilled water and continuity of the flow we can write:

$$Q_1 + Q_2 = Q_3$$

$$C_1Q_1 + C_2Q_2 = C_3Q_3$$

$$C_3 = C_2Q_2 / Q_3$$

Where Q_1 is M9 minimal culture media inflow rate, C_2 and Q_2 are AgNPs concentration and flow rate, from syringe infusion pump, respectively, as well as Q_3 is the outflow and C_3 is concentration of AgNPs in outflow. Based on this formulation the concentration of AgNPs in outflow is determined and assumed to be equal to AgNPs concentration inside the reactor (Table S 3).

Table S 3. Estimated values for constant concentration of AgNPs inside bioreactors for two specific growth rates

μ (h^{-1})	V	C_1 mg/L	Q_1 mL/min	C_2 mg/L	Q_2 mL/min	C_3 mg/L	Q_3 mL/min
0.1	45 mL	0	0.1	11	0.01	1	0.11
0.2	40 mL	0	0.13	14	0.01	1	0.14

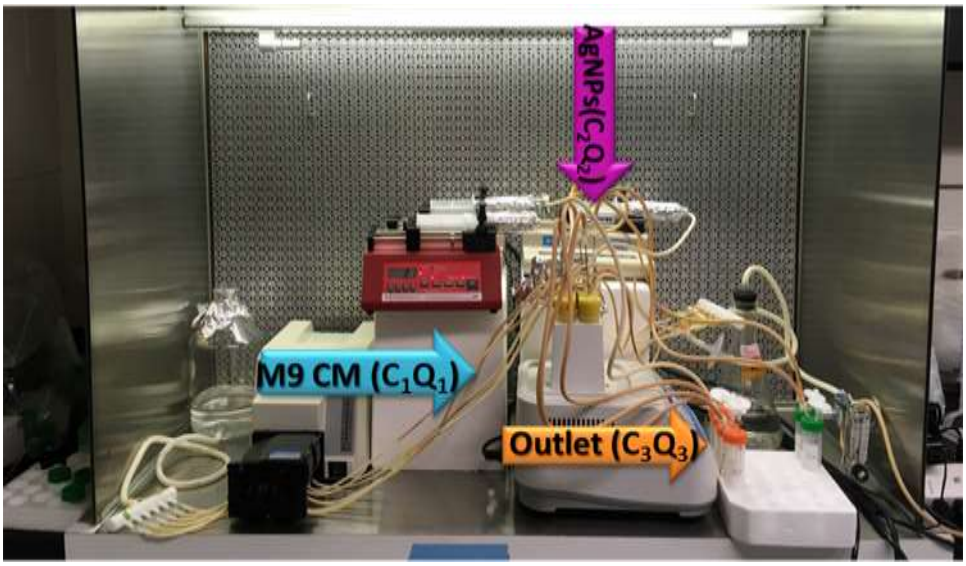

Figure S4. Continues culture of *E.coli* K-12 with continues injection of AgNPs

Through continuous injection, AgNPs concertation inside the reactor was kept at constant value from time of injection to the end of experiment, allowing us to make consistent comparisons at multiple exposure times. Samples were collected at 4 hours intervals from bioreactors. After centrifugation for 20 minutes at 6000 rpm, the supernatant that includes ES and AgNPs were separated from bacteria. Then, the ES and AgNPs solution were used for measuring the particle hydrodynamic diameter size distribution and zeta potential (ζ) of the suspensions as well as measuring AgNPs and silver ions concentrations.

1.5. Testing designed primers for transcriptomic analysis

To ensure that the primer dimer would not be formed, multiple primer pairs were analyzed for the possibility of primer dimer formation. We ordered the primer pairs which showed the lowest possibility to form self and/or hetero dimers. Next, a series of dilutions for the cDNA template was tested for qPCR efficiency and the melting

curves were carefully analyzed. Since, there was only a single melting point for each primer pair it was established that the amplification was specific and only one target amplicon for each primer pair was being generated. The melting temperatures of the qPCR product ranged from 81.81 °C to 86.84 °C. The primer dimer formation was ruled out by the absence of melting point at temperature between 65 °C and 70 °C. Furthermore, we used $\Delta\Delta C_T$ method for gene regulation calculation. First, for both control bioreactors and AgNPs-exposed bioreactors, we determined the ΔC_T by subtracting the mean C_T value of each gene from mean C_T value of housekeeping gene (*rrsB*). Then, in order to calculate the $\Delta\Delta C_T$ we subtracted the ΔC_T of genes at control bioreactors from the ΔC_T of genes at AgNPs-exposed bioreactors. Finally, the regulation of each gene (R) is obtained by $2^{-\Delta\Delta CT}$

Table S4. Primers of target genes

Target genes	Forward Primer	Reverse Primer
cpsB	GTT GGC TCC TGG TCT TCA TTA	CAG GCC AGA TTC AGC ATA CA
copA	CGA TCC GTT GCG TAG TGA TAG	CCT CAT CAA TCC CTG CTT CTT
CueO	TGC TGC ATC CGT TCC ATA TC	CAC TTC GCT GAC ATT ACC TTC T
CusA	GAC GCC ACG CTG GAT AAT AA	CAG GGT GAA GAT CGG GAT AAA C
fabR	ATG GTT GAT GAG AGC GGT TTA	CCG GAA GGC GTT AGG ATT ATT
ompF	CGC TAC GCC GAT CAC TAA TAA	ACC AGA TCA ACA TCA CCG ATA C
rrsB	GTC AGC TCG TGT TGT GAA ATG	CCC ACC TTC CTC CAG TTT ATC
soxS	ATC AGA CGC TTG GCG ATT AC	GAG ACA TAA CCC AGG TCC ATT G
zwf	CCA AGC TGG ATC TGA GCT ATT C	ACC CAT TTC CAG GCT TCT TC

1.6. ROS generation measurement using 2',7' –dichlorofluorescin diacetate (DCFH-DA)

First, $2x10^5$ cells/well were cultured in a 96-well black plate. After washing the cells with buffer 1X, supernatant in the microplate was replaced with DCFH-A (10 μM) and incubated for 1 hour at 37 °C. Finally, cells were washed with buffer 1X and exposed with given concentration of AgNPs. Procedures were performed in the dark. Each 96-well microplate consists of blanks (AgNPs 1 mg/L and 10 mg/L), AgNPs exposed bacteria, and control bacteria. The blanks absorbance were subtracted from AgNPs exposed bacteria, allowing us to make consistent comparison with control bacteria.

2. Additional Results

2.1. AgNPs concentration inside of the continuous culture

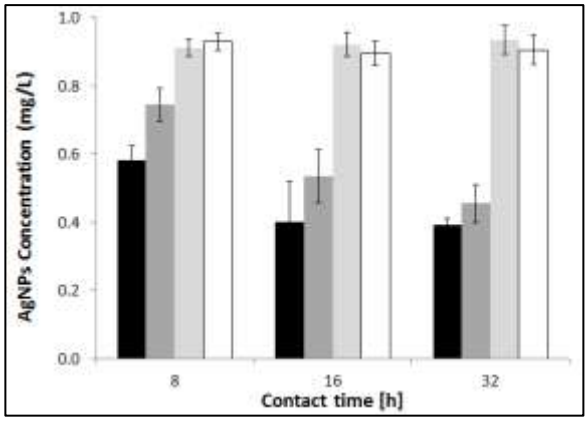

Figure S5. Changes of the AgNPs concentration inside of the continuous culture for both specific growth rates are displayed after 8, 16, and 32 hours after AgNPs injection. Black bars represent 0.1 h^{-1} and dark grey bars represent 0.2 h^{-1} for exposed bacteria. Light grey bars represent control reactors at 0.1 h^{-1}. White bars represent control reactors at 0.2 h^{-1}. For control reactors M9 minimal medium plus AgNPs were used. Error bars represent the error between three technical replicates from duplicate bioreactors.

2.2. Dissolution rate of nanoparticles in continuous bioreactors

Dissolution experiments consisted of measuring the concentration of Ag ion released in ES from both growth rates. Ag ions release was quantified for ES with AgNPs (from continuous bioreactors), M9 minimal medium, and distilled water (control) (Figure S6). The initial concentration of Ag ions released in DI water was 0.031 ± 0.005 mg/L but over time after 12 hours, the released ion concentration increased to 0.08 ± 0.006 of the total silver concentration (1 mg/L). In contrast, initial ion released in M9 minimal culture media slightly increased over 12 hours of contact. The effect of ES from both specific growth rates on the initial Ag ion release was not detectable for

both 0.1 h^{-1} and 0.2 h^{-1}, although, after 12 hours of exposure the concentration of ions released in ES of 0.1 h^{-1} and 0.2 h^{-1} were almost the same (Figure S6). The low rate of AgNPs dissolution in M9 minimal culture media and ES clarified that bacteria that responded to the inhibitory effect of AgNPs were not correlated with ions released by the nanoparticles and their interference in the cellular metabolic pathways.

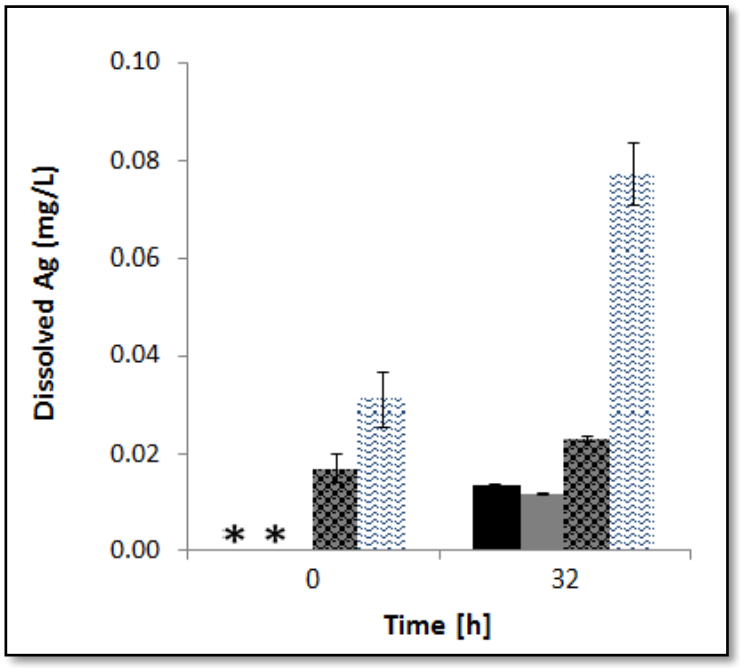

Figure S6. Ag ions released from AgNPs at concentrations of 1 mg/L DI water, M9 minimal media, ES from EB-0.1, and ES from EB-0.2 at time zero and after 32 hour contact time at 37 °C. Wave patterns represent AgNPs suspended in DI water, sphere patterns show AgNPs suspended in fresh M9 minimal media, and grey filled represent AgNPs exposed to ES from EB-0.2 and black filled correspond to AgNPs suspended in from EB-0.1. Star sign means that Ag ion concentrations were not detectable. Samples run in triplicate.

2.3. AgNPs stability and hydrodynamic diameter size distribution

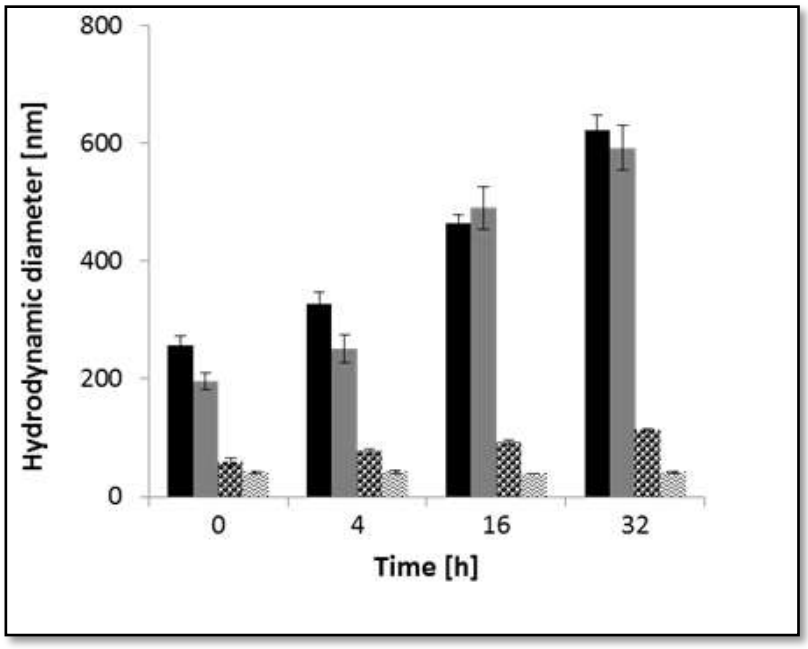

Figure S7. AgNPs stability in DI water, M9 minimal media, ES from EB-0.1, and ES from EB-0.2 after 32 hours of exposure. Wave patterns represent Ag suspended in DI water, sphere patterns show AgNPs suspended in fresh M9 minimal media, and grey filled represent AgNPs in ES from EB-0.2 and black filled correspond to AgNPs suspended in ES from EB-0.1. Samples run in triplicate.

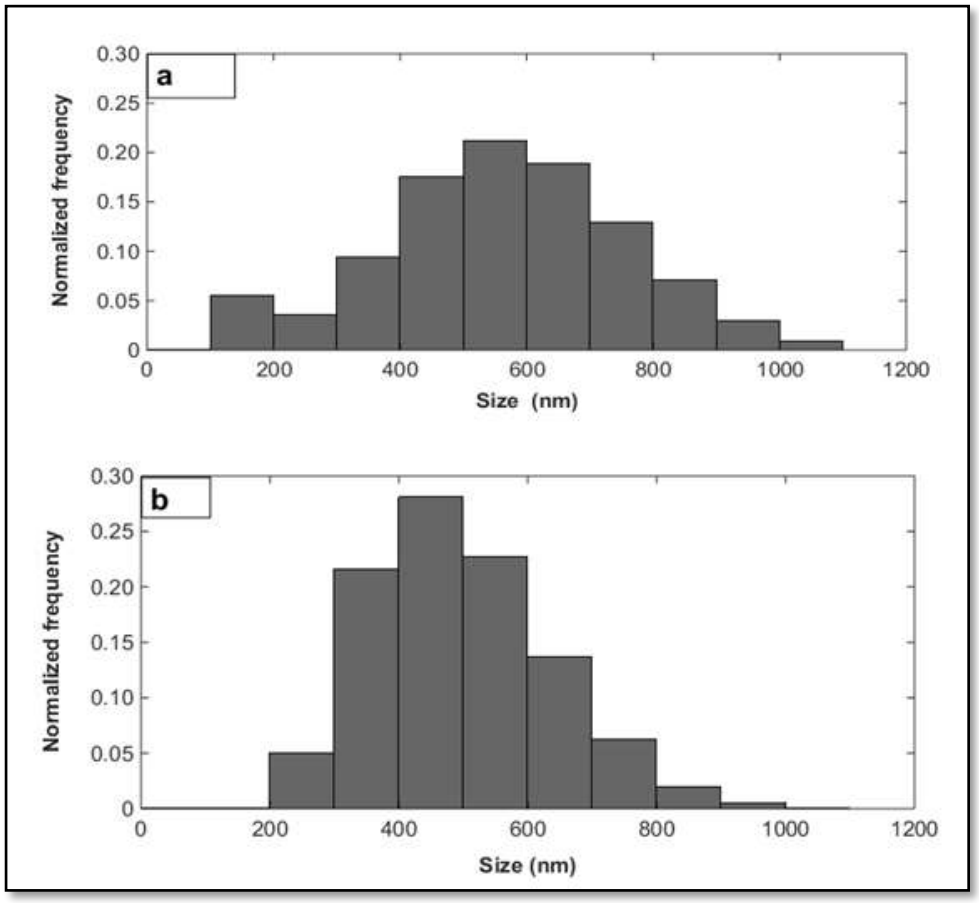

Figure S8. AgNPs size distribution in ES of continuous bioreactor products. (a) AgNPs in ES at EB-0.1 and (b) AgNPs in ES at EB-0.2 h both after 32 hours of contact time.

2.4. AgNPs zeta potential

Table S5. Zeta potential characterization of AgNPs suspension in different solutions.

Suspensions	AgNPs Zeta Potential (mV)
DI water + AgNPs	-26 ± 1.53
M9 minimal media + AgNPs	-22 ± 1.12
AgNPs at ES from EB-0.1	-11 ± 1.23
AgNPs at ES from EB-0.2	-14 ± 1.34

2.5. ES concentration and characteristic at different specific growth rates

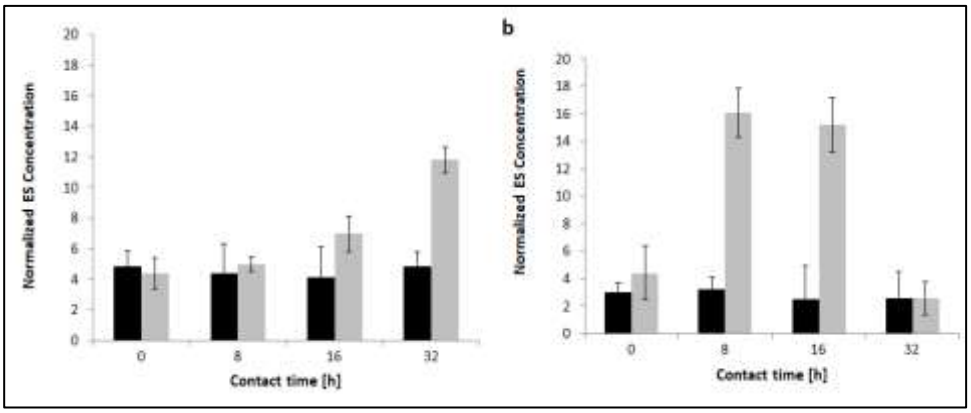

Figure S9. ES concentration normalized to OD600 at different contact times, zero contact time means before the starting injection, 8, 16, and 32 represents the time in hours of contact between nanoparticles and bacteria inside continuous culture at two specific growth rates. (a) Normalized ES concentration at 0.1 h^{-1} and (b) Normalized ES concentration at 0.2 h^{-1}. Black and grey marks show the ES from CB and ES from EB, respectively. Bars represent the error between three technical replicate from two replicates.

ES can affect the inhibitory effectiveness of AgNPs through two mechanisms; physiochemical alteration of nanoparticles' surface modifications and nanoparticles'

immobilization in ES matrix.[7] In here, it was considered the heterogeneity between the compositions of ES at different specific growth rates (Figure S10). Therefore, after characterization of ES compositions by ATR-FTIR,[8] variation of ES composition among the tested conditions was assessed using HCA.[9]

ATR-FTIR spectra which looked at a comparison of the ES before and after reaction with AgNPs demonstrated changes in the organic moieties and functional groups of the ES. For the ES at 0.1 h^{-1}, the band around 1640 cm^{-1} is ascribed to C=O stretching (amide I), which completely disappeared in ES of 0.2 h^{-1}. Also, the band at 1550 cm^{-1} is ascribed to the N-H bending and C-N stretching (amide II) in peptides vanished in ES of 0.2 h^{-1}. The bands near 1046 cm^{-1} are assigned to the stretching vibration of C-O-C in sugar derivatives after AgNPs exposure shifted to 1060 cm^{-1} at 0.1 h^{-1} and 1070 cm^{-1} at 0.2 h^{-1} due to carbohydrate backbones. These results assessed that the ES contains mainly protein, saccharides, and carboxylates. These findings are in agreement with Wang *et al*.[7] They reported the weakness of bands related to amide II and carboxylic acids after reaction with zinc oxide nanoparticles in ES. Furthermore, the band corresponding to the C-O-C group of sugar derivatives (1046 cm^{-1}) becomes shifted in ES after AgNPs exposure, implying the possibility of trivial reducing sugar adsorbing these nanoparticles.

In this study, HCA was based on the baseline-normalized spectra of all ES obtained from continuous culture. HCA results for the pairwise analysis of the fingerprint (1800-900 cm^{-1}) region of ES released from bacteria without and with nanoparticles are shown in Figure S10. ES extracted from 0.1 h^{-1} segregated distinctly from the ES from control groups of 0.2 h^{-1}. Higher heterogeneity values in the dendogram was

obtained in ES from 0.2 h^{-1} compared to 0.1 h^{-1}, which indicates that the composition of ES released by CB-0.1 during their time spent in the continuous culture/during nanoparticle exposure were more stable than those obtained from CB-0.2. Moreover, the heterogeneity between ES from EB-0.2 showed the higher similarity to ES composition of other samples (ES from CB-0.1 and ES from EB-0.1). Generally, in the control group ES concentration and composition was function of growth rate. In addition, ES from AgNPs exposed bacteria changed in composition at the higher growth rate condition and obtained similar compositions to ES from exposed bacteria at low growth rate condition.

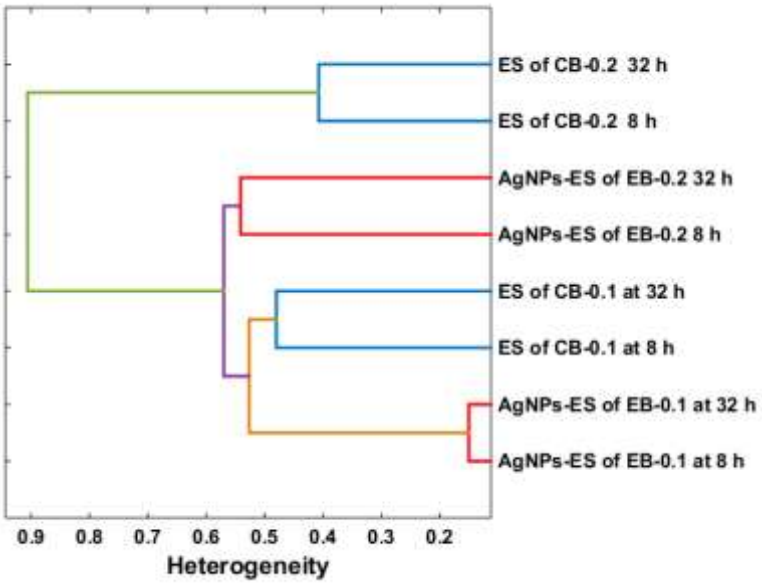

Figure S10. Hierarchical cluster analysis of the ES composition from control bacteria (CB) and ES from AgNPs-exposed bacteria (EB) at two different specific growth rates during 8 hours and 32 hours of contact time. Blue line represents only time impacts on compositional differences between ES of control bacteria (CB). Red line shows heterogeneity between the AgNPs-ES samples from AgNPs-exposed bacteria (EB) during different time of treatment with AgNPs. Green line shows dissimilarity between the ES of CB-0.2 and other samples (ES of CB-0.1, AgNPs-ES of EB-0.1, and AgNPs-ES EB-0.2). Purple line represents dissimilarity between ES of CB-0.1 and AgNPs-ES of EB-0.1, and AgNPs-ES of EB-0.2. Orange line shows the heterogeneity between ES of CB-0.1, and AgNPs-ES of EB-0.1.

Results of thermogravimetric analysis (TGA)

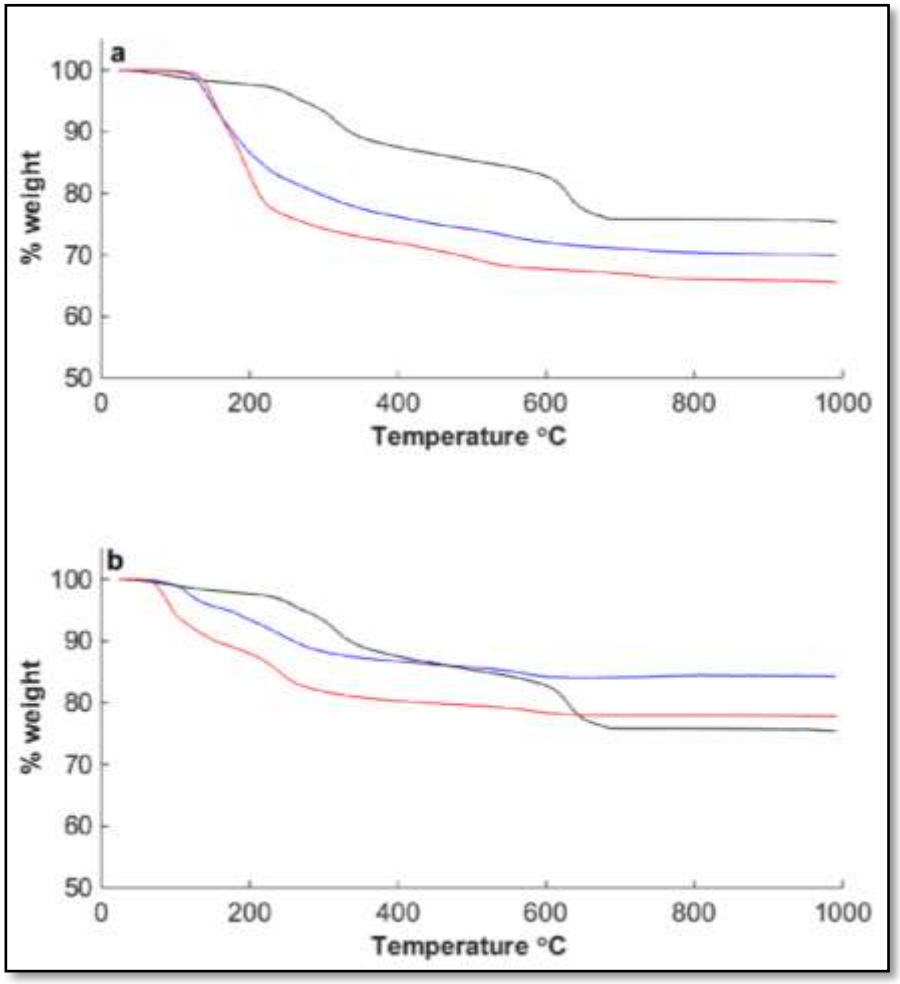

Figure S11. Thermogravimetric analysis (TGA) of ES-AgNPs of the AgNPs-exposed bacteria (EB) and ES of the control bacteria (CB) from different specific growth rates. (a) Thermal stability of AgNPs-ES from EB-0.1 and ES from CB-0.1, (b) thermal stability of AgNPs-ES from EB-0.2 and ES from CB-0.2. Thermal stability of AgNPs-casein was obtained as a reference to compare with interacted AgNPs-ES. Black, blue, and red lines represent TGA of AgNPs, AgNPs-ES, and ES, respectively.

REFERENCES FOR SUPLEMENTARY INFORMATION

1 R. M. Maier, I. Pepper and C. Gerba, *Environ. Microbiol.*, 2000, 43–59.

2 G. Molin, *Eur. J. Appl. Microbiol. Biotechnol.*, 1983, **18**, 303–307.

3 J. Glazyrina, E.-M. Materne, T. Dreher, D. Storm, S. Junne, T. Adams, G. Greller and P. Neubauer, *Microb. Cell Factories*, 2010, **9**, 42.

4 M. O. Tovey and D. Brouty-Boyé, *Exp. Cell Res.*, 1979, **118**, 383–388.

5 Q. Wang, F. Kang, Y. Gao, X. Mao and X. Hu, *Sci. Rep.*, 2016, **6**, 21379.

6 J. Zeng, J.-M. Gao, Y.-P. Chen, P. Yan, Y. Dong, Y. Shen, J.-S. Guo, N. Zeng and P. Zhang, *Sci. Rep.*, 2016, **6**, 26721.

7 R. Gurbanov, N. Simsek Ozek, A. G. Gozen and F. Severcan, *Anal. Chem.*, 2015, **87**, 9653–9661.

MANUSCRIPT – III: COMPARISON OF TWO PULSED LIGHT LAMPS FOR DISINFECTION AND DEGRADATION ORGANIIC COMPOUNDS IN AQUEOUS SOLUTIONS.

In preparation for submission to Water research Journal

Faghihzadeh, F.[1], Anaya, N.M.[1], Hadjeres, H.[2], Boving, T.B.[1,2], Oyanedel-Craver*[1].

[1] Department of Civil and Environmental Engineering, University of Rhode Island, Kingston, RI, 02881, USA.

[2] Department of Geoscience, University of Rhode Island, Kingston, RI, 02881, USA.

*Corresponding Author:

* Corresponding author: Vinka Oyanedel Craver

E-Mail: craver@uri.edu

Phone: (401) 874 2784,

Fax: (401) 874 2786

Abstract

This study explores the impacts of pulsed light (PL) on cellular compartments of *Escherichia coli* MG1655 as well as degradation of polycyclic aromatic hydrocarbons. The samples were exposed to high intensity (1.27 joule/cm^2/pulse) and short pulses (360 μs) generated by ultraviolet (UV) light. Two types of spiral UV lamps were used, one with 190 nm cut-off (PL1), the other with 240 nm cut-off (PL2). The PL1 results showed statistically significant (p = 6.81E-07) impact on bacterial membrane disturbance and remaining respiration. Irradiation with PL2 lamp had a much lower impact (p = 0.0062). We studied *E. coli* regrowth after irradiation and found that the lag phase duration increased 20% and growth rate decreased 29% after exposure to PL1 compared to PL2. In addition, hieratical cluster analysis between the cellular compartments of regrowth of exposed bacteria and exposed bacteria showed maximum distinct segregation between regrowth of exposed to PL2 bacteria and exposed to PL2 bacteria on the carbohydrates region. Regarding PAHs degradation, all of the four target compounds (naphthalene, fluorene, pyrene, and anthracene) degraded 100% after 15 seconds of exposure to either PL1 or PL2. First-order decay kinetics best described the naphthalene and fluorene degradation. The degradation of pyrene and anthracene, regardless of exposure to PL1 and PL2, were better explained with second order kinetics.

Keywords: Pulsed light with or without ozone, polycyclic aromatic hydrocarbons, *Escherichia coli* MG1655, cellular components, Kinetic decay order.

1. Introduction

Ultraviolet light treatment, continuous (CUV) and pulsed (PL), are none-thermal

treatment techniques for aqueous solutions containing microbial and organic contaminants, such as *E. coli* and polycyclic aromatic hydrocarbons (PAH) [1–4]. Compared with CUV, PL has showed higher inactivation of microorganisms and degradation of PAHs, because of it rich and broad-spectrum UV content, high energy peaks and predictable treatment outcomes[4]. Typical PL lamps produce high intensity light pulses in a wavelength spectrum between 100 to 1100 nm. For water treatment purposes, short pulses (100-400 μs) in the wavelength range below 400 nm are commonly applied [1,5].

In terms of microbial disinfection, several studies have shown that PL produce DNA damage[3–9]. High intensity light pulses of PL cause thymine dimerization in the DNA chain and prevent replication[4]. Kramer and Muranyi[5] reported that with fluence up to 0.27 joule/cm^2, only about 80% of DNA was formed relative to the non-exposed cells. They also reported that observed colony count reduction after exposure to PL in *L. innocua* is directly corresponded to the occurrence of DNA low quantity[5].

DNA damage have been reported as the main mechanism, however other studies have showed the high complexity of the microbial response to PL to be a multi-target inactivation process[8,9]. Transcriptomic analysis have shown that several stress related proteins upregulated in PL exposed cells, implying an increase in transcriptional and translational processes in response to PL[6]. Other reported effect are increase of bacterial mutation frequency as well as changes in the abundance of 19 proteins as revealed by a global proteome analysis[6] and whole genome DNA microarray analysis[7].

The effect of PL on cellular components and metabolic cell activity[6–8] have been described while other studies documented structural damages to the cell membrane or cell wall after PL exposure[11–14]. For instance, structural cell damage has been observed by propidium iodide uptake[11,12], protein or other cellular component leakage[12, 13], as well membrane shrinkage[13]. Effects of metabolic activities and cellular dysfunctions, low glucose uptake[6,7] activity, and reduction of esterase activity[12,15] were reported [6,7] as well as less cultivability and more cellular damage on respiration, enzyme activity, and membranes[7]. Kramer and Muranyi also assessed less cultivability and more cellular damage on respiration, enzyme activity, and membrane[5]. On the other hand, Garvey *et al.*[14] suggested that PL exposed cells are viable but non-culturable and that colony count reduction cannot be directly linked to membrane disruptions. There are incomplete understandings among previous reports that need to comprehensively investigate including the PL impacts on bacterial inactivation and bacterial cellular components. In addition, any direct effects of PL on cellular biomolecules, such carbohydrates, nucleic acids, proteins and fatty acids, were not investigated. To the best of our knowledge, detecting the heterogeneity between the cellular components (nucleic acids, carbohydrates, proteins, and fatty acids) of PL exposed bacteria and regrowth of PL exposed bacteria have not been reported.

It is well known that UV light photolyases PAHs[3,4,16,17]. Rates of photolysis generally decrease with decreasing PAH molecular weights[17]. At wavelengths present in sunlight, higher molecular weight PAHs, such as pyrene, possess higher reactivity because of their higher extinction coefficients[16]. There is evidence for phenanthrene

degradation when irradiated with PL[18], but the effect of PL on other PAHs remains unclear[18].

The impetus for this study was two-fold: (1) to explore the impacts of pulsed light (PL) on *Escherichia coli* MG1655 in terms of membrane disruption, impact on bacterial respiration, membrane permeation, regrowth lag phase duration and the biomolecular alterations of fatty acids, protein, carbohydrates, and nuclei acids, (2) degradation kinetics of polycyclic aromatic hydrocarbons by PL. We consider the results of this study of interest to water treatment professionals seeking an alternative to conventional water disinfection and treatment technologies.

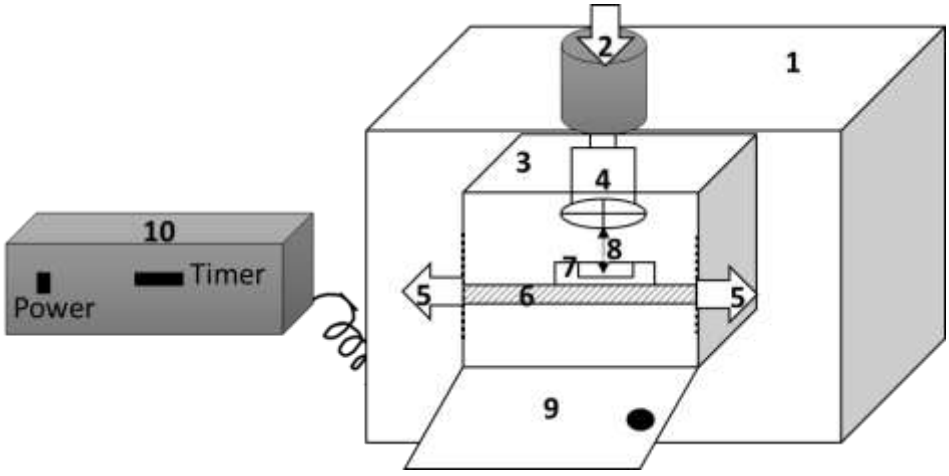

Fig. 14 Schematic of laboratory scale pulsed light SteriPulse®-RS 4000 system (XENON Corporation, Wilmington, MA) unit. This system includes; 1)pulsed light sterilization system, 2)air, 3)pulsed light chamber, 4)Xenon spiral lamp, 5)quartz glass, 6)chamber tray, 7)Teflon plate, 8)the distance between lap and sample, 9)chamber door, 10)controller.

2. Materials and Methods

2.1. Materials

A non-pathogenic strain of *Escherichia coli K-12 strain MG1655* (*E. coli)* was selected for this study, because is a Gram-negative bacterium extensively used in disinfection studies[19,20]. Reagents used to prepare the lysogeny broth (LB) Miller growth were purchased from Fisher Scientific. The bacteria were stored in a phosphate buffer solution (PBS) consisting of—and ethylenediaminetetraacetic acid (EDTA), which were purchased from Sigma Aldrich. SYTO 9 and propidium iodide used for cell membrane permeation were purchased from Invitrogen. Tetrazolium dye (Redox Dye Mix A) was purchased from Biolog and used to measure the respiratory activity of *E. coli*. The cell culture 96-well flat bottom plates were purchased from Corning Costar Co. The mFC Fecal Broth for cultivation and colony enumeration was purchased from Fisher Scientific. Synergy TM MX microplate reader (BIOTEK, VT) was used for the spectrophotometric and fluorescence analysis. Optical density as OD600 nm was measured by using a UV Vis-spectrophotometer (Genesis, 10UV, Thermo Scientific).

Two types of spiral XENON UV lamps were tested (XENON Corporation, Wilmington, MA), one with 190 nm cut-off (PL1), the other with 240 nm cut-off (PL2). The PL1 lamp produced Ozone (O_3) from ambient oxygen[21], whereas PL2 does not. Other lamp characteristics are summarized in Table 4. Both lamps are low-pressurized and mercury free.

The lamps were installed in a laboratory scale SteriPulse®-RS 4000 system (XENON Corporation, Wilmington, MA) (Fig. 14). Bacteria and PAH samples were contained in two types of circular Teflon® trays. For the bacterial inactivation test, the tray was 3 cm diameters and 0.5 cm depth (Vol.: 3 mL). For the PAH experiments, the tray diameter and depth was 5.0 and 0.8 cm, respectively (Vol.: 30 mL). Two different volume plates were used to avoid cross contamination between bacteria and PAHs samples and volume requirements for downstream analysis. After the UV exposure, the 30 mL of PAHs were concentrated in 2 mL for follow extraction. On the other hand, 3 mL of bacteria aliquot were enough for further analysis.

Table 4. Characteristics of the PL1 and PL2 lamps

Lamp	Spectral cut off (nm)	Pulse energy (joule/pulse)	Intensity (joule/cm^2/pulse)	Curing area
PL1	190	15	1.27	Circular 5.5" diameter
PL2	240	13	1.27	Circular 5.5" diameter

The decay kinetics of three low molecular weight PAHs: naphthalene ($C_{10}H_8$), fluorene ($C_{13}H_{10}$), and anthracene ($C_{14}H_{10}$) were compared to pyrene ($C_{16}H_{10}$), a high molecular weight PAH. All PHA were purchased from Sigma Aldrich (Purity grade: 99% or higher). Deuterated PAHs mixtures were purchased from Ultra Scientific. Analytical grade solvents, including methanol and dimethyl sulfoxide (DMSO), dichloromethane (DCM) were purchased from Fisher Science. PAH standards were obtained from Ultra Scientific.

2.2. Methods

2.2.1. Bacterial culture

For each experiment, fresh *E. coli* cultures were grown for 12 hours in sterilized LB media at 37 °C [22]. The pH of the medium was adjusted to 7.2. After that cell were harvested by centrifugation and the solutions containing the desire concentration of bacteria were prepared using the PBS [23]. PBS was used to maintain the constant pH and prevent denaturation and conformational changes.

2.2.2. Determination of operational conditions of PL1 and PL2 on *E. coli* K-12

After determining the most effective fluences for PL1 and PL2, for reduction of culturable bacteria and membrane permeation, 76 joule/cm2 for PL1 and 95 joule/cm2 for PL2 were chosen to study the PL1 and PL2 disinfection mechanisms on bacteria. 3 mL of high concentration bacteria (OD600 = 1.2) was considered due to requirement of respirometric test and fourier transform infrared spectroscopy (FTIR) analysis to high concentration of bacteria. After exposure to PL1 and PL2 downstream analysis including respirometric test, membrane permeability analysis, cultivation and enumeration, and determination of specific growth rates and their lag phase duration of regrowth bacteria were performed. Finally, FTIR analysis was performed to determine qualitatively the composition of controls and resultant after disinfection, then, hieratical clustering analysis (HCA) of FTIR data was applied to determine the heterogeneity of bacterial various biomolecular groups such as fatty acids, proteins and nucleic acids between exposed, non-exposed, regrowth of exposed, and regrowth of non-exposed bacteria. The comparison was mainly based on exposed and regrowth

of exposed to non-exposed, but regrowth of non-exposed was also added to verify its similarity to non-exposed and to consider possible effects of compositional differences due to bacterial regrowth.

2.2.3. Culturability

In order to compare between the culturability of PL1 exposed bacteria and PL2 exposed bacteria, two tests such as colony forming and bath growth were performed.

2.2.3.1. Colony forming

Four dilutions (1.00E+03, 1.00E+06, 1.00E+09, and 1.00E+12) of PL1 and PL2 exposed bacteria, and non-exposed bacteria were prepared in PBS. Then, after the filtration, samples were incubated in mFC fecal broth media at 42 °C for 24 hours. The log removal of bacteria were obtained for PL1 and PL2 through counting the number of colony forming unit (CFU) based on previous study[24].

2.2.3.2. Batch growth

10 µL of PL1 and PL2 exposed bacteria were regrown in 5 mL of LB media at 37 °C in a six well microplate. Absorbance at 600 nm was recorded every 0.25 hour for 18 hours. The slope of the log phase showed the specific growth rates of the bacteria. The control and blank were non-exposed bacteria and LB media, respectively. Experiment was run in two 6 well microplate and each microplate contains duplicates of each condition. Afterwards, samples from each well were collected for FTIR analysis.

2.2.4. Respirometric test

Cell respiration was quantified in non-growing conditions of PL1 and PL2 exposed bacteria and non-exposed bacteria to compare their metabolic activity of electron

transports by tetrazolium dye. Non-growing condition was selected for metabolic activity detection in order to determine only the respiration of bacteria and avoid growth, since, bacteria are not able to grow in PBS. The remaining respiration rate were determined using previously reported protocols [25]. In brief, 96-well microplate was prepared in final volume of 100 µL in each well. Then the following list added respectively; glucose [80 mg/L], tetrazolium dye, PL exposed bacteria solution and each well was mixed thoroughly by pipetting at least 10 times. Controls and blanks were respectively non-exposed bacteria and only PBS instead of bacterial solution. The experiment was run in two microplates and each microplate contains triplicate of each condition. A Microplate reader recorded the absorbance every 0.25 hour for 12 hours. The percentages of remaining respiration (PRR) of the bacteria exposed to PL1 and PL2 were compared by dividing the slope value rates of PL2 exposed bacteria and PL1 exposed bacteria with the slope values of the non-exposed bacteria only first 4 hours was considered (Equation 3).

$$RRP = (P_t/P_c) \times 100 \qquad \text{Equation 3}$$

Where, P_t is the slope from the absorbance–time graph for PL exposed bacteria and P_c is the slope from the absorbance–time graph for non-exposed bacteria (control).

2.2.5. Epifluorescence staining membrane permeability analysis

A membrane permeability test was also performed for the PL1 and PL2 exposed bacteria to compare the membrane permeability with non-exposed bacteria. The cell membrane permeation of PL1 and PL2 exposed *E. coli* was quantified by propidium iodide and SYTO 9 dyes in a microplate reader based on previous report with slight

modifications[22]. A calibration curve of live and dead bacteria was prepared to quantify and compare the membrane disruption on bacteria before and after PL exposure. Each plate contained triplicate wells for each condition to quantify the disturbed cell membrane. The green/red fluorescence ratio between the PL exposed bacteria and non-exposed bacteria were calculated. Undisturbed cell membrane percent (UCM) obtained by Equation 4.

$$\boldsymbol{UCM = (P_t/P_c) \times 100} \qquad \text{Equation 4}$$

Where, P_t is green/red fluorescence ratio for PL exposed bacteria and P_c is green/red fluorescence ratio for non-exposed bacteria (control)

2.2.6. Fourier transform infrared spectroscopy (FTIR) analysis

Bacterial compositions from PL1 and PL2 exposed, non-exposed, regrowth of PL1 and PL2 exposed, and regrowth of non-exposed conditions were characterized by directly placing specimens on the crystal surface for attenuated total reflection (ATR) mode of FTIR (Nicolet iS50 FTIR, Thermo Scientific) in the 3300-600 cm^{-1} spectral range same as previously reported protocol[26]. The software for the data providing was Omnic software (Thermo Scientific) and for data processing was MATLAB (MathWorks Software).

The heterogeneity of bacterial various biomolecular groups such as fatty acids, proteins, and nucleic acids between exposed, non-exposed, regrowth of exposed, and regrowth of non-exposed bacteria were determined by HCA[27]. For HCA, a data set was collected from the pair-wise similarity coefficients of all spectra as a matrix of correlation coefficients, which contains the total number of spectra (N entries).[28] Between two spectra, each correlation coefficient can range from 0.0 for totally

different spectra to 1.0 for identical spectra. The similar spectra were obtained by recalculation of the correlation matrix. Then, the identical spectra were merged into a new object, and the merging process repeated until all spectra were combined into a small number of clusters.

2.2.7. Degradation of aqueous phase PAH

Stock solutions of PAHs were produced by mixing reagent-grade, powder forms of the model PAHs with methanol (1 mg/L) and stirred for 24 hours in the dark. PAHs sample aliquots were prepared by transferring 10 mL of the stock solution to 1 L of distilled water and stirred for another 24 hours in the dark. Then, 20 ml of PAHs sample aliquots were added to Teflon plates and were exposed to PL1 and PL2 for a range between 0 to 190 fluences (joule/cm^2). Controls were run for each condition and consisted of non-exposed PAHs which placed on the chamber uncovered and without turning on the PL. Dichloromethane (DCM) was considered as blank Blanks for analyzed for quality control purposes.

After exposure, a 30 µL of deuterated PAH mixture with a individual PAH concentration of 50 mg/L was added to the samples as an internal standard. Then, 2 mL of dichloromethane (DCM) was added to the samples and mixed completely through agitation for 1 min. After 2 min of settling time, the DCM phase containing the PAH (1 mL) was extracted and analyzed by the GC-MS (QP2010S, Shimadzu).

2.2.7.1. PAHs Degradation Kinetics

The degradation of PAHs following PL1 and PL2 exposure were modeled as first and second order decays on Equation 5 and Equation 6.

First-order decay constant (α)= $\frac{\ln\left(\frac{c_0}{c_t}\right)}{t}$ Equation 5

Second-order decay constant (α)= $\frac{1}{tc_t}$ Equation 6

where α is the decay rate coefficient, C_0 is the initial concentration of PAHs, C_t is the concentration of PAHs at time t.

2.2.8. Toxicity of degraded PAH solution

For respiration test of the exposed PAHs on *E. coli*, the remaining respiration was quantified in the same conditions that mentioned above. The only difference was measuring the respiration of *E. coli* in presence of the PL1 and PL2 exposed PAHs. Previously exposed PAHs from three different fluences (0, 19, 190 joule/cm^2) were selected to follow the effects of the PAHs and byproducts of exposed PAHs on bacterial respiration. Table S1 in the SI contains the used PAHs concentration in this test.

3. Results and Discussions

3.1. Disinfection mechanisms of PL1 and PL2 on E. coli K-12

Initially we performed the kinetic study of bacterial exposure to several fluences including 0, 19, 38, 57, 76, 95, 190 joule/cm^2 using both lamps. Then, we selected 76 joule/cm^2 for PL1 and 95 joule/cm^2 for PL2, based on the kinetic study of colony forming test and membrane permeation results (Figure S1 in the SI).

3.1.1. Culturability of PL1 and PL2 exposed *E. coli K-12*

The influence of PL1 and PL2 on culturability of exposed and regrowth bacteria were determined by different analysis. These analyses include membrane filtration

(capability of to form colonies), as well as growth rate determination and lag phase duration from regrowth of exposed bacteria.

3.1.1.1. Colony forming units

PL1 treatment with fluence of 76 joule/cm^2 and PL2 with 95 joule/cm^2 were shown to be enough bacterial removal as shown the log removal for each case (Figure S1). Fig. 15 shows the reduction in the bacterial colonies in PL1 and PL2 by demonstrating reduction of colony forming unit in terms of log removal. The log removal obtained by the $\log_{10}$ of divided non-exposed bacteria to PL exposed bacteria. The reduction of colony forming unit of cultivation and enumeration for PL1 and PL2 exposed bacteria was in agreement with those obtained by other studies. PL has been reported to result in a 0.5 to 8 $\log_{10}$ [2–5] reduction of colony forming unit. The differences between the PL1 and PL2 lamps in reduction of colony forming unit related to the ozone diffusion in the PL1 by oxidation of the lipid bi-layer of bacterial membrane[15].

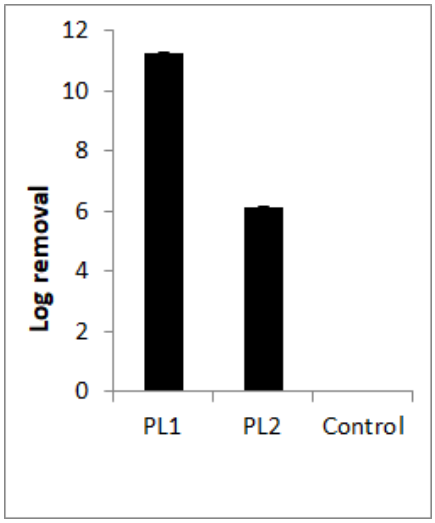

Fig. 15 Log reduction of colony forming units after treatment with of PL1 and PL2. Control was the non-exposed bacteria, hence no colony unite reduction occurred. Error bars indicate the standard deviation of triplicate samples.

3.1.1.2. Batch regrowth

Bacterial regrowth showed a longer lag phase and slower growth rate after exposure to PL1 compared with PL2 (Fig. 16). With growth rate for PL1 and PL2 at 0.1 h^{-1} and 0.13 h^{-1}, respectively, versus the no-exposed case at 0.21. However, both a short lag phase and fast growth rate were observed for non-exposed bacteria regrowth. With lag phase for PL1 and PL2 at ~10 hours and ~8 hours compared to non-exposed at ~2 hours. Previous studies describe photoreactivation as an enzymatic DNA-repair mechanism in different microbial species and its occurrence after PL exposure[7,11]. Farrell et al. assessed that 4 h of sunlight illumination of *Candida glabrata* exposed with various fluencies caused a higher recovery up to 1 $\log_{10}$ compared to dark stored samples[11]. Similarly, Kramer et al.[7] reported recovery was increased by up to 2 $\log_{10}$ exactly after *E. coli* or *L. innocua* were exposed to artificial daylight directly. Also, a possible explanation for the differences between culturability of PL1 exposed and PL2

exposed bacteria is ozonation[29]. Ozonzation is the process that ozone combined with UV in the chamber and increases the PL1 disinfection performance.

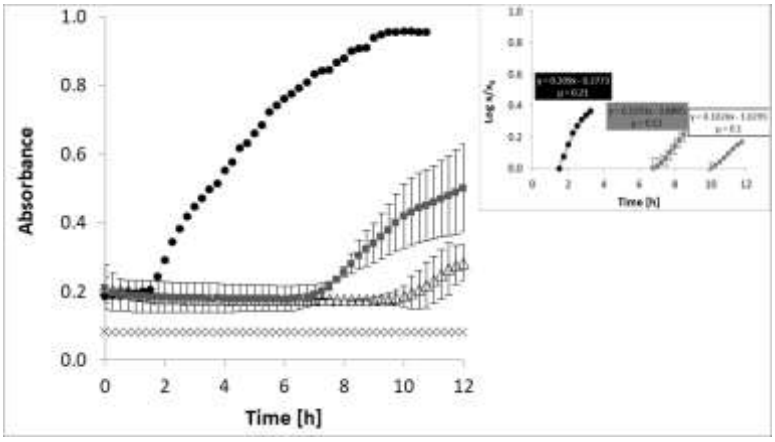

Fig. 16 The absorbance of bacterial regrowth at OD 600 nm. a) Raw data of bacterial regrowth b) linear trend line of slope and regression for regrowth bacteria at different conditions. Marks are: ● controls (non-exposed bacteria), Δ regrowth of PL1 exposed bacteria, ■ regrowth of PL2 exposed bacteria, x blank which is LB media. Error bars are the standard deviation of triplicate samples.

3.1.2. Metabolic activity

Fig. 17 shows a statistically significant PRR difference between the bacteria exposed to both PLs and non-exposed bacteria ($p < 0.05$). Based on previous report metabolic activity is vulnerable to PL than non-exposed cells due to damage to the DNA or other cellular structures like lipids and proteins[7]. The differences in metabolic PRR of the PL1 and PL2 is due to ozone presence in PL1 which first damages the cell membrane, leading to a low metabolic activity and then inhibition of bacterial growth[30].

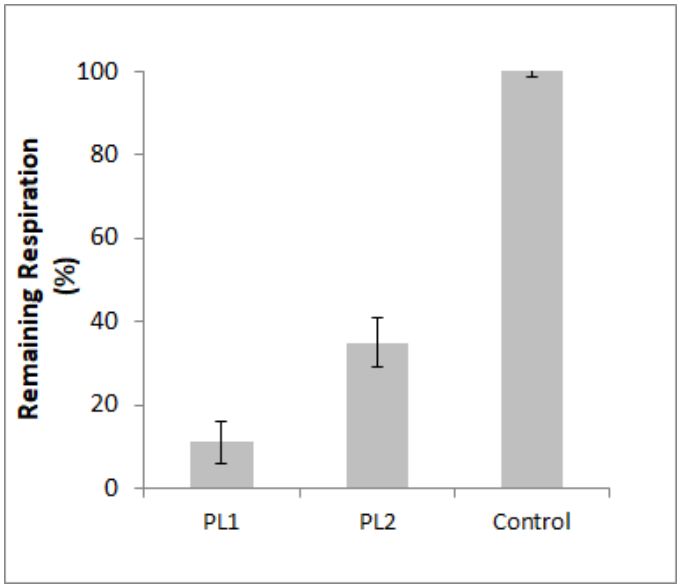

Fig. 17 Impacts of PL1 and PL2 on bacterial remaining respiration percent (RRP). Bacteria exposed to PL2 for 76 joule/cm^2 and bacteria exposed to PL1 for 95 joule/cm^2. Control is non-exposed bacteria. Error bars are the standard deviation of triplicate samples.

3.1.3. Cellular components

3.1.3.1. Membrane permeability

The undisturbed cell membrane (UCM) results (Fig. 18) indicated that the effect of the PL2 on the membrane permeation of bacteria was lower than PL1. The statistical analysis confirmed the disparity of impacts of PL1 and PL2 on bacterial membrane disturbance (p = 6.81E-07). Our finding was in agreement with Krishnamurthy *et al.*[13] report. They demonstrated *S. aureus* cell membrane damage, cytoplasmic membrane shrinkage, and cellular content leakage after PL exposure[13]. Otherwise, Ferrario *et al.*[12] found that PL provoked rupture of the *S. cerevisiae* membrane allowing propidium iodide to penetrate cells as well as progressive loss of esterase activity. However, the significant differences between the PL1 and PL2 effect on the UCM of

exposed bacteria explain by ozone ability to increase the permeability of the cell membrane and causing the efflux of intracellular substances[30].

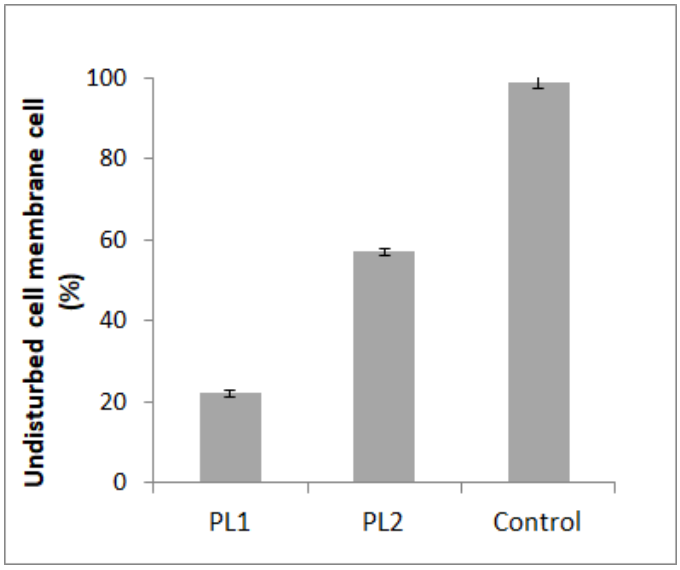

Fig. 18 Impacts of PL1 and PL2 on bacterial membrane permeability that shows undisturbed membrane cell percent. Bacteria exposed to PL2 for 76 joule/cm^2 and bacteria exposed to PL1 for 95 joule/cm^2. Control is non-exposed bacteria. Error bars are the standard deviation of triplicate samples.

3.1.3.2. Cell composition

ATR-FTIR spectra were used to compare the regrowth of PL1 exposed bacteria, PL2 exposed bacteria, and non-exposed bacteria demonstrated changes in the functional groups of bacteria. Comparison of the FTIR results for exposed bacteria and regrowth of exposed bacteria showed significant changes at wavenumbers: biomolecular groups: C=O Stretching, >CH deformation, C=O vibration, and C-O-C vibration for PL1 and PL2. We further investigated each of these wavenumbers in Table 5.

Table 5. Comparison of altrations in biomolecular group between PL exposed and non-exposed bacteria using FTIR.

Biomolecular groups	C=O 1636 cm^{-1}	$>CH_2$ 1454 cm^{-1}	C= O 1235 cm^{-1}	C-O-C 1067 cm^{-1}
Control	1636±2.1 cm^{-1}	1454 ±1.6cm^{-1}	1235±1.4 cm^{-1}	1067±1.1 cm^{-1}
Regrowth control	1636±1.3 cm^{-1}	1453±2.2 cm^{-1}	1235±0.9 cm^{-1}	1068±1.5 cm^{-1}
PL1 exposed	1640±2.8 cm^{-1}	1451±1.1 cm^{-1}	1238±1.4 cm^{-1}	1058 ±1.3cm^{-1}
Regrowth PL1 exposed	1641±3.1 cm^{-1}	1451±0.9 cm^{-1}	1241 ±2.9cm^{-1}	1060±1.1cm^{-1}
PL2 exposed	1639±1.9 cm^{-1}	1467±5.1 cm^{-1}	1232±1.2 cm^{-1}	1085±2.5 cm^{-1}
Regrowth PL2 exposed	1635±0.7 cm^{-1}	1453±1.3cm^{-1}	1237± 2.1cm^{-1}	1069±2.1 cm^{-1}

The vibration of C-O-C in PL exposed bacteria is corresponding carbohydrate backbones and the C-O-C group of sugar derivatives. Hence, the possible explanation for shifting at this region is the possibility of trivial reducing sugar adsorbing[31]. These results assessed that unlike PL2, the negative impacts of PL1 on protein-like amphoteric polymers (N-H and C-N in amide II) and carbonyl groups (C= O) were not compensated by both PL exposed bacteria after regrowth. Also, HCA results in Fig. 19 shows that the carbohydrate region between regrowth of exposed bacteria to PL1 and exposed bacteria to PL1 segregated distinctly. However, HCA and FTIR composition results demonstrated the distinct segregation on the carbohydrates, protein and fatty

acids region between regrowth of PL2 exposed bacteria and PL2 exposed bacteria (Fig. 20). Overall, a higher heterogeneity values in the dendogram were obtained between regrowth of exposed bacteria and exposed bacteria in nucleic acids, carbohydrates and fatty acids regions compared to proteins region. These results indicate that there is more similarity in the protein regions of the regrowth bacteria and exposed bacteria than other cellular components.

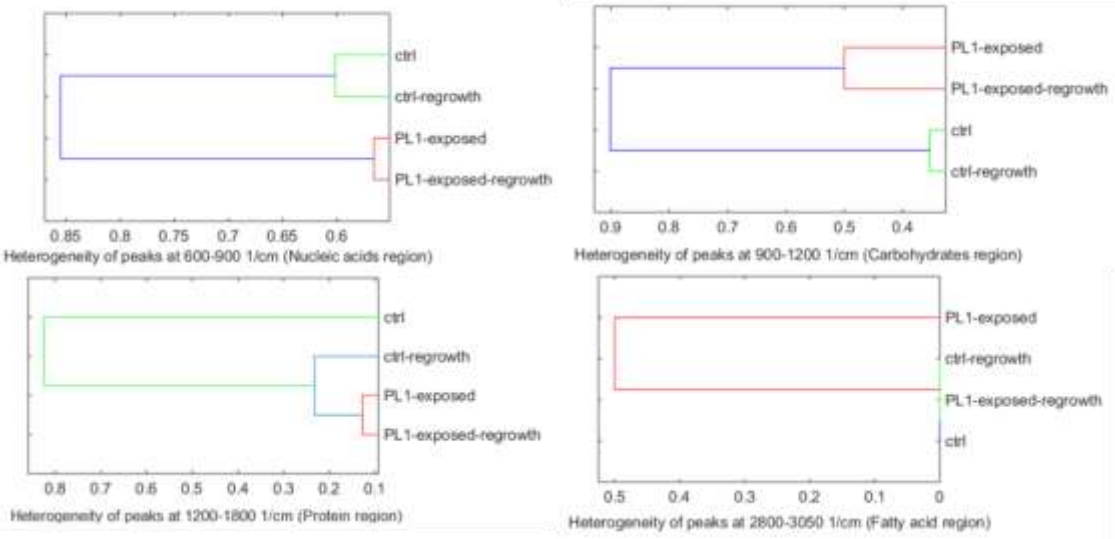

Fig. 19 Hieratical analysis of fatty acids, protein, carbohydrates, and nuclei acids between regrowth bacteria and exposed bacteria to PL1 for 76 joule/cm^2. Control is non-exposed bacteria. Regrowth control is regrowth of non-exposed bacteria.

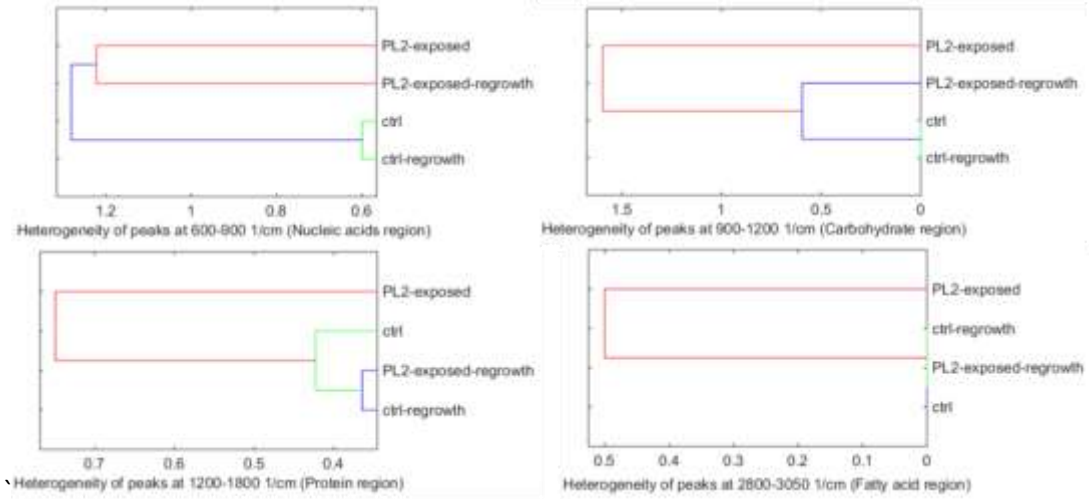

Fig. 20 Hieratical analysis of fatty acids, protein, carbohydrates, and nuclei acids between regrowth bacteria and exposed bacteria to PL2 for 95 joule/cm^2. Control is non-exposed bacteria. Regrowth control is regrowth of non-exposed bacteria.

To summarize the microbial disinfection results, the regrowth of PL1 exposed bacteria are still growing with low specific growth rate and high lag time. On the other hand, our observations corresponding to significant damage on cell membrane permeability of PL1 exposed bacteria (Fig. 18) and lowest heterogeneity of proteins exposed and control groups of bacteria in all conditions (Fig. 19 and Fig. 20) may explain by the Garvey et al., finding which suggested no damage on cell membrane regarding the protein leakage in PL exposed cells[32]. The distinct segregation of carbohydrate region in PL1 exposed bacteria in compare with regrowth of PL1 exposed bacteria indicates that the bacterial respiration process (Fig. 17) had the most disturbance compared to other cellular mechanisms. In this content, the shifting of carbohydrate backbone and significant reduction of PRR might be related to reducing sugar adsorbing[31].

Furthermore, the important similarity between PL1 and PL2 exposed bacteria was the heterogeneity of fatty acids of PL exposed bacteria and regrowth of exposed bacteria which was the same for both lamps. Ferrario et al., assessed that PL agitated rupture of the cytoplasm membrane and progressive loss of esterase activity[12]. These results are in agreement with previous study that cell structural properties such as cellular content leakage, cell membrane damage and cytoplasmic membrane shrinkage occurs after PL exposure[13]. In addition, the comparison between PL1 and PL2 exposed bacteria showed that PL1 has statically higher removal percent than PL2 ($p < 0.05$). The effectiveness of PL1 in bacterial removal may be explained by ozone diffusivity. In this content, Sharrer *et al.* [29] reported that bacteria tend to embed within particulate matter or that form bacterial aggregates that provides shielding from oxidation by UV. They also, pointed out the high CFU reduction when UV irradiation was followed by ozonation (2.5–4.3 $\log_{10}$ reduction)[29]. Thus, combining ozone with a UV irradiation which provided in PL1 consistently reduced bacteria counts to near zero. Also, the comparison of the impacts of these two lamps on cellular components showed that the FTIR composition analysis and HCA results from regrowth of PL1 exposed bacteria lost their similarity to non-exposed bacteria. The possible explanation for this phenomena might be reacting to residual activity and molecular responses[8,33]. However, PL2 exposed bacteria showed ability to regrowth after exposure. Moreover, high heterogeneity between nucleic acids of PL2 exposed bacteria and its regrowth as well as similarity between regrowth of PL2 exposed bacteria and non-exposed bacteria point to the ability of PL2 exposed bacteria to recover itself.

3.2. Kinetic study of PAHs concentration after exposure to PL1and PL2

PAHs rate of destruction tests have been conducted using the ozone generating UV lamp, using the same exposure fluences as for the bacteria (0, 19, 38, 57, 76, 95, 190 joule/cm^2) (Figure S2 in SI). The results of these experiments are displayed in Fig. 21. Results were in agreement with previous studies in terms that high molecular weight PAHs (pyrene) are degradable faster than low molecular weight PAHs (fluorene, naphthalene and anthracene)[17]. Overall, all of the PAHs are removed completely after exposure to 57 joule/cm^2 using the PL1. The pathway of PAHs oxidation in the both PL system can develop according to the structure of individual PAHs.

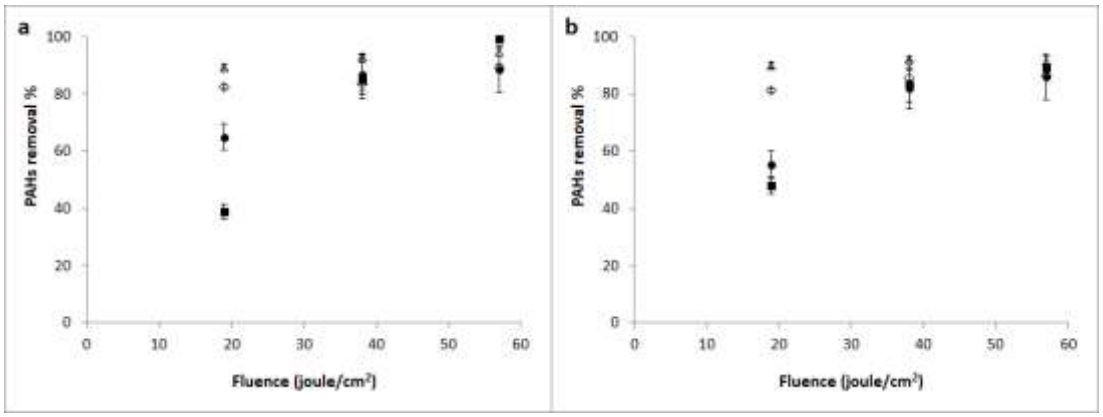

Fig. 21 Kinetic of PAHs removal percentage after inducing to PL1 and PL2 for 57 joule/cm^2. a) PAHs removal percentage during exposure to PL1. b) PAHs removal percentage during exposure to PL2. ● naphthalene. ■ fluorene. Δ pyrene. ◊ anthracene. Error bars indicate standard deviation of triplicates samples.

3.2.1. Removal kinetic order of PAHs concentration after exposure to PL1 and PL2

During PAHs exposure to PL1 and PL2 for 0, 19, 38, 57, 76, 95, 190 joule/cm^2, the decay kinetic orders were investigated by finding the closest linear regression for their degradation constant (Table 6 and Figure S2 in SI).

Table 6. Removal order characteristics of PAHs after exposure to PL1 and PL2.

PAHs	**Fluorene**		**Naphthalene**		**Anthracene**		**Pyrene**	
Parameters	PL1	PL2	PL1	PL2	PL1	PL2	PL1	PL2
Order of decay kinetic	1st	1st	1st	1st	2nd	2nd	2nd	2nd
Decay constant (k)	0.15	0.12	0.12	0.15	175.35	114	168.8	139
R^2	0.95	0.85	0.98	0.99	0.9	0.77	0.96	0.87

Fluorene and naphthalene was positively assigned to first-order decay rate constants (k) for both PL1 and PL2, but, they were negatively correlated with the normalized first-order decay rate constants of pyrene and anthracene. However, regardless of exposure to PL, the removal rates of pyrene and anthracene were better explained with estimation of second order kinetics. Also, no significant differences observed between the degradation rate of the PL1 and PL2. These results oppose Ledakowicz *et al.*[3] study which compared efficiency of three systems (UV, UV with O_3) for PAHs

degradation. The authors recommend UV system in combination with O_3 as the most effective in PAHs degradation processes[3].

3.3. Toxicity of PAHs byproducts on E. coli in term of respiration

The respiration test of the exposed PAHs on *E. coli* showed that the byproduct compounds which were released by the PAHs as a result of exposure to PL1 and PL2 didn't show any toxicity effect on bacteria. Also, the highest bacterial RRP was observed when the high concentration of PL1 exposed PAHs was exposed to bacteria. These results are not conclusive in terms of the toxicity effects of PAHs byproducts after exposure, since the scope of this study didn't include these analyses. (Table S2 in the SI).

4. Conclusion

In summary, PL1 and PL2 treatments have shown its effectiveness in inactivating *E. coli* and degrading PAHs in this study. The results show the potential of PL1 for microbial disinfection and both PLs for the fast degradation of PAHs. However, further testing for daughter PAH products that may be released as byproducts from exposure of the parent PAHs to PL1 and PL2 is needed for optimizing this system. With regard to PAHs, near total degradation was achieved for all four PAHs when working with the SteriPulse®-RS 4000 system and PL1 and PL2 lamps. Moreover, degradation kinetics reflected the molecular weight of the PAHs, with pyrene, a high molecular weight PAH, degrading faster than the other three low molecular weight PAHs.

Acknowledgment

Funding for this project was provided by the Rhode Island Innovation Voucher Program. We are thankful to Xenon corp., Wilmington, MA for technical assistance.

References

1. Uslu, G., Demirci, A. & Regan, J. M. Disinfection of synthetic and real municipal wastewater effluent by flow-through pulsed UV-light treatment system. *J. Water Process Eng.* **10,** 89–97 (2016).
2. Birmpa, A., Vantarakis, A., Paparrodopoulos, S., Whyte, P. & Lyng, J. Efficacy of Three Light Technologies for Reducing Microbial Populations in Liquid Suspensions. *BioMed Research International* (2014). doi:10.1155/2014/673939
3. Wang, T., MacGregor, S. J., Anderson, J. G. & Woolsey, G. A. Pulsed ultra-violet inactivation spectrum of Escherichia coli. *Water Res.* **39,** 2921–2925 (2005).
4. Kramer, B., Wunderlich, J. & Muranyi, P. Impact of pulsed light on cellular activity of Salmonella enterica. - PubMed - NCBI. (2016). Available at: https://www.ncbi.nlm.nih.gov/pubmed/27409040. (Accessed: 19th February 2018)
5. Kramer, B., Wunderlich, J. & Muranyi, P. Pulsed light induced damages in Listeria innocua and Escherichia coli. *J. Appl. Microbiol.* **119,** 999–1010 (2015).
6. Massier, S. *et al.* Effects of a pulsed light-induced stress on Enterococcus faecalis. *J. Appl. Microbiol.* **114,** 186–195 (2013).
7. Uesugi, A. R., Hsu, L. C., Worobo, R. W. & Moraru, C. I. Gene expression analysis for Listeria monocytogenes following exposure to pulsed light and continuous ultraviolet light treatments. *LWT - Food Sci. Technol.* **68,** 579–588 (2016).

8. Rowan, N. J., Valdramidis, V. P. & Gómez-López, V. M. A review of quantitative methods to describe efficacy of pulsed light generated inactivation data that embraces the occurrence of viable but non culturable state microorganisms. *Trends Food Sci. Technol.* **44,** 79–92 (2015).
9. Farrell, H. P., Garvey, M., Cormican, M., Laffey, J. G. & Rowan, N. J. Investigation of critical inter-related factors affecting the efficacy of pulsed light for inactivating clinically relevant bacterial pathogens. *J. Appl. Microbiol.* **108,** 1494–1508 (2010).
10. Ferrario, M., Guerrero, S. & Alzamora, S. M. Study of Pulsed Light-Induced Damage on Saccharomyces cerevisiae in Apple Juice by Flow Cytometry and Transmission Electron Microscopy. *Food Bioprocess Technol.* (2014).
11. Krishnamurthy, K., Tewari, J. C., Irudayaraj, J. & Demirci, A. Microscopic and Spectroscopic Evaluation of Inactivation of Staphylococcus aureus by Pulsed UV Light and Infrared Heating. *Food Bioprocess Technol.* **3,** 93 (2010).
12. Demirci, A. & Krishnamurthy, K. Pulsed Ultraviolet Light. in *Nonthermal Processing Technologies for Food* (eds. Zhang, H. Q. et al.) 249–261 (Wiley-Blackwell, 2010). doi:10.1002/9780470958360.ch18
13. Fine, F. & Gervais, P. Efficiency of pulsed UV light for microbial decontamination of food powders. *J. Food Prot.* **67,** 787–792 (2004).
14. Garvey, M., Stocca, A. & Rowan, N. Use of a Real Time PCR Assay to Assess the Effect of Pulsed Light Inactivation on Bacterial Cell Membranes and Associated Cell Viability. *Water Environ. Res. Res. Publ. Water Environ. Fed.* **88,** 168–174 (2016).

15. Jacobs, L. E., Weavers, L. K. & Chin, Y.-P. Direct and indirect photolysis of polycyclic aromatic hydrocarbons in nitrate-rich surface waters. *Environ. Toxicol. Chem.* **27,** 1643–1648 (2008).

16. Bertilsson, S. & Widenfalk, A. Photochemical degradation of PAHs in freshwaters and their impact on bacterial growth – influence of water chemistry. *Hydrobiologia* **469,** 23–32 (2002).

17. Lee, H. *et al.* Photodegradation of benzene and phenanthrene in aqueous solution using pulsed ultraviolet light. *KSCE J. Civ. Eng.* **21,** 1607–1613 (2017).

18. McLeod, A. *et al.* Chicken fillets subjected to UV-C and pulsed UV light: Reduction of pathogenic and spoilage bacteria, and changes in sensory quality. *J. Food Saf.* **38,** n/a-n/a (2018).

19. Hosseini, S., Azar-Daryany, M., Massudi, R. & Elikaei, A. Pulsed UV laser light on Escherichia coli and Saccharomyces cerevisiae suspended in non-alcoholic beer. *Iran. J. Microbiol.* **3,** 31–35 (2011).

20. Berney, M., Weilenmann, H.-U., Simonetti, A. & Egli, T. Efficacy of solar disinfection of Escherichia coli, Shigella flexneri, Salmonella Typhimurium and Vibrio cholerae. *J. Appl. Microbiol.* **101,** 828–836 (2006).

21. UV Properties of Plastics: Transmission and Resistance from Cole-Parmer. Available at: https://www.coleparmer.com/tech-article/uv-properties-of-plastics. (Accessed: 20th February 2018)

22. Anaya, N. M., Faghihzadeh, F., Ganji, N., Bothun, G. & Oyanedel-Craver, V. Comparative study between chemostat and batch reactors to quantify membrane

permeability changes on bacteria exposed to silver nanoparticles. *Sci. Total Environ.* **565,** 841–848 (2016).

23. Zhang, H. & Oyanedel-Craver, V. Comparison of the bacterial removal performance of silver nanoparticles and a polymer based quaternary amine functiaonalized silsesquioxane coated point-of-use ceramic water filters. *J. Hazard. Mater.* **260,** 272–277 (2013).

24. Craven, N., Patterson, A. & Anderson, J. C. A membrane filtration method for estimating the number of viable bacteria in solutions containing antibiotic. *Acta Microbiol. Pol.* **30,** 407–411 (1981).

25. Anaya, N. M., Solomon, F. & Oyanedel-Craver, V. Effects of dysprosium oxide nanoparticles on Escherichia coli. *Environ. Sci. Nano* (2015). doi:10.1039/C5EN00074B

26. Faghihzadeh, F., Anaya, N. M., Schifman, L. A. & Oyanedel-Craver, V. Fourier transform infrared spectroscopy to assess molecular-level changes in microorganisms exposed to nanoparticles. *Nanotechnol. Environ. Eng.* **1,** 1 (2016).

27. Bosch, A. *et al.* Fourier Transform Infrared Spectroscopy for Rapid Identification of Nonfermenting Gram-Negative Bacteria Isolated from Sputum Samples from Cystic Fibrosis Patients. *J. Clin. Microbiol.* **46,** 2535–2546 (2008).

28. Ward, J. H. Hierarchical Grouping to Optimize an Objective Function. *J. Am. Stat. Assoc.* **58,** 236 (1963).

29. Sharrer, M. J. & Summerfelt, S. T. Ozonation followed by ultraviolet irradiation provides effective bacteria inactivation in a freshwater recirculating system. *Aquac. Eng.* **37,** 180–191 (2007).

30. *Canned Citrus Processing: Techniques, Equipment, and Food Safety*. (Academic Press, 2015).

31. Wang, Q., Kang, F., Gao, Y., Mao, X. & Hu, X. Sequestration of nanoparticles by an EPS matrix reduces the particle-specific bactericidal activity. *Sci. Rep.* **6,** 21379 (2016).

32. Massier, S. *et al.* Adaptation of Pseudomonas aeruginosa to a pulsed light-induced stress. *J. Appl. Microbiol.* **112,** 502–511 (2012).

33. Ledakowicz, S., Jacek S. Miller & Dorota Olejnik. Oxidation of PAHs in water solution by ozone combined with ultraviolet radiation. *Int. J. Photoenergy* **3,** 95–101 (2001).

SUPLEMENTARY INFORMATION

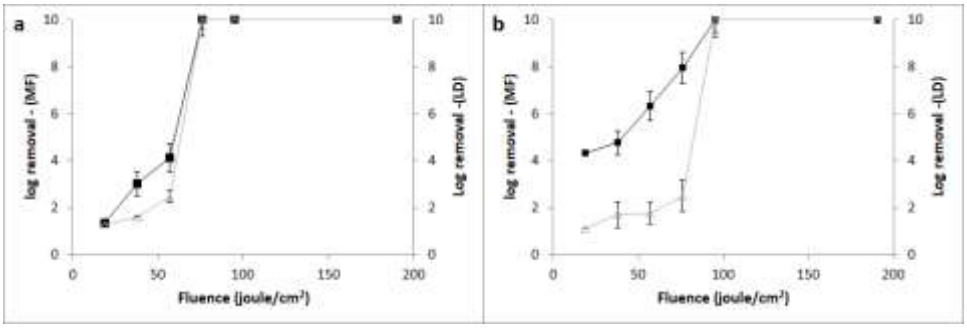

Figure S 12. Kinetic of bacteria removal after PL1 and PL2 exposure using membrane filtration and membrane permeation (live and dead) tests at different fluences of exposure (0, 19, 38, 57, 76, 95, and 190 joule/cm^2). a) Bacterial log removal during exposure to PL1. b) Bacterial log removal during exposure to PL2. –Δ– Marks and grey lines represent the membrane permeation (live and test). –■– Marks and black lines represents membrane filtration test. Error bars indicate the standard deviation of triplicate samples.

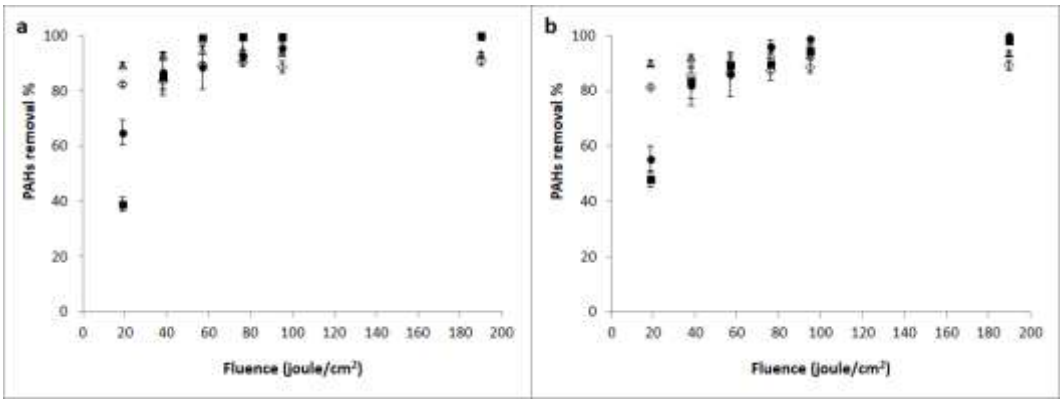

Figure S 13. Kinetic of PAHs removal percentage after PL2 at different fluences of exposure (0, 19, 38, 57, 76, 95, and 190 joule/cm^2) . a) PAHs removal during exposure to PL1. b) PAHs log removal during exposure to PL2. ● marks represent naphthalene. ■ marks represent fluorene. Δ marks represent pyrene. ◊ marks represent anthracene. Error bars indicate standard deviation of triplicates samples.

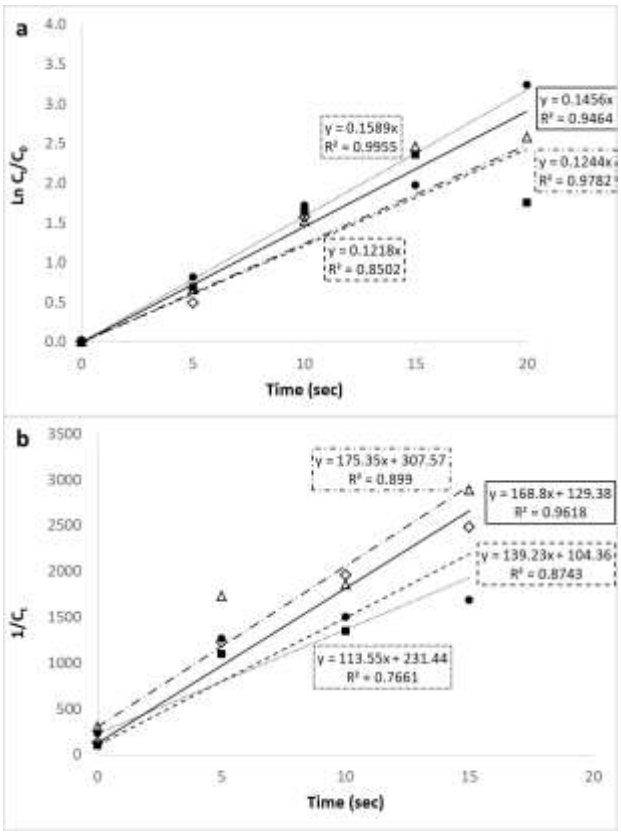

Figure S 14. Kinetic orders of poly aromatic carbons during exposure to PL1 and PL2 for 0, 5, 10, 15, 20, 25, 50 seconds. a) First kinetic orders of the fluorene and naphthalene during exposure to PL1 and PL2. Round dot lines and ● marks represent naphthalene exposed to PL1. Dash lines and ■ marks represent fluorene exposed to PL1. Long dash dot lines and Δ marks represent naphthalene exposed to PL1. Solis line and ◊ marks represent fluorene exposed to PL1. b) Second order kinetic orders of the pyrene and anthracene during exposure to PL1 and PL2. Round dot lines and ● marks represent anthracene exposed to PL2. Dash lines and ■ marks represent pyrene exposed to PL1. Long dash dot lines and Δ marks represent anthracene exposed to PL1. Solis line and ◊ marks represent pyrene exposed to PL1.

Table S 6. Concentrations of PAHs for respiration test of bacteria in presence of PL1 and PL2 exposed PAHs

Samples/PAHs	**Naphthalene**	**Pyrene**	**Fluorene**	**Anthracene**
	[mg/L]	[mg/L]	[mg/L]	[mg/L]
Ctrl-0 joule/cm^2	0.251	0.00975	0.0145	0.00427
PL2-19 joule/cm^2	0.0792	0.0014	0.0073	0.00079
PL1-19 joule/cm^2	0.0405	0.00208	0.0032	0.00050
PL2-190 joule/cm^2	0.040	0.00079	0.0033	0.00309
PL1-190 joule/cm^2	0.0148	0.00048	0.00997	0.0006

Table S 7. Respiration of bacteria after exposure to PL1 and PL2 exposed PAHs in triplicate**.**

RR Slope/Samples	Control Bacteria (No PAHs)	Exposed Bacteria to induced PAHs (0 joule/cm^2)	Exposed Bacteria to induced PAHs (19 joule/cm^2)	Exposed Bacteria to induced PAHs (190 joule/cm^2)
PL2	0.11	0.3	0.32	0.41
PL1	0.11	0.3	0.37	0.32

IV – CONCLUSIONS

We investigated the antimicrobial agent's inhibitory effects in terms of kinetic, metabolic, and cellular component response of bacteria in three studies. In first part of this study, based on the literature review of comparing FTIR with four other tools (Raman, NMR,XPS, mass spectrometry), we selected the more appropriate characterization tool to screen the inhibitory effect of nanoparticles on bacteria. We found FTIR as an appropriate tool to study toxic effects on cellular components of bacteria. FTIR was able to differentiate between exposed and non-exposed bacterial components through change of spectra due to changes of functional groups in biomolecules. In the second part of this study, we applied this tool along with kinetic and metabolic tests for several experimental conditions and found that the inhibitory effects of nanoparticles in a continuous culture depend on the bacterial specific growth rate. At different growth conditions bacteria released different a concentration and composition of extracellular substance (ES). Bacteria at lower growth rate produce ES that are more effective reducing the inhibitory effect of the nanoparticles by changing the physicochemical properties of their surfaces. In the third part of this study, we demonstrated that the recovery of exposed bacteria depends on the range of ultraviolet wavelength applied by comparing the results of kinetic, metabolic and cell compositions of exposed bacteria when lamps with different cut off wavelength were used. At lower wavelength, we observed permanent damage to cellular composition which might be explained by generation of ozone at low ultraviolet wavelength and due to the high adsorption of this wavelength on DNA molecules.

Although experimental conditions in these three studies may diverge from each other (continuous culture vs. batch culture), our results from these three experiments allows us to assess the antimicrobial agent's effects on kinetic, metabolic and cellular composition of bacteria.

The main impacts of this study, is not only on the current protocols used to assess the toxicological response of nanoparticle on microorganism but also determine unintended impacts such as antibiotic resistance, which can have a high impact to public health. Since resistant bacteria not only can compromise the efficacy of antimicrobial agents but also could have implications on public health in terms of metal-antibiotic co-resistance. Hence, if resistant bacteria are released to the environment, it will become a threat to public health.

Overall in this study, we observed that the antimicrobial agents can cause permanent compositional changes of bacteria components. However, the inhibitory effects of antimicrobial agents on bacteria depend on the number of generations that the bacteria culture is exposed. For this purpose, future research should include detection of permanent gene mutations in exposed bacteria by RNA sequencing. The extracted RNA will be sequenced by next generation sequencing (RNAseq). Once the sequencing data has been obtained the sequences will be analyzed using currently by Breseq 0.24rc6 pipeline. Breseq pipeline uses three types of evidence to predict mutations, read alignments (RA), missing coverage (MC), and new junctions (JC). Comparing the sequence of RNA between exposed and non-exposed bacteria at different bacterial generations will assist the scientific community to better understand the number of generation of bacteria that corresponds to gene mutations. Additionally,

investigating bacterial resistance to antimicrobial agents for a larger number of generations of the bacteria culture could provide complementary results to those obtained on this dissertation. New findings in that subject can further support decision making and develop better policies regarding use of antimicrobial agents and their potential negative effects in the environment and public health.